Morphological and Biomechanical Predictions of Cranial Kinesis in Reptile Evolution

IAN N. COST

July 2019

APPROVAL PAGE

The undersigned, appointed by the dean of the Graduate School, have examined the dissertation entitled

Morphological and Biomechanical Predictions of Cranial Kinesis in Reptile Evolution

Presented by Ian N. Cost, a candidate for the degree of doctor of philosophy, and hereby certify that, in their opinion, it is worthy of acceptance.

_____

Professor Casey Holliday

_____

Professor Kristina Aldridge

_____

Professor Kevin Middleton

_____

Professor Manuel Leal

ACKNOWLEDGMENTS

I am grateful for the assistance of numerous individuals and institutions for aiding in the completion of this project. I will begin by expressing my sincerest thanks to my doctoral dissertation committee who helped to develop and guide this project: Casey Holliday, Kevin Middleton, Kristina Aldridge, and Manuel Leal.

Many institutions and individuals helped in procuring specimens and data for this project. I am extremely grateful to the following individuals at loaning and scanning institutions I worked with: Peter Larson (Black Hills Institute), Art Anderson (Virtual Surfaces), Larry Witmer (Ohio University), Ben Marks (Field Museum of Natural History), Zachary Morris and Jeremiah Trimble (Harvard Center for Nanoscale Systems and Museum of Comparative Zoology), Constance Woodman (Hill Country Aviaries), Mark Robbins (University of Kansas Biodiversity Institute), James Schiffbauer and Tara Selly (University of Missouri X-ray Microanalysis Core), Abby Rainwater (MU Raptor Rehabilitation Program), Matt Colbert, Jesse Maisano, and Timothy Rowe (University of Texas High-Resolution X-ray CT Facility), and the Truman VA Biomolecular Imaging Center. My special thanks go out to M. Scott Echols who helped forge a number of aviary and veterinary connections at Tracy Aviary, Hill Country Aviaries and with Constance Woodman, Mark Nielsen, and Brian Speer. I also thank M. Scott Echols for his direct contributions throughout the length of this project.

Many people took the time to ask questions and discuss this project as it developed and as results began to manifest. Without these conversations and interactions with colleagues at conferences, over email, and on a daily basis

some of the ideas in this project may have hobbled along or never fully taken flight. These individuals span from undergraduate students to emeritus faculty. I specifically thank Kelsie Abrams, Alida Bailleul, Jen Bright, Julieta Carril, Don Cerio, Jasmine Croghan, Julian Davis, Federico Degrange, Catherine Early, Daniel Field, Stephen Gatesy, Paul Gignac, Nat Graham (and everyone else at Science on Tap), Brandon Hedrick, Anna Nele Herdina, Anthony Herrel, Tobin Hieronymus, Dominique Homberger, Marc Jones, Mackenzie Kirchner-Smith, Daniel Ksepka, Sharon Kuo, Melissa Macias, Armita Manafzadeh, Faye McGechie, Ralph Molnar, JP Nassif, Aaron Olsen, Benjamin Perlman, Kristen Prufrock, Emily Rayfield, Ryan Ridgely, Rachel Rozin, Kaleb Sellers, Anmol Sethi, Cailtyn Smith, Eric Snively, Anthony Spates, Spiro Sullivan, Diego Sustaita, Ian Trevethan, Morgan Turner, Conner Verhulst, Alec Wilken, Larry Witmer, and Natalie Wright. Many of the above mentioned people have become good friends over the years and I value their involvement in this project and everyday life jointly.

I thank my closest friends, who have checked in on not just the status of the project, but the status of life. They kept me balanced throughout the process. For that I sincerely thank Nina Haro and Joanna Kerby (for asking questions about teaching), Jeff Johnson (for never forgetting to do something to make me laugh on my birthday), Anthony Luna (for all sorts of things, but mostly making me jealous because he saw some rare bird while I was typing away), Frances Owen, Clint Helms,

Jess Casey, and Brian Zinke (for continuing to work outdoors like we all did at Fort Hays and sharing photos of their work). I also must thank S. Christopher Bennett for taking a chance on me as a master's student, beginning this whole journey and Greg Farley for encouraging my interests in birds. I also thank all of the students I ever taught, undergraduate students and middle school alike.

I thank my family for always supporting me and urging me to push myself to get what I want from life and never to settle. My mother Diana for having the energy of five people and tiring me out over the phone talking about my project and life and my brother Tyler for updating me constantly about music, hockey, and video games over the years, giving us something different to talk about. My second set of parents, Tammie and Brian for always being interested in whatever I was doing during this project because they were just naturally curious about some of the things I was doing, have my heartfelt thanks. And finally, and never least, my wife Jennifer who suffered through my desire to quit a full time job to go back to school, became a reluctant amateur bird watcher, moved to western Kansas, and listens to me talk about parrots and computer modeling on a more than regular basis and does it all with a smile, even if she just wants to read a book and have a quiet moment without birds being mentioned.

TABLE OF CONTENTS

LIST OF FIGURES AND ILLUSTRATIONS

LIST OF TABLES

ABSTRACT

Feeding is a complex behavior that all tetrapods engage in on a regular basis to procure energy and survive. The reptilian feeding apparatus includes many types of feeding behaviors including multiple methods of engaging cranial kinesis, the ability to move one portion of the skull in relation to another portion of the skull. Understanding the underlying mechanisms of cranial kinesis enabled feeding mechanism is integral to understanding avian feeding behaviors, strategies, and ecology. Chapter 1 introduces how the feeding apparatus of reptiles is modified during the evolution of birds from dinosaur and reptile relatives. During this introductory chapter I lay the foundation for our knowledge of avian feeding and its evolution and describe the musculoskeletal environment of the avian feeding apparatus, which becomes the main focus of the rest of this project. Chapter 2 explores the diversity of jaw muscle resultants across a sample of birds, dinosaurs and other reptiles using ternary plots. Jaw musculature orientations are altered across ontogeny, behavior, and evolution. I use ternary plots to investigate the diversity of jaw muscle orientations across the ontogeny and feeding behaviors of alligators and through evolution in the dinosaur to bird lineage. Additionally, I use ternary plots to show how diverse organisms use different muscles to produce high bite forces. Chapter 3 introduces and demonstrates the use of postural modeling to investigate the feeding apparatus at a specific instant of a feeding behavior. I investigate the kinetic capability of 3 taxa using this method. I use my postural modeling method to validate postural models of known behaviors in extant taxa first. I then evaluate the kinetic

capabilities of an extinct animal, *Tyrannosaurus rex*. Finally, Chapter 4 investigates the diversity of the feeding apparatus across parrots, a lineage of morphologically comparable birds with distinctive ecological roles. The biomechanical requirements of similar functional morphology used for diverse feeding behaviors are analyzed here. I use statistical and finite element analyses to describe the biomechanical environment of the feeding apparatus in parrots. I analyze stress and strain dissipation as well as geometric properties of bone mechanics that enable parrots to engage in cranial kinesis. I use a phylogenetic tree informed by molecular phylogenies to plot and compare ancestral reconstructions of characters of the feeding apparatus in parrots. My findings using these methods describe the diversity of the musculoskeletal systems of diverse parrots. The data gathered from the studies described here form the foundation of a better understanding of the biomechanics of the avian feeding apparatus. The findings described here will be used in future studies to describe the underlying mechanisms that govern diverse feeding behaviors.

Chapter 1

Introduction: Avian Evolution and Feeding

Early Evolution of Birds

The intake and processing of energy is essential for all forms of life. In tetrapods this process begins with the feeding apparatus, which is responsible for mechanically ingesting, and sometimes processing, sources of energy. Many forms of the feeding apparatus have evolved over the evolutionary history of animals with each morphology reflecting the feeding strategy of the animal which uses it. In archosaurs the feeding apparatus exists in a multitude of shapes and sizes. The various forms of the feeding apparatus can be either rigidly fixed within the cranium or capable of movement at mobile articulations of the skull, which is known as cranial kinesis (Versluys 1910; Bock 1964; Zusi 1993). Birds, among archosaurs, are exceptional examples of this movement between the braincase, and the facial skeleton.

The archosaur lineage split around 240 million years ago during the Triassic period, giving rise to both the crocodile and dinosaur-bird lineages (Fig. 1-1; Kumar and Hedges 1998). The earliest birds originated from theropod ancestors some time later during the Late Jurassic (Ostrom 1976; Padian and Chiappe 1998; Prum 2002; Godefroit et al. 2013). Our knowledge of this transition originally rested largely in the non-avian theropod *Archaeopteryx*. In the past 30 years, evidence of the transition has become more abundant as more ancestors of birds, such as *Jeholornis*, *Sinosauropteryx*, and *Microraptor* have been discovered and described (Chatterjee 1991; Ji and Ji 1996; Xu et al. 2000;

Zhou and Zhang 2002). Modern birds began to appear in the Middle Cretaceous (Gauthier and de Queiroz 2001). This group consisting of all living birds is known as the Neornithes.

Neornithe birds diversified further into the two main groups of birds, the Paleognathae and Neognathae, beginning approximately 98 million years ago (Mayr 2011; Suh et al. 2011; Claramunt and Cracraft 2015). The Paleognathae are named for their palatal configuration; paleognath means “old mouth”. Despite the meaning of this name, the palates of paleognath birds do not resemble those of their dinosaur ancestors or the earliest birds. The palatines and pterygoids of palaeognath birds are dorsoventrally flattened. Neognath, conversely, means “new mouth” and possess palatine bones that are dorsoventrally tall and cylindrical pterygoid bones (Huxley 1867; Simonetta 1960; Bock 1963; Parkes and Clark 1966; Gussekloo and Zweers 1999). The Paleognathae consists of the ratites and tinamous. These birds are placed in five extant groups and are most closely related the oldest forms of modern birds, including the extinct Moas and Elephant birds (Baker et al. 2005; Baker et al. 2014; Mitchell et al. 2014). Gallanseriformes constitute the most primitive clade of neognath birds and diverged from other groups approximately 80 million years ago (Jetz et al. 2012; Prum et al. 2015). Parrots, falcons, and songbirds began to diverge from other groups approximately 75 million years ago; falcons began diverging from this subgroup approximately 41 million years ago, parrots 56 million years ago, and songbirds 67 million years ago (Chubb 2004; Ericson et al. 2006; Hackett et al. 2008; Mayr 2011; Prum et al. 2015).

Relationships between Parrots and Falcons

Over the past 30 years the fields of molecular biology and molecular evolution have radically altered the accepted phylogenetic relationships of bird families, in some parts of the phylogeny drastically altering existing relationships between sister taxa (Sibley and Ahlquist 1990; Sibley and Monroe 1990; Groth and Barrowclough 1999; Sheldon et al. 1999; Mayr et al. 2003; Paton et al. 2003; Chubb 2004; Dyke and Van Tuinen 2004; Fain and Houde 2004; Ericson et al. 2006; Ksepka et al. 2006; Paton and Baker 2006; Fain and Houde 2007; Hackett et al. 2008; Lanfear and Bronham 2011; Mayr 2011; Suh et al. 2011; Jarvis et al. 2014; Prum et al. 2015). The most current molecular phylogeny, Prum et al. 2015, places parrots (Psittaciformes) as the sister group to falcons (Falconiformes) and all songbirds (Passeriformes).

Recently, studies of nuclear DNA sequences (Hackett et al. 2008) and retroposons (Suh et al. 2011) have both illuminated the phylogenetic relationship between falcons and parrots. The most recent genetic study of avian DNA conducted by Prum et al. (2015) reconfirmed the relationship espoused in the two previous studies using large-scale genomic sequencing and DNA-DNA hybridization. Falcons and parrots also share morphological similarities. In the cranium, both parrots and falcons possess tomial teeth along their upper, decurved, beaks, and bony tubercles in their holorhinal nostrals (Hull 1991; Homberger 2003; Mayr 2010; Toft and Wright 2015). Oral cavity structure of

falcons and parrots are similar in that the pterygoid bones are highly cylindrical and resist dorsoventral bending more than mediolateral bending forces.

The palatines and quadrates of these two groups are considerably different. Falcons also lack m. pseudomasseter (mPM) and m. ethmomandibularis (mEM) but do possess clear and discernible bellies of m. pseudotemporalis profundus (mPSTp). As dedicated predators, the orbits of falcons are oriented rostrally and converge appreciably (*Falco peregrinus* possesses a 74.52° overlap according to Iwaniuk et al. 2008), affording the falcons with significant stereoscopic vision (Fox et al. 1977). Parrot orbits, however, are oriented more laterally (*Melopsittacus undulates* possesses largest overlap of tested parrots at 56.45° according to Iwaniuk et al. 2008), resulting in a minimal stereoscopic field of vision (Demery et al. 2011). Descriptions of morphological and phylogenetic disparities, and similarities, among parrots and falcons are integral to generating a fully informed and complete phylogenetic tree.

Cranial Kinesis and the Anatomy of the Feeding Apparatus

Cranial Kinesis and Feeding

Cranial kinesis is hypothesized to be plesiomorphic for all tetrapods (Iordansky 1989). The process of cranial kinesis involves movement of the palatine, pterygoid, and quadrate bones in relation to a palatobasal and otic joint with the braincase and another rostral joint like the craniofacial hinge. In different groups this rostral joint can be comprised of a variety of different joints. The most

common kinetic joints are those between either the frontal and nasal bones or between the frontal and parietal bones (Frazzetta 1962; Bock 1964; Iordansky 1989; Bock 1999; Herrel et al. 1999; Schwenk 2000; Bout and Zweers 2001). Lepidosaurs exhibit cranial kinesis between the frontal and parietal bones when feeding (Gans 1961; Cundall, 1983; Herrel et al. 1999; 2000). Among the extant archosaurs, crocodiles and avians, however, the birds are the only group that exhibit cranial kinesis (Bock 1964; Zusi 1993; Schwenk 2000). Avian cranial kinesis always occurs in the frontal-nasal junction of the cranial skeleton (Bock 1964; Tokita et al. 2007; Bailleul et al. 2017). All songbirds possess the functional morphology capable of producing and undergoing cranial kinesis (Bock 1964; Zusi 1984; Hoese and Westneat 1996; Bock 1999; Zweers 1999; Bout and Zweers 2001; Meekangvan et al. 2006). Falcons also possess kinetically competent cranial anatomy but have not been observed significantly employing kinesis within their typical behavioral activities. However, falcons are an interesting sister group and the closest non-songbird relatives to parrots.

Birds as a whole can be split into two smaller groups based on the morphology of their feeding apparatus and these distinctions are important in inferring cranial kinesis in avian taxa. The oldest group of birds, the paleognathae (translating to “old mouth”), possess rigid open palates (palatine – pterygoid complex) in the roofs of their mouth and weakly flexible connected joints in the frontoparietal and frontonasal areas (Gussekloo and Zweers 1999; Gussekloo 2000). The palates of these avians are constructed to resist bending of the upper bill and restricting movements in the rostrocaudal plane of the cranium (Parker

1866; Gussekloo 2005; Gussekloo and Bout 2005; Degrange and Picasso 2010). The lack of kinetic capability is a defining characteristic of the paleognathae, whereas birds of the neognathae (translating to “new mouth”) group are known in part for their kinetic capability. This group possesses a palate with open palatobasal joints and mobile craniofacial and otic joints. Cranial kinesis in this group of birds exists as two main varieties of kinetic competency, movement about the craniofacial skeleton at joints between the cranium and “face”. The first of the two varieties of kinetic competency in avians is rhynchokinesis, observed mainly in shorebirds (Charadriiformes) which are capable of kinesis between the premaxilla and maxilla of the upper beak (Zusi 1984; Chandler 2002; Estrella and Masero 2007). The other is coupled prokinesis, observed in neognathae outside of shorebirds which include kinetic capabilities between the frontal and nasal bones and, in rhynchokinesis, within the premaxilla and maxilla (Zusi 1993; Hoese and Westneat 1996; Tokita et al 2007).

The degree to which neognathae birds are capable of kinesis relies on the connections between the frontal and nasal bones that constitute the kinetic joint. In ducks and geese (Anseriformes) the bony connections at the frontonasal joint are somewhat extensive but still allow for extension and flexion of the joint (Bailleul et al. 2017). Movement of the quadrate is known to be considerable in ducks (Dawson et al. 2011). The accompanying assumption of the extensive movement of the quadrate is that the rostral effects on the palate of Anseriformes is likely significant as well, though this requires more study. Chickens (Galliformes), parrots (Psittaciformes), crows (Corvidae), pigeons (Columbidae),

and finches (Fringillidae) have all been discussed in regard to their kinetic capabilities. The majority of these studies have largely consisted of ecomorphological observations (Bock 1964; Burton 1974; Hoese and Westneat 1996; Bock 1999; Homberger 2003; Claes et al. 2017; Muyshondt et al. 2017.)

Cranial Kinesis and Corresponding Anatomy in Parrots

Among previously observed kinetically competent taxa, parrots are a highly charismatic group and are among the most kinetic tetrapods. Additionally, parrots are capable of generating relatively high bite forces despite their highly mobile skulls. The craniofacial joint (referred to hereafter as the craniofacial hinge) in parrots is largely unobstructed by bony tissue, and consists mainly of soft articular tissues capable of extensive dorsoventral excursions. However, Tokita (2003) and Tokita et al. (2007) histologically analyzed the development of the craniofacial hinge in parrots (*M. undulates* and *N. hollandicus*) and discovered that the small ossifications were derived from posteromedial projections of the premaxilla overlaying the nasal bones. Bühler (1982) noted without using histological evidence that larger parrots appear to possess only a synovial joint, entirely lacking the posteromedial projections of the premaxilla described by Tokita (2003) in the small parrots *M. undulates* and *N. hollandicus*.

The kinetic system is mobilized and stabilized by m. adductor mandibulae posterior (mAMP) and m. protractor pterygoidei et quadrati (mPPt) (Homberger 2003). The movement of the quadrate at the otic joint is translated to the pterygoids which are tubular and elongate rostrocaudally. The pterygoids in turn

branch between the quadrate and palatobasal-pterygopalatine joints where the pterygoid abuts the palatine bone, the opposite pterygoid (in some parrots) and the interorbital septum ventrally at the surface of the parasphenoid rostrum (palatobasal joint) (Burton 1974; McKibben and Harrison 1987; Baumel et al 1993; Homberger 2003; Beaufrère et al. 2019). The palatines are mobilized rostrally during this activity and they in turn mobilize the beak through their contact at the palatomaxillary joint. Additionally, this suite of movement is linked back to the quadrate through the jugal and quadratojugal complex which articulates rostrally with the maxilla of the beak and caudally with the quadrate itself. The additional restraint of the postorbital ligament aids to limit the maximum excursion of the beak during cranial kinesis (Homberger 2003).

Musculus pseudomasseter is a variably present muscle in parrots that occupies a superficial position within the adductor chamber when present though it originates from the posteromedial region of m. adductor mandibulae externus superficialis (mAMES; Tokita 2004). The deep muscles, m. adductor mandibulae externus profundus (mAMEP), m. adductor mandibulae posterior (mAMP), and m. pseudotemporalis superficialis (mPSTs), fill the temporal fossa. The pterygoideus muscles contribute extensively to jaw closure (bite force), constitute the largest group of cranial muscles in parrots, and stabilize the kinetic palate (Burton 1974; Homberger 2003). The pterygoideus muscles are differentiated into three identifiable muscles. One of the muscle bellies, mEM, is a muscle specific to parrots derived from the belly of m. pterygoideus dorsalis (mPTd; Baumel et al. 1993; Tokita 2004; Carril et al. 2015). Musculus ethmomandibularis

attaches to the medial side of the mandible and, rostrally, medially, and superiorly to the eye along the rostral interorbital septum (Baumel et al. 1993; Tokita 2004; Homberger 2003; Carril et al. 2015). The remaining two pterygoideus muscles, m. pterygoideus dorsalis (mPTd) and m. pterygoideus ventralis (mPTv), attach to the dorsolateral and ventromedial surfaces of the palatine and pterygoid bones, respectively, as well as the caudomedial (mPTv) and caudolateral (mPTd) aspects of the mandible. These muscle bellies are responsible for closing the mouth as they “simultaneously close both the upper and lower jaws,” (Baumel et al. 1993) as they pull on aspects of both the palate and cranium and the mandible (Burton 1974; Homberger 1980; Buhler 1981; Homberger 2003).

Musculus depressor mandibulae (mDM) and m. pterygoideus et quadrati (mPPt) aid in depression of the mandible (Bühler 1981). Musculus pterygoideus et quadrati is also essential in propelling the pterygoid and quadrate rostrally, aiding to elevate the maxillary rostrum during bouts of cranial kinesis (Fig. 1-2; Bock 1966; Bühler 1981; Baumel et al. 1993; Homberger 2003). Musculus depressor mandibulae attaches to the caudal margin of the skull by filling the subtemporal fossa between the temporal fossa and the transverse nuchal ridge of the occipital region of the skull (Baumel et al. 1993). Musculus pterygoideus et quadrati attaches to the ventral edge of the interorbital septum medially and the caudal end of the pterygoid and the orbital process of the quadrate (Baumel et al. 1993). The adductor and pterygoideus complex is also entirely independent of the ocular muscles, though two muscles (mEM and mPSTs) occupy attachment

sites on the interorbital septum where the ocular muscles also attach. The orbit of parrots is highly specialized to contain a large eye and its ocular muscles as well as attachments for jaw closing muscles and, in some parrots, ossified suborbital ligaments. The resulting suborbital arch of bone variably serves as an attachment point for the adductor chamber muscle mPM; though, not every parrot possessing mPM has a suborbital arch and not every parrot possessing a suborbital arch has a definable and dissectible mPM (Tokita 2003; Tokita et al. 2007).

The ventral border of the orbit is defined by the dorsal surfaces of the palatines, the articular tissue at the palatobasal and pterygopalatine joints, and the dorsal surface of the mPTd muscle at its dorsal-most attachment site on the palatine (Jones et al. 2007). The palatines are also uniquely shaped in parrots. As in other birds, parrots possess a horizontal shelf along the midline of their palatines which articulates with the parasphenoid rostrum at the palatobasal joint. Laterally located shelves of the palatine extended ventrally between the mandibles. The hyoid bones of the tongue and the esophagus and trachea are located in the midline between the shelves. These large shelves serve as attachments for the extensive pterygoideus muscles (mPTd and mPTv).

This dissertation research investigates the functional morphology of the reptilian feeding apparatus to better understand the evolution of reptile feeding behaviors and function. I provide specific methods for visualizing the complex orientations of three-dimensional (3D) muscles in in two-dimensional (2D) space. Then I analyze the impacts that postural behavioral changes have on the feeding

apparatus of known kinetic lepidosaurs and avians and hypothesized kinetic non-avian archosaurs. Finally, I thoroughly analyze the biomechanical environment of the feeding apparatus across a group of related animals with similar morphology. These insights will enhance the representation of data in future 2D publications and improve investigations into feeding kinematics and biomechanics by providing new methods to address questions concerning functional morphology, ecology, and behavior.

Chapter two of this dissertation provides a new tool based on past work using ternary diagrams in chemistry (e.g. Othmer and Tobias 1942), geosciences (e.g. Norton 1966), and biology (e.g. Capano et al. 2019) to visualize 3D relationships of muscles and their orientations in 2D space. This study presents data from ontogeny, behavior, and phylogeny with crocodilian, avian, and non-avian dinosaur taxa. Results from this study are applicable to all 3D structures and will enable researchers to better visualize and share their 3D information in 2D publications.

Chapter two of this dissertation investigates the effects that postures of the feeding apparatus have on the biomechanical environment of lepidosaurs and archosaurs. This study analyzes the hypothesis that Tyrannosaurus rex was capable of cranial kinesis by validating postural behavioral models using the performance of known kinetic taxa. Taxa are placed in one neutral posture and two kinetic postures to validate the biomechanical parameters of the known preferred kinetic posture; instantaneous recreations of skeletal configurations of distinct behaviors. The same process is then carried out with Tyrannosaurus rex

and the results are analyzed for congruency with the postures in the two known taxa. This study establishes a new method of testing and analyzing taxa biomechanically for kinetic competency and preferred kinetic posture using computer models. This study also forms the basis of future work in describing the feeding apparatus and feeding behaviors of extinct taxa in greater detail than is currently available.

Chapter three of this dissertation investigates the biomechanical environment of the feeding apparatus of a group of closely related birds. The evolutionary history of the feeding apparatus is complex. However, developing a better understanding of the evolutionary history of the feeding apparatus in a closely related group of birds will help to better understand the larger process of evolution. Parrots with diverse diets and similar functional morphology are modeled in this study and parameters including muscle force, stress and strain, second moment of area, and measurements of the skull are used to analyze bite force, bone bending resistance, and stress and strain mitigation in the kinetic palate. Continuous and discrete characters are analyzed using squared-change parsimony (for continuous characters) and maximum likelihood (for discrete characters) ancestral state reconstructions (Garland Jr. et al 1997; Pagel 1999). Ternary diagrams were employed, as in chapter one, to analyze muscle orientations in parrots. Analytical methods of biomechanical models used in chapter two were used in this chapter as well, and additional analyses, including mapping strain profiles of bones, were conducted. Geometric properties of the pterygoid were investigated to determine the resistance to bending and

compression in the bone, as these are concepts integral to the proper functioning of this bone as a strut in the head. This work lays out a firm base of future studies for cataloging and detailing the biomechanical environment of the feeding apparatus. This study also forms the basis of future ancestral state reconstruction analysis using continuous morphological variables of the feeding apparatus that will be applied across all avian lineages.

This dissertation will form the basis for many necessary avenues of study within avian lineages. Chapters 2 and 4 of this dissertation will specifically enhance our knowledge of how the avian feeding apparatus evolved into the many forms it is now observed in and how those forms biomechanically function. Further, chapter 3 will add to our knowledge of the biomechanical function of the feeding apparatus. Together, the results of all of the chapters of this dissertation research will inform future studies investigating ecology, morphology, and evolution. These future endeavors will provide answers critical to better understanding the function and evolution of the feeding apparatus in archosaurs and reptiles as a larger group.

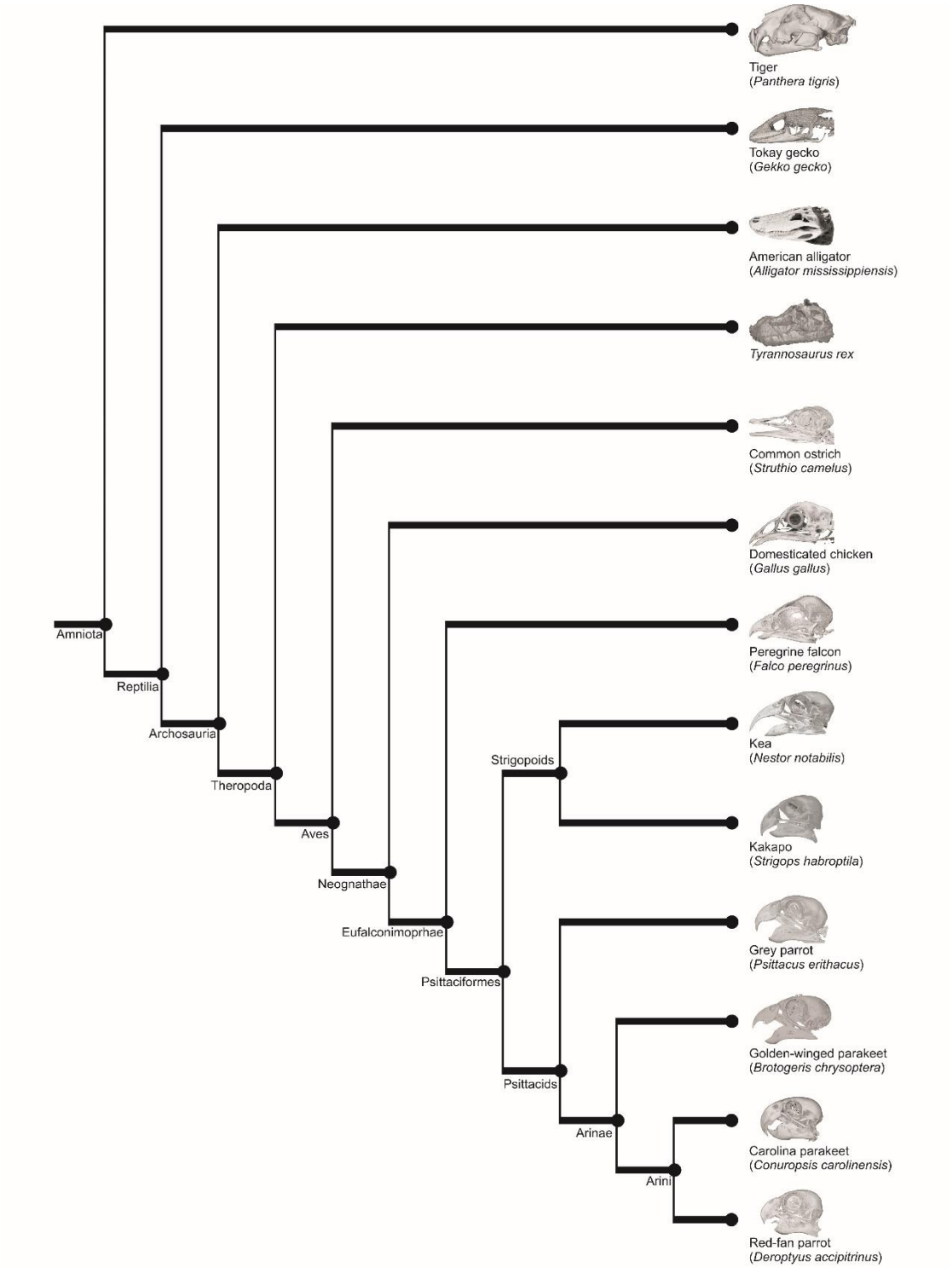

Figure 1-1. Phylogenetic tree of Archosauria and Lepidosaur sister group. Synapsids are represented as an outgroup. Avian taxa comprise the majority of the tree. Skulls were processed in Avizo by the author from scans procured at Truman VA Biomolecular Imaging Center (Columbia, MO), University Hospital Department of Radiology (University of Missouri, Columbia, MO), School of Veterinary Medicine (University of Missouri, Columbia, MO), Geological Sciences X-ray Microanalysis Core (University of Missouri, Columbia, MO), and OhioHealth O'Bleness Hospital (Athens, OH).

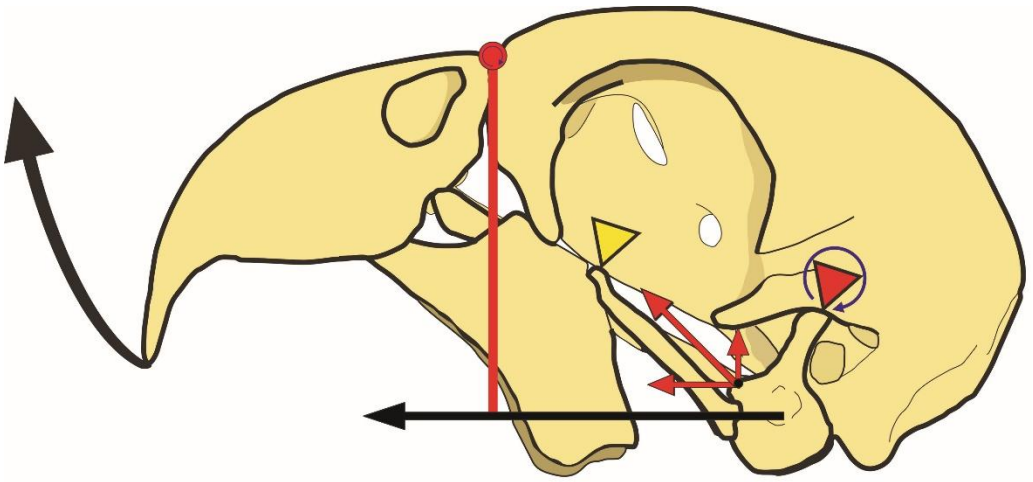

Figure 1-2. Diagrammatic representation of cranial kinesis with an emphasis on the contraction of m. pterygoideus et quadrati (mPPT; red arrows). The red triangle is a fulcrum placed at the otic joint, the joint at which cranial kinesis mobilizations originate. The blue arrow around the otic joint fulcrum indicates the direction of rotation. The yellow triangle is a fulcrum placed at the palatobasal joint which acts as a secondary link the mechanism of cranial kinesis. Solid black arrow originating at the middle of the quadrate represents the jugal and its directional movement. Vector arrows from the quadrate are modeled after Bühler's (1981) representation of the vectors of mPPT: rostral and dorsal pointing arrows represent those components of mPPT force acting on the quadrate and pterygoid. Arrow obliquely oriented parallel to the pterygoid represents the muscle resultant of mPPT. The red vertical bar represents the linkage between jugal and palate to the craniofacial hinge (red circle with blue arrow inset to indicate direction of rotation). Curved black arrow at beak tip represents movement of the maxillary rostrum due to cranial kinesis (Modified after Bühler, 1981, Fig 8.6.)

Chapter 2

Visualization of Complex Muscle Function of Gape, Ontogeny, and Evolution in Three Dimensions

Introduction

Recent advances in imaging and computational methods are enabling researchers to capture three-dimensional morphology at high resolutions. Researchers are ushering in a renaissance of imaging approaches in areas such as astronomy (Cohen et al. 2003; Preusker et al. 2015; Korsun et al. 2016), biochemistry (Lüthy et al. 1992; Zemla 2003; Arnold et al. 2006), and even archaeology and anthropology (Hughes et al. 2005; Lee et al. 2007; Carlson et al. 2011; Du Plessis et al. 2015). Similarly, biological sciences are greatly enhanced by morphological studies incorporating large amounts of high resolution three-dimensional data. Morphologists frequently model diverse systems in entomology (Klaus et al. 2003; Friedrich and Beutel 2008), physiology (Witmer et al. 1999; Schachner et al. 2013; Tsai and Holliday 2015; Kelly 2016; Stephenson et al. 2017), neuroanatomy (Evans et al. 2009; Lautenschlager et al. 2012; Kawabe et al. 2013), and skeletal tissue biomechanics (Grosse et al. 2007; Cuff et al. 2015) using high resolution data. Modeling musculoskeletal systems in 3D is enabling researchers to investigate the underlying biomechanics of behaviors such as feeding (Gans et al. 1985; Zusi 1987; Witmer and Rose 1991; Hoese and

Westneat 1996; Herrel et al. 1999; Dumont et al. 2005; Dawson et al. 2011; Snively et al. 2013; Sellers et al. 2017; Bates and Falkingham 2018) and locomotion (Bramwell and Whitfield 1974; Lauder et al. 2003; Hutchinson 2004; Charles et al. 2016; Manafzadeh and Padian 2018) using computational and imaging methods such as finite element analysis (e.g. Keyak et al. 1993; Rayfield 2007; Santana et al. 2010), XROMM (e.g. Brainerd et al. 2010; Baier et al. 2013), and multibody dynamics (e.g. Moazen et al. 2009; Curtis et al. 2010; Snively et al. 2015).

In many biomechanical studies great interest has been expressed in estimating and calculating bite force, a vertical component of force. This interest in a vertical component of force is somewhat a result of an historical focus on mammalian feeding and locomotor systems in which muscles largely act in parasagittal planes (e.g. Maynard Smith and Savage 1959; Dullemeijer 1956; Cartmill 1974, 1985). The complicated 3D anatomy of the musculoskeletal system remains difficult to share in 2D publications and other disseminations (e.g. Greaves 1982; Sinclair and Alexander 1987; Bimber et al., 2002; Lockwood et al. 2002; Holliday and Witmer 2007; Vincent et al. 2007; Huber et al. 2008; Sustaita 2008; Holliday 2009; Kolmann and Huber 2009; Pfaller et al. 2011; Figueirido et al. 2013; Holliday et al. 2013; Cost et al. in press). We are therefore often forced to decompose multidimensional measurements into more simplified plots that are designed specifically for 2D publishing. This, in turn, causes higher order questions of behavior, ontogeny, and phylogeny to be even more challenging to analyze and disseminate. One solution, when appropriate, is to

project 3D data in a ternary diagram. Ternary diagrams have a long history of use in geology, chemistry, and physics, wherein the relative contributions of three variables to a whole are studied. For example, phases of matter (Othmer and Tobias 1942), soil composition (Norton 1966), vertebrate limb proportions (Middleton and Gatesy, 1997), and ventilation kinematics (Capano et al. 2019) have made use of ternary diagrams in the past.

Here we provide examples of how cranial muscle resultants of archosaurs change over time using three case studies of behavior, ontogeny, and phylogeny. Archosaurs are the clade of tetrapods that includes crocodylians, dinosaurs and birds. Within a single individual, the three-dimensional nature of the cranial musculature requires that muscle forces and resultants must vary with gape (Herring and Herring 1974; Dumont et al. 2003) during a feeding bout. Our case study shows how ternary plots enable researchers to visualize the changes in orientations through one open to close phase of a feeding cycle in alligators. Archosaurs have a wide diversity of cranial morphologies and feeding ecologies that both change ontogenetically (Fig. 2-1; Erickson et al. 2003; Yanega and Rubega 2004; Grigg 2015). Here, our case study shows that ternary plots are able to track the trajectory of muscle orientation change through ontogeny in alligators. Finally, comparisons across geological time reveal broad patterns among Archosauria including repeated evolution of large body size (Turner and Nesbitt 2013), convergent

evolution of feeding ecologies (Burton 1974b) and relatively hard biting in diverse clades (e.g. Carril et al. 2015; Sellers et al. 2017; Bates and Falkingham 2018). To show an example of how ternary plots can be used to track evolution and patterns of differential muscle use, we plotted the orientations of muscles across a sample of avian phylogeny and we also show how three hard-biting taxa differentially organize cranial muscles to produce high bite forces. We show that ternary diagrams are particularly useful for conveying components of jaw muscle resultants at different scales of organization, enabling comparisons of higher order biomechanical data across behavior, ontogeny, and phylogeny. We show that, using ternary diagrams, complex 3D structures can be represented in a 2D space such that anatomical relationships and physiological parameters are retained as comparable data.

Methods

Materials and Imaging

The skulls of four extant taxa (*Alligator mississippiensis*: MUVCAL008, MUVCAL024, MUVCAL031, MUVCAL612, MUVCAL622, MUVCAL700; *Struthio camelus*: OUVC10659; *Gallus gallus*: MUVCAV003; and *Psittacus erithacus*: MUVCAV042, MUVCAV092) and one extinct taxon (*Tyrannosaurus rex*: BHI3033) were scanned using computed tomography (CT) or micro-computed tomography (µCT; Table 1). Specimens of *Alligator* (MUVCAL031), *Gallus* (MUVCAV003), and *Psittacus* (MUVCAV042) were µCT scanned at the Truman VA Biomolecular Imaging Center, in Columbia, MO (Siemens INVEON164

SPECT/CT, Siemens Medical Solutions USA Inc.). The largest *Alligator* specimen (MUVCAL008) was CT scanned at the University of Missouri Medicine Department of Radiology (Siemens Somatom Definition Scanner, Siemens Medical Solutions USA Inc.). All other *Alligator* specimens (MUVCAL024, MUVCAL612, MUVCAL622, MUVCAL700) were CT scanned at the University of Missouri School of Veterinary Medicine (GE LightSpeed VCT CT scanner)(Sellers et al., 2017). A second *Psittacus* specimen (MUVCAV092) was µCT scanned at the University of Missouri Department of Geological Sciences X-ray Microanalysis Core (Zeiss Xradia 510 Versa 3D x-ray microscope, Carl Zeiss Microscopy, LLC). A 1/6-scale model of *Tyrannosaurus rex* (BHI 3033) and *Struthio* were scanned at OhioHealth O'Bleness Memorial Hospital, Athens, OH (General Electric LightSpeed Ultra Multislice CT scanner; Cost et al., in press).

Muscles of interest (m. adductor mandibulae externus medialis, mAMEM; m. adductor mandibulae externus profundus, mAMEP; m. adductor mandibulae externus superficialis, mAMES; m. adductor mandibulae posterior, mAMP; m. pterygoideus dorsalis, mPTd) were identified through physical dissection and processed diffusible iodine contrast-enhanced CT and µCT images (DiceCT; Fig. 2-2; Gignac et al. 2016). Scans were rendered and segmented manually at thresholds unique to each scan using Avizo v9.5 (FEI Houston Inc., Hillsboro, OR; Fig. 2-3A). Avizo segmentation was informed by first-hand observation,

reference to the literature, and consultation among colleagues. Segmentation was conducted by myself, Rachel Rozin, Kaleb Sellers, and Anthony Spates. Defects and segmenting artifacts were cleaned and models were registered to a global coordinate system fitted to a transverse plane below the mandibles in Geomagic Studio 2013 (3D Systems, Rock Hills, SC). Axes were oriented such that the X-axis corresponded to the mediolateral axis, the Y-axis to the dorsoventral axis, and the Z-axis to the rostrocaudal axis. Models were then imported into Strand7 (Strand7 Pty Ltd, Sydney, NSW) and solid elements applied to create a finite element model (FEM). Muscle attachment areas were identified and mapped on the FEM and tessellated to form a matching shell that serves as both a measurable shape as well as a source for muscle forces (Fig. 2-3B and Fig. 2-4). Muscle maps were estimated from direct observations of material (dissections, DiceCT; see Fig. 2-2), interpretations of osteological correlates, and the literature when necessary (e.g., Baumel et al. 1993; Holliday and Witmer 2007, Holliday 2009).

Modeling Muscle Orientation and Force

Physiological cross-sectional areas (PCSA) of muscles were determined by physical dissection or extant phylogenetic bracketing of taxa, as in *T. rex* (Sellers et al. 2017, Cost et al. in press; Fig. 2-3c). Muscle parameters (e.g., pennation angles) were estimated to fall within known ranges for alligators and birds and osteological correlates of representative fossils informed PCSA estimates in *T. rex* (Cost et al., in press). Muscle orientations were calculated

from the centroid of the cranial attachment to the centroid of the palatal or mandibular attachment. The centroids and muscle areas were calculated STLs using the program Area_Centroid_From_STL (Davis, et al. 2010; Santana et al. 2010). Muscle resultants were computed from physiological cross-sectional area estimations, areas of muscle attachments, and the centroids of the attachments.

Ternary Diagrams

Ternary diagrams are used to represent three-variable systems in which the sum of the variables is a constant. Here, the three relative positional components (x, y, z) of a vector sum to 100. To calculate relative orthogonal contributions for a muscle vector, a three-dimensional vector representing coordinates of a muscle's origin (x_{or}, y_{or}, z_{or}) and insertion (x_{ins}, y_{ins}, z_{ins}) is first translated to the origin by subtracting insertion coordinates from origin coordinates:

$$(x_0, y_0, z_0)=(x_{ins}\text{-}x_{or}, y_{ins}\text{-}y_{or}, z_{ins}\text{-}z_{or}). \quad (1)$$

The resulting vector is normalized to a unit vector by dividing each element by the vector's magnitude:

$$(x, y, z) = \left(\frac{x_0}{\sqrt{x_o^2+y_0^2+z_0^2}}, \frac{y_0}{\sqrt{x_o^2+y_0^2+z_0^2}}, \frac{z_0}{\sqrt{x_o^2+y_0^2+z_0^2}} \right) \quad (2)$$

The relative proportions of (x, y, z) are then calculated as:

$$(x', y', z') = \left(\frac{x^2}{x^2+y^2+z^2}, \frac{y^2}{x^2+y^2+z^2}, \frac{z^2}{x^2+y^2+z^2}\right). \quad (3)$$

The relative proportions (*x*', *y*', *z*'), which sum to 1, represent the contributions of the mediolateral (*x*'), dorsoventral (*y*'), and rostrocaudal (*z*') components of each muscle's 3D orientation. Ternary diagrams were used to represent the muscle component vectors in two dimensions, with size of the point scaled to each muscle's force (Fig. 2-3). All calculations and plots were solved and created, respectively, in R (ver. 3.5.1; https://www.r-project.org/) using the custom-written and freely available R package *MuscleTernary* (https://github.com/Middleton-Lab/MuscleTernary), which extends the R packages *ggtern* (ver. 3.0.0; https://cran.r-project.org/package=ggtern) and *ggplot2* (ver. 3.1.1; Wickham 2016).

We demonstrate this approach using three case studies that explore jaw muscle resultants over three scales of time. To visualize changes in muscle orientation between high and low gape during an orthally-biting feeding behavior, we plotted muscle parameters in ternary space for two specimens (1 juvenile, 1 adult) of *A. mississippiensis* by manipulating the mandibles to produce gapes of 5° (“low” gape) and 30° (“high” gape). A gape of 5° allows the animal to exert near its peak bite force, and at 30°, the jaws are at peak separation. To visualize changes in muscle orientation through ontogeny, we plotted the muscle parameters in ternary space for individuals of *A. mississippiensis* ranging from juvenile (head length = 4.9 cm) to adult (head length = 45.4 cm). To visualize changes in muscle orientation across a phylogeny, two avian taxa and one non-

avian dinosaur were plotted in ternary space and the patterns of muscle orientation were analyzed and their differences described. Non-avian and avian taxa were constructed with a gape of 20°. This value was chosen because it was the lowest gape determined to be of optimal performance in theropods by Lautenschlager (2015). Muscle resultants were plotted in ternary space to show patterns within the avian tree.

Results and Discussion

Jaw muscle resultants and gape in *Alligator mississippiensis*

As gape decreases in Alligator, muscle insertion points rotate caudoventrally and cause most muscles to exchange dorsoventral for rostrocaudal orientations during a bite (Fig. 2-3). If the jaws rotate symmetrically about the two quadratoarticular joints in a hinge-like fashion as in a sequence of orthal biting in alligators, the mediolateral component of muscles necessarily increases. The dorsoventral components of certain muscles (mAMES, mAMEM, mAMEP, and mAMP) are reoriented mediolaterally as gape decreases during a bite. In ternary space, this is represented by points moving away from the top of the triangle and toward the bottom left corner. The resultant of mPTd decreased rostrocaudally and increased mediolaterally and dorsoventrally as the gape decreased. In this instance, the point in ternary space moves away from the bottom right corner and toward the top and left, settling in the middle area of the ternary plot.

The *Alligator* results from tracing changes in gape from high to low confirm the general pattern that every muscle increased its mediolateral component as gape decreased. The increase in mediolateral components was greatest in mAMEM and least in mPTd in both the juvenile and adult alligators. This increase in mediolateral components decreases the relative vertical force that mAMEM contributes to bite force and mPTd relatively increases its contributions to bite force as it is not reoriented mediolaterally. Additionally, in both juvenile and adult mAMP retained much of its dorsoventral components (more in the juvenile than the adult). As gape decreased, the dorsoventral component of mPTd increased. Sellers et al. (2017) determined that over one third of total bite force is derived from the individual muscle forces of mPTd and mAMP. Retention of the dorsoventral components of the muscles enables the muscles to maintain high vertical bite forces even at low gapes. These results show that the decrease in dorsoventral components in many of the temporal muscles is potentially compensated for at low gapes by the increase in mPTd dorsoventral orientation.

Movement of the mandibles with respect to the cranium during feeding translates muscle insertions relative to their origins, leading to differing muscle orientations at different gape angles. As some muscle orientations are less effective at producing a given mandibular movement (e.g. jaw adduction), the gape angle can influence a system's ability to generate forces in a given direction (e.g. Eng et al. 2009; Lautenschlager 2015). A number of recent studies have further explored the effects of hypothesized ranges of gape in various taxa on modeling muscle biomechanics (e.g. Lautenschlager 2015; Montuelle and

Williams 2015). Lautenschlager (2015) simulated absolute maximum gapes of non-avian dinosaurs based on the maximum tension limit of muscle of 170% the resting length of the muscle. Lautenschlager (2015) determined that gapes of up to 79° could be possible, but gapes between 20.5° and 28° were the most optimal in non-avian theropods. Montuelle and Williams (2015) investigated maximum gape in regard to cranial kinesis in *Gekko gecko* and determined that the maximum gape was approximately 10% greater in kinesis than in akinesis.

Jaw Muscle Resultants and Ontogeny in *Alligator mississipiensis*

The shape of the skull often changes considerably throughout ontogeny (Dodson 1975) and ontogenetic changes in muscle orientation can be substantial (Fig. 2-6). Individuals of *A. mississippiensis* undergo a thousands-fold ontogenetic increase in body mass and show correspondingly dramatic shape changes to the skull over ontogeny (Busbey 1995; Erickson et al. 2003; Sellers et al. 2017). Most muscles were more dorsoventrally oriented in the juvenile alligator and more rostrocaudally and/or mediolaterally oriented in the adult specimen. So, as crocodilian skulls flatten out during ontogeny (Monteiro et al. 1997; Brochu 2001; Piras et al. 2014; Sellers et al. 2017), muscles change orientation.

Temporal muscles in individuals of *Alligator* become less dorsoventral throughout ontogeny (Fig. 2-6). A rostrocaudal increase in muscle orientation is most appreciable in the external temporal muscles

(mAMES, mAMEP, and mAMEM). Rostrocaudal increases in temporal muscles move the corresponding point in ternary space toward the top of the ternary plot. The other temporal muscle, mAMP, experiences a slight decrease in its dorsoventral component and corresponding increase in its rostrocaudal component during ontogeny. The point representing mAMP therefore moves away from the top of the ternary plot and closer to the bottom right corner over ontogeny. However, this increase is not extensive and mAMP largely retains its juvenile orientation overall as an adult. Musculus pterygoideus dorsalis (mPTd) retains and increases its rostrocaudal orientation; however, the changes associated with ontogenetic development are not as great as in the temporal muscles. The point for mPTd moves farther into the bottom right corner of the ternary diagram in this instance. The least change over ontogeny is seen in mAMP and mPTd. These two muscles retain large dorsoventral (mAMP) and rostrocaudal (mPTd) orientations.

The ternary diagrams of each muscle (Fig. 2-6) highlight these changes in the youngest and oldest specimens included in this study. Compared to the rest of the skull, the braincase and skull roof of adult alligators are more mediolaterally-positioned relative to the jaw joints and mandibles than the same structures in juveniles, which displaces the cranial attachments of temporal muscles mediolaterally. The ramus of the quadrate also shifts caudolaterally, which gives some muscles a more rostrocaudal orientation in addition to the mediolateral dimension. Similarities in mAMP and mPTd throughout ontogeny likely reflect the integral roles that these two muscles play in increasing the bite

force of alligators throughout the gape cycle regardless of specimen age. Although not done here, the changes in force each muscle produces ontogeny could also be mapped onto the size of the point.

Phylogenetic Patterns of Jaw Muscle Resultants

Jaw muscle resultants projected in ternary space are useful to show biomechanical patterns across niches, phylogeny and deep time, revealing new patterns in morphology, ecology, and evolution. Evolutionary changes in a non-avian dinosaur (*Tyrannosaurus rex*) and three avians (*Struthio camelus*, *Gallus gallus*, and *Psittacus erithacus*) show changes in muscle orientations (Fig. 2-7). *Tyrannosaurus* muscle resultants constitute a representative example of non-avian theropod dinosaur muscle orientations. Despite size differences between *Tyrannosaurus* and the avian taxa represented here, muscle orientations are size independent parameters of muscle anatomy. A number of characters separate the paleognathe bird *Struthio camelus* from the neognathe birds *Gallus gallus and Psittacus erithacus*. Huxley (1867), Bock (1963), Gussekloo and Zweers (1999), and others described cranial and postcranial characteristics of these two clades of birds. In the interest of cranial biomechanics, a number of characteristics of the bones of the mouth and the muscles that attach to these bones are of interest. Of particular interest to our ternary diagrams, the conditions of the palatine, pterygoid, and quadrate which form fused (palatine-pterygoid) and

complex (pterygoid-quadrate-orbital process) joints in *Struthio* may impact the resultant orientation of mPTd. Overall, however, the orientations of the temporal and pterygoid muscles change along the dinosaur to bird line of evolution. The muscle resultants translate from dorsoventrally to rostrocaudally oriented, and, due to expansion of the braincase (Balanoff et al. 2016; Fabbri et al. 2017), more mediolateral components are also introduced to the muscle resultants, most noticeably in mPTd.

The temporal muscles (Fig. 2-7: mAMEP, mAMES, mAMEM, and mAMP) of *Tyrannosaurus* exhibit a strong dorsoventral orientation. The mPTd of *Tyrannosaurus* is also considerably dorsoventrally oriented, but mPTd also possesses some mediolateral components that cause the muscle resultant to venture toward the center of the ternary. An appreciable rostrocaudal component also translates the resultant away from the dorsoventral corner of the ternary. In the paleognathe bird *Struthio*, the temporal muscles are almost entirely rostrocaudally oriented, but all possess appreciable dorsoventral aspects as well. The mPTd of *Struthio* is largely rostrocaudal with a small dorsoventral component. The temporal and pterygoideus muscles of the neognathe bird *Gallus gallus* are largely rostrocaudoally oriented (Fig. 2-7). The orientations of mAMEP, mAMES, and mAMP possess very little to no mediolateral components. The mPTd possesses the most mediolateral orientation of any muscles in *Gallus*. The muscle orientations of *Psittacus*, another neognathe bird, are different from *Gallus* (Fig. 2-7). *Psittacus* possesses more mediolateral muscle resultant components. The muscle orientations of the temporal muscles contain

appreciable mediolateral components, especially in mAMES and mAMEP. In *Psittacus* mPTd is highly dorsoventrally and mediolaterally oriented. The rostrocaudal component of mPTd in *Psittacus* is relatively greater than the other birds sampled and *Tyrannosaurus* as well.

Muscle resultants in non-avian theropod dinosaurs are highly dorsoventrally oriented and possess few mediolateral or rostrocaudal components. Birds, however, exhibit muscle resultants that are highly rostrocaudal and, in neognathe taxa, possess some mediolateral components in the non-temporal mPTd. Bhullar et al. (2016) described the lateral expansion of the braincase and compression of the temporal region in birds. This combination of expansion and compression causes muscle insertions of the temporal region to be more lateral than, but ventral to, the braincase in birds. The translation of muscle resultants to a more rostrocaudal orientation is likely related to this expansion of the braincase in birds. Differences between paleognathe and neognathe birds are more subtle than those between non-avian and avian theropods. For example, the differences in mPTd among *Struthio* and *Gallus* and *Psittacus* reflect the different shapes of the palatal complex that separate the Paleognathae and Neognathae clades of birds as described by Huxley (1867), Bock (1963), Gussekloo and Zweers (1999), and others. The temporal muscles, though, are fairly similar in their rostrocaudal orientations. The trends described here are shown with a small sample size, however; we are confident that an increase in sample size,

specifically dinosaur taxa more closely related to birds than *Tyrannosaurus*, will only serve to bolster these trends among non-avian dinosaurs and birds.

Muscle Orientation in Hard Biting Taxa

Finally, we demonstrate that high bite forces can be differentially produced by highly diverse taxa and that the contributing muscles can be described using ternary plots of jaw muscle resultants. Numerous vertebrate species have evolved increased bite forces in order to dispatch prey (*Alligator*, *Tyrannosaurus*) or to husk tough food item (*Psittacus*), and in these cases, we expect the skulls to have increased vertical components of jaw muscle resultants. This case study considers the hardest biting fossil and extant taxa (*Tyrannosaurus rex* and *Alligator mississippiensis*). A third taxon, *Psittacus*, also produces relatively high bite forces compared to other avian taxa (e.g. Sustaita and Hertel 2010; Carril et al. 2015). The three taxa produce relatively high bite forces with different cranial configurations: *Alligator* possesses a dorsoventrally flattened, mediolaterally wide skull whereas *Tyrannosaurus* and *Psittacus* both possess dorsoventrally tall and mediolaterally wide skulls.

Despite possessing a dorsoventrally short skull, *Alligator* temporal muscles possess appreciable dorsoventral and mediolateral components (Fig. 2-8). The temporal muscles of *Alligator* are relatively weaker than mPTd with the exception of mAMP (See figs. 3 and 4). These two muscles, mPTd and mAMP, possess extensive rostrocaudal and dorsoventral components respectively. The force of mPTd and mAMP together constitute approximately 35% of the total bite

force produced by *Alligator* (Sellers et al. 2017). *Tyrannosaurus* and *Psittacus* also both exhibit very few mediolateral muscle components except in mPTd. The temporal muscles of *Tyrannosaurus* and *Psittacus* are largely dorsoventral and rostrocaudal, respectively. The exception to large rostrocaudal components in *Psittacus* is in mPTd, which exhibits a highly dorsoventral, and appreciable mediolateral, orientation. *Tyrannosaurus* has a greater rostrocaudal orientation in mPTd than in any other muscle. In *Psittacus* the dorsoventral components of mPTd are relatively greater than the dorsoventral components of mPTd in *Tyrannosaurus*.

The highly vertical muscle orientations found here in diverse adductor muscles of *Alligator* (mAMP), *Tyrannosaurus* (mAMEP, mAMEM, mAMES, and mAMP), and *Psittacus* (mPTd) show that hard biting archosaurs employ different biomechanical strategies to generate higher bite forces. As we observed in the gape ternaries, mPTd in *Alligator* increases its dorsoventral component as gape decreases, contributing a larger dorsoventral component to low gape. *Alligator* produces high bite forces largely using one highly dorsoventrally oriented muscle (mAMP) and one rostrocaudally oriented muscle (mPTd) that increases its dorsoventral orientation at low gapes, potentially to compensate for decreases in dorsoventral orientations elsewhere in the skull. The dorsoventral bite force production of *Tyrannosaurus* is largely the result of

the temporal muscles. *Psittacus*, however, employs a pterygoideus muscle (mPTd) to produce its high bite forces.

Conclusions

The case studies presented here illustrate that ternary diagrams are a powerful means of conveying complex muscle orientation data in comparative contexts across behavior, ontogeny, and phylogeny. Our cases identify trends in muscle orientation changes across gape in juvenile and adult specimens as well as ontogenetic changes within the same lineage (*A. Mississippiensis*). Gape decreases during biting in *Alligator* change the resultant orientation of muscles in both juvenile and adult specimens to a more mediolateral orientation. Over ontogeny, however, the orientations of the muscles are translated rostrocaudally and mediolaterally. In the dinosaur-avian lineage, muscle resultants changed across taxa such that the resultant orientations were translated rostrocaudally and mediolaterally. Finally, we showed that among archosaurs, hard-biting taxa do so with disparate arrangements of jaw muscles. These kinds of data will enable us to follow the evolutionary changes that resulted in different anatomical solutions to functional demands. Future studies can make use of these types of morphological variables to study the convergence of bones and muscles across guilds of animals. Studies that estimate ancestral states and evaluate the tempo of adaptive radiations of animals that modify the feeding apparatus (e.g., cichlids) could also benefit from using ternary diagrams to present data and results.

Table 2-1. Scan parameters of specimens used in this study.

Taxon	Specimen number	Voxel Size (mm)	Skull length (mm)	Scanner Used
Alligator mississippiensis	MUVC AL 031	0.083^3	48	Siemens INVEON164 SPECT/CT
Alligator mississippiensis	MUVC AL 622	0.160^2 x 0.5	99	GE LightSpeed VCT
Alligator mississippiensis	MUVC AL 612	0.250^2 x 0.5	203	GE LightSpeed VCT
Alligator mississippiensis	MUVC AL 024	0.430^2 x 0.625	269	GE LightSpeed VCT
Alligator mississippiensis	MUVC AL 700	0.510^2 x 0.5	333	GE LightSpeed VCT
Alligator mississippiensis	MUVC AL 008	0.570^3	454	Siemens Somatom Definition Scanner
Gallus gallus	MUVC AV 003	0.092^3	68	Siemens INVEON164 SPECT/CT
Struthio camelus	OUVC10659	0.036^2 x 0.1	184	General Electric LightSpeed Ultra Multislice
Psittacus erithacus	MUVC AV 042	0.063^3	66	Siemens INVEON164 SPECT/CT
Psittacus erithacus	MUVC AV 092	0.063^3	66	Zeiss Xradia 510 Versa 3D
Tyrannosaurus rex	BHI 3033	0.625^3	1470	General Electric LightSpeed Ultra Multislice

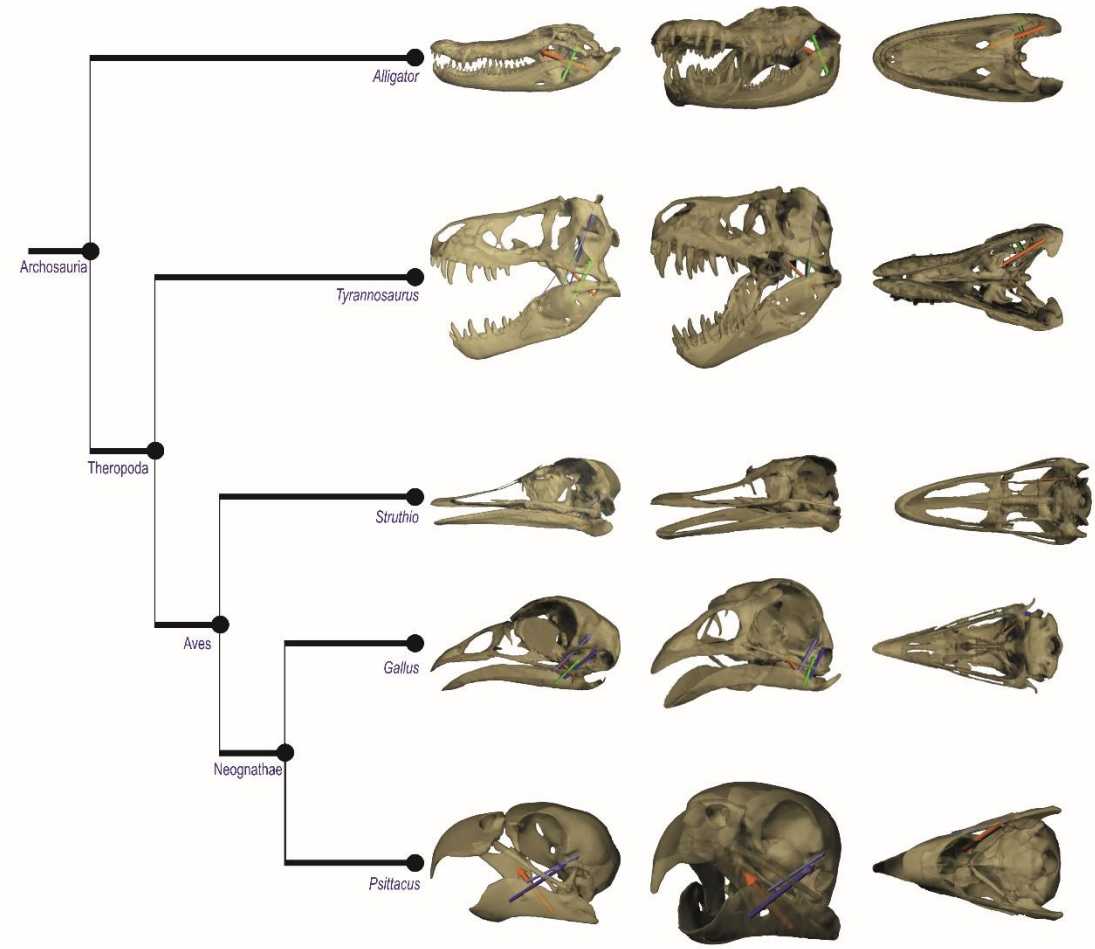

Figure 2-1. Phylogenetic tree of archosaur taxa in this study. Taxa are shown in left lateral (left), oblique (center), and ventral (right) views. Models were generated in Maya and are shown with resultants presented in this study.

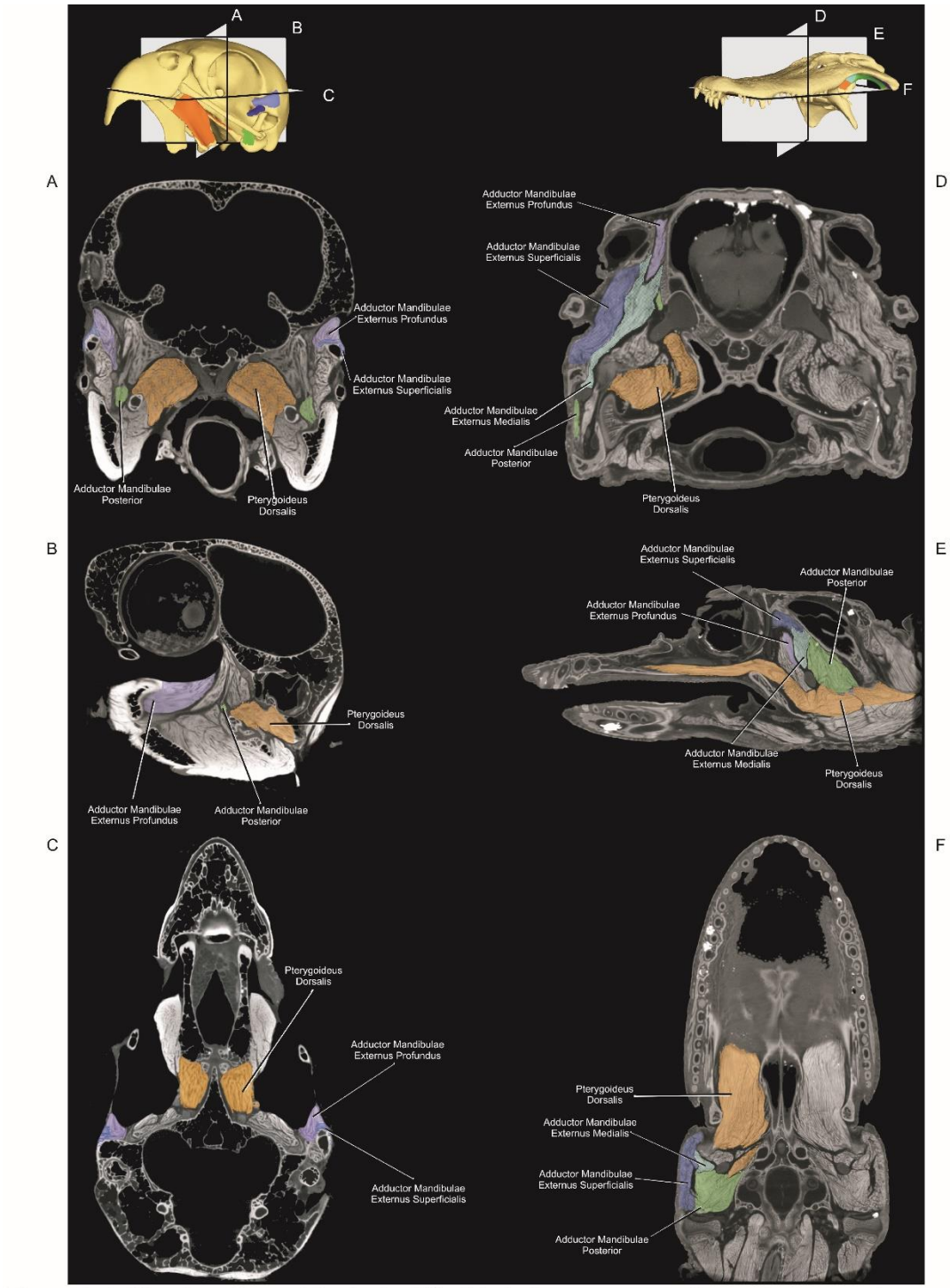

Figure 2-2. Muscles pictured *in situ* in diffusible iodine contrast-enhanced computed tomography (DiceCT). Grey parrot (*Psittacus erithacus*; MUVCAV092) and alligator (*A. mississippiensis*; MUVCAL031) are used to show muscles of the cranium discussed in this study. Muscles include m. adductor mandibulae externus superficialis (mAMES), m. adductor mandibulae externus medialis (mAMEM), m. adductor mandibulae externus profundus (mAMEP), m. adductor mandibulae posterior (mAMP), and m. pterygoideus dorsalis (mPTd). Images are shown in coronal **(A and D)**, parasagittal **(B and E)**, and horizontal **(C and F)** planes; the legend for the planes in each taxon is at the top of the respective column of anatomical images.

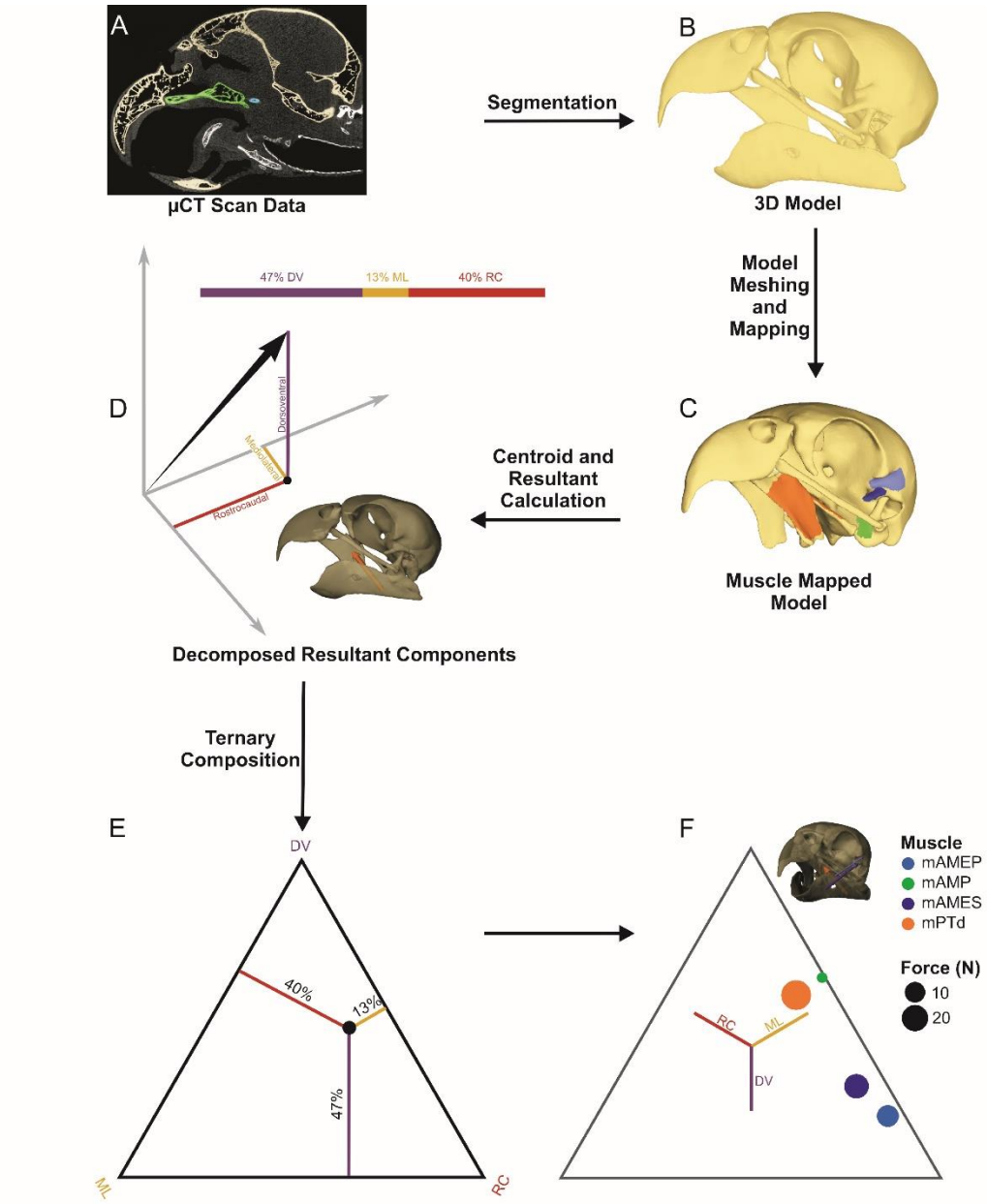

Figure 2-3. Illustrated description of ternary diagram construction. **(A)** Computed tomography (CT), or microcomputed tomography (μCT) where appropriate, data is collected. Data are then segmented **(B)** and reconstructed, smoothed, and meshed to create a finite element model (FEM; **C**). Muscles are attached to the finished FEM and the coordinates of the centroids of attachment areas are determined. The centroids are employed to determine a muscle resultant vector between the two attachment centroids of a muscle; one on the mandible, the other on the cranium. **(D)** The resultant vectors are then decomposed into rostrocaudal, mediolateral, and dorsoventral components. The resultant vector can be described in terms of what proportion of the total each component accounts for, as in **(D)**, in which the dorsoventral component accounts for 47% of the resultant vector, the mediolateral component accounts for 13%, and the rostrocaudal component accounts for 40%. **(E)** The resulting point in space is then plotted on a ternary diagram using the components detailed above. **(F)** The final product of this process results in multiple points representing the 3D orientations of muscle resultants plotted in 2D space that enable researchers to view and appreciate the region in 3D space which muscles occupy.

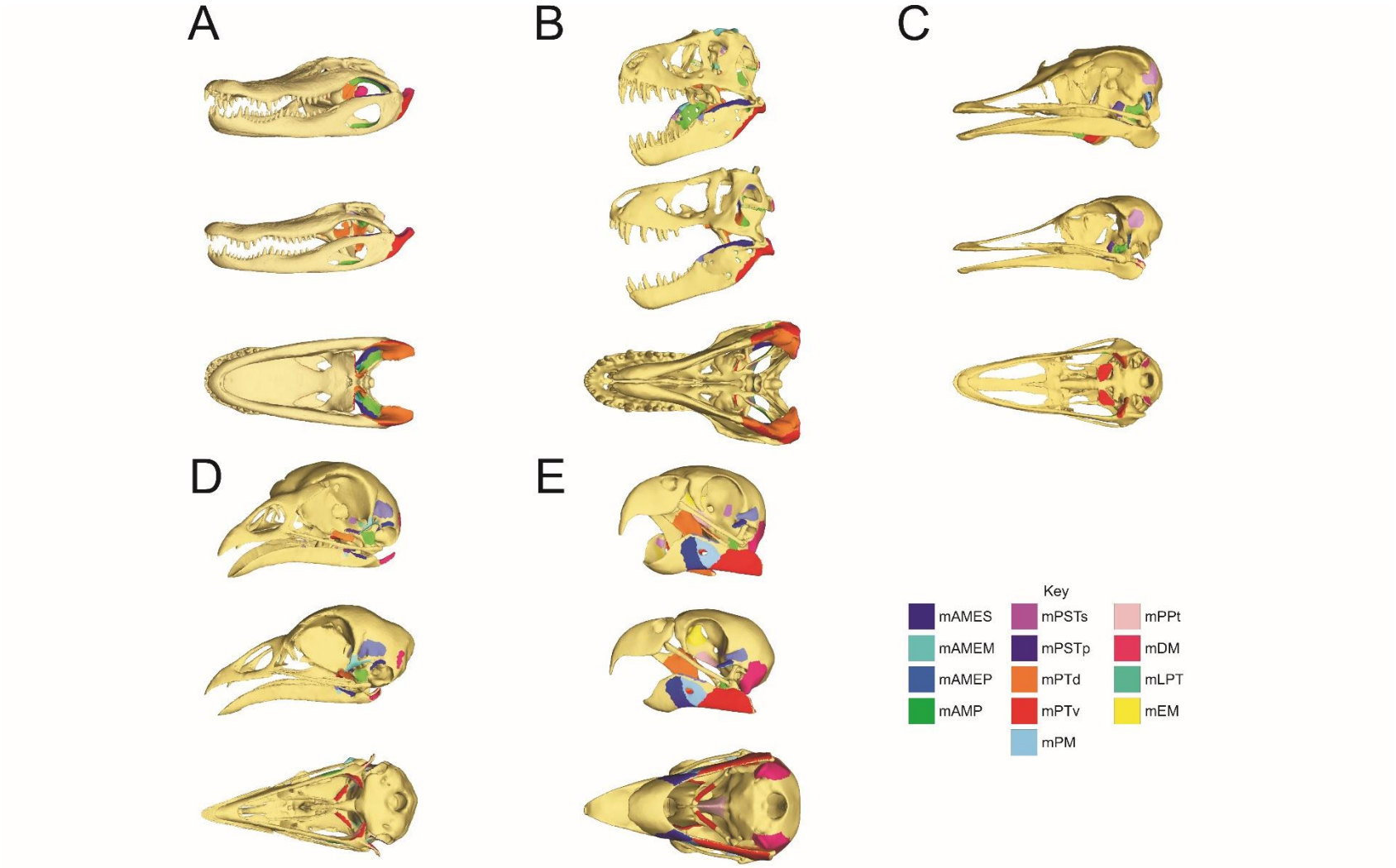

Figure 2-4. Muscle maps of models used to analyze muscle resultants in this study. Oblique (top), left lateral (middle), and ventral (bottom) views of muscle mapped models are shown. Models are arranged taxonomically: **(A)** *Alligator mississippiensis*, **(B)** *Tyrannosaurus rex*, **(C)** *Struthio camelus*, **(D)** *Gallus gallus*, and **(E)** *Psittacus erithacus*.

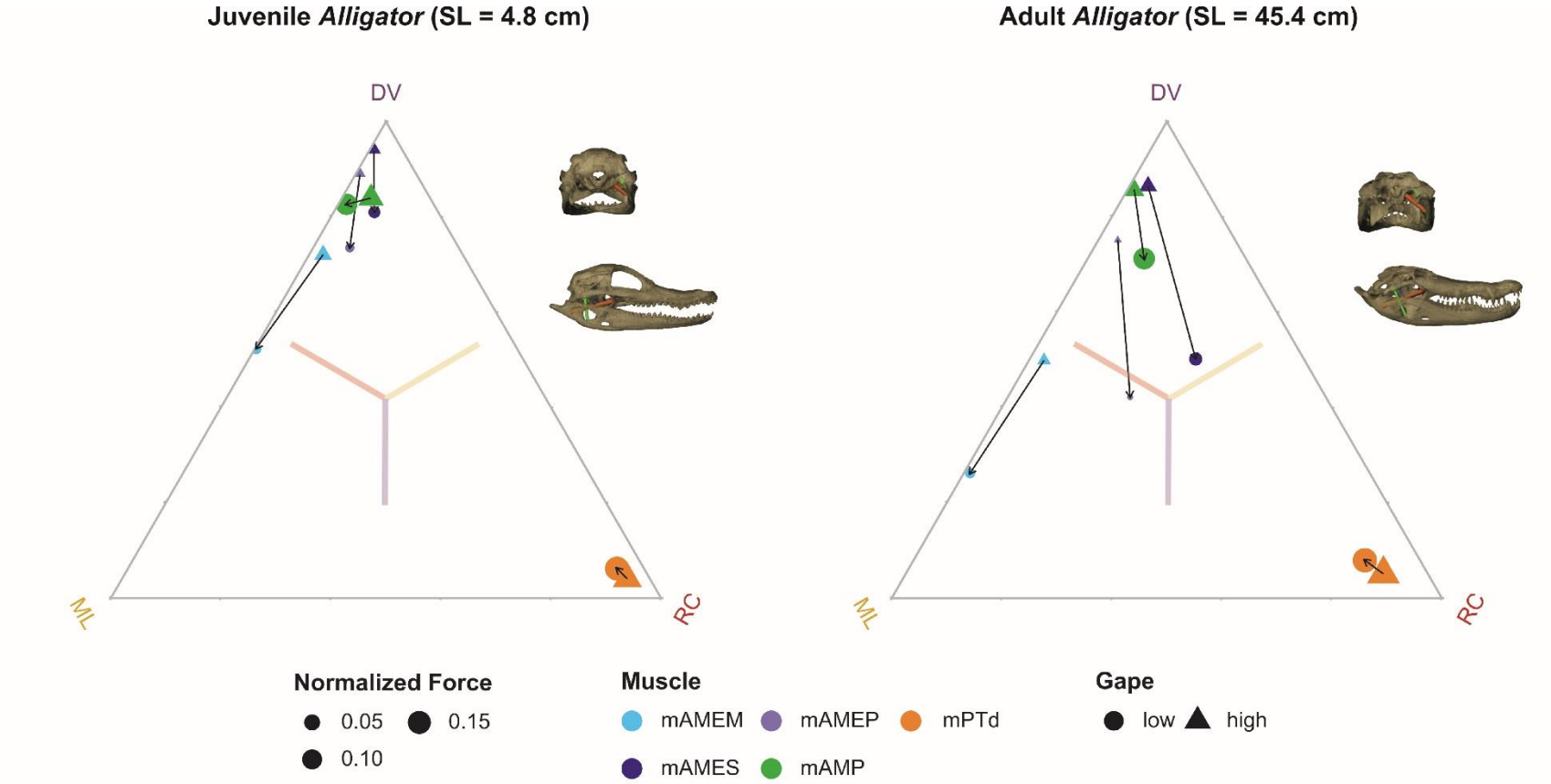

Figure 2-5. Changes in muscle orientations during a gape cycle in *A. mississippiensis* (MUVCAL008 and MUVCAL031). Orientations of muscles at 30° and 5° of gape (high to low gape) are represented in ternary space. Arrows point from orientations at low gape (circles) to the orientation of the corresponding muscle at high gape (triangles). For both specimens, the normalized force of each muscle represents the force of that muscle as a proportion of total jaw muscle force. Changes in orientation are most appreciable in the temporal muscle complex (mAMES, mAMEM, mAMEM, and mAMP). The mPTd undergoes little to no change in orientation during a gape cycle.

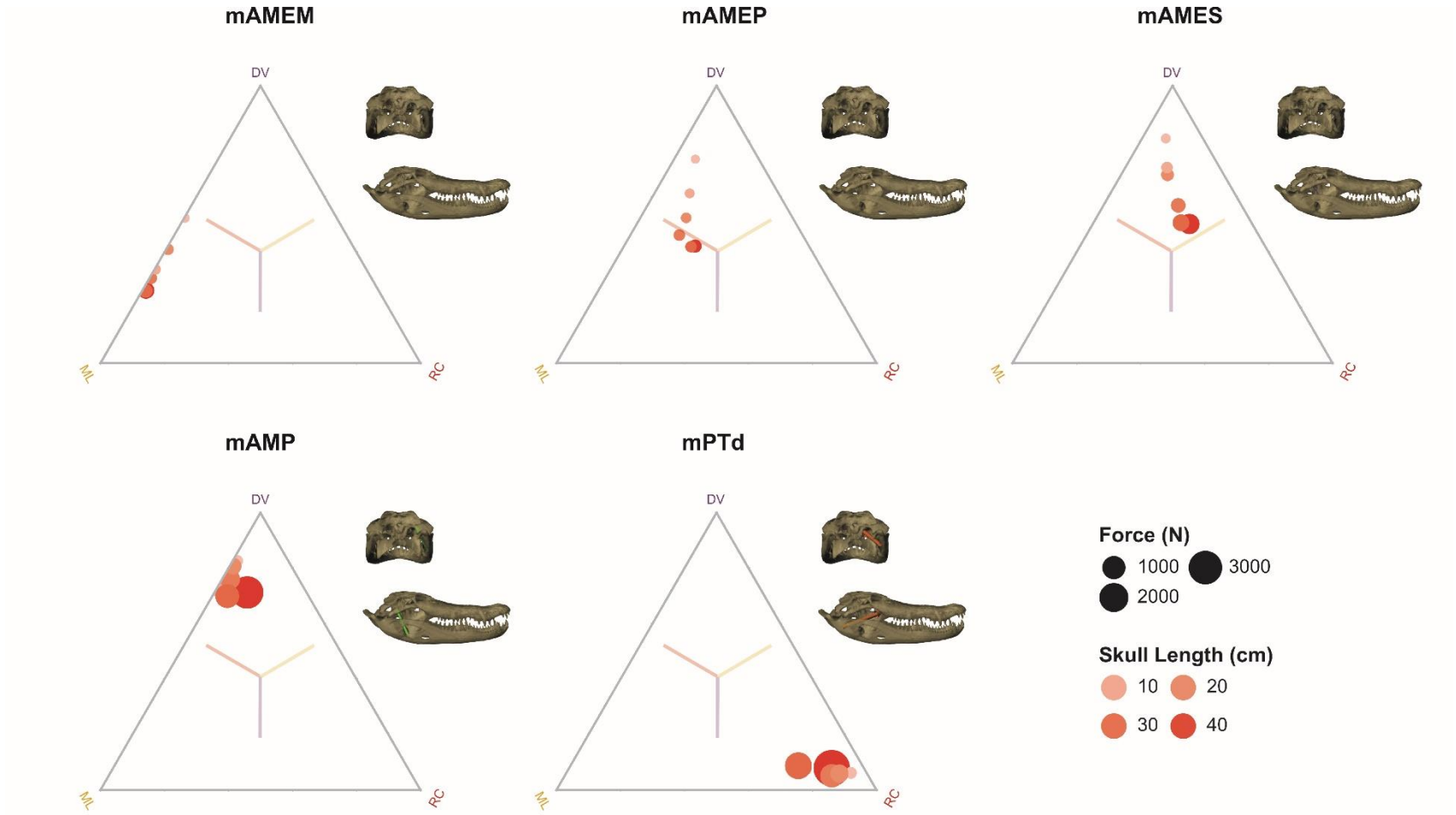

Figure 2-6. Ontogenetic changes in muscle orientation in *A. mississippiensis* (MUVCAL008, MUVCAL024, MUVCAL031, MUVCAL612, MUVCAL622, and MUVCAL700). Changes over a growth series of *A. mississippiensis* are represented in ternary space with points representing muscle belly orientation. Points are depicted ranging from lighter to darker red colors which represent smaller to larger individuals respectively. Orientations of temporal muscles in *A. mississippiensis* become more rostrocaudal or mediolateral as alligators mature and become larger. Musculus pterygoideus dorsalis does not follow a linear path throughout ontogeny, but largely retains a highly rostrocaudal orientation as individuals grow from hatchling to adult.

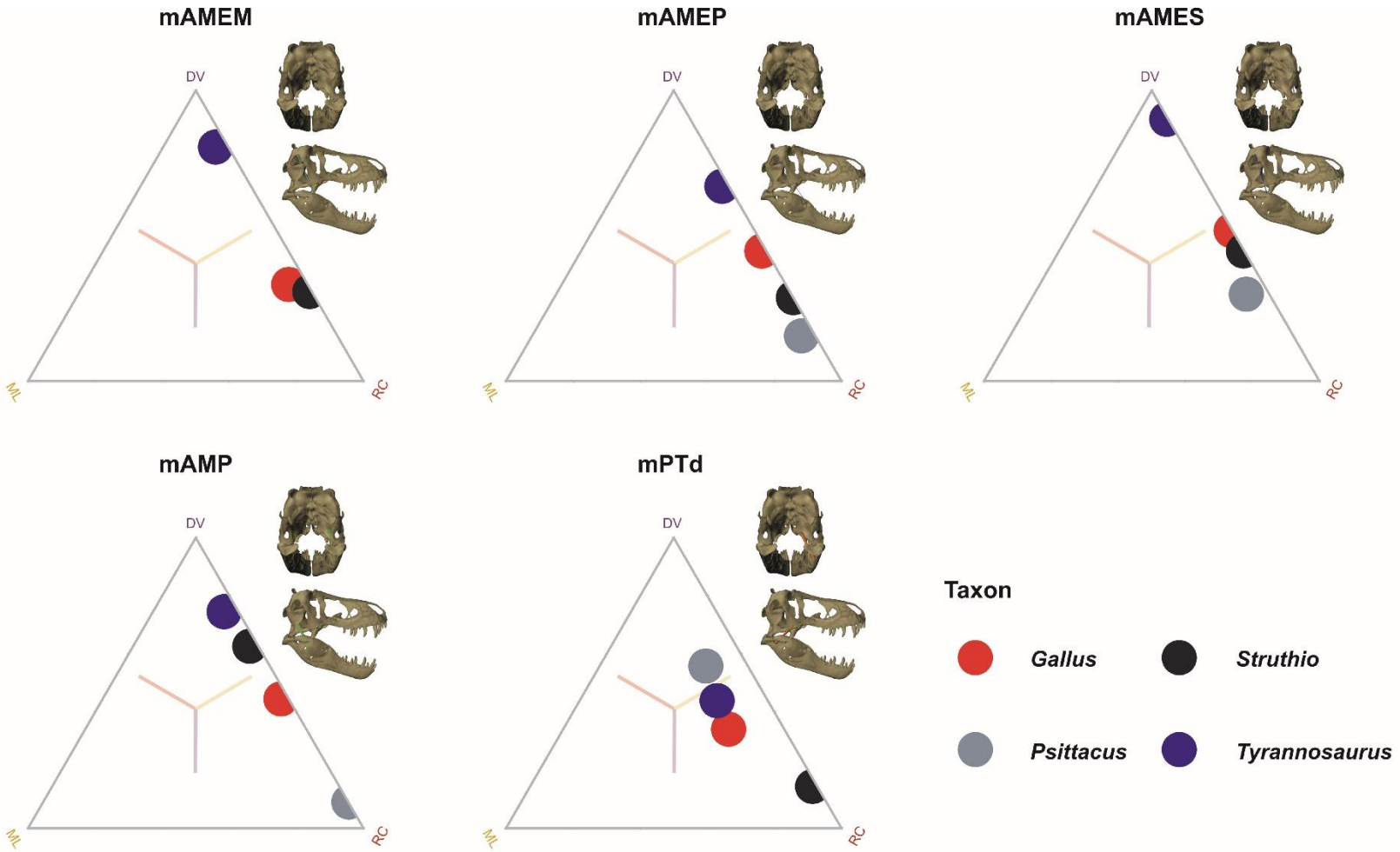

Figure 2-7. Changes in muscle orientation during the evolution of theropod dinosaurs (T*yrannosaurus rex* BHI 3033) and birds (*Struthio camelus* OUVC10659; *Gallus gallus* MUVCAV003; *Psittacus erithacus* MUVCAV042). *Tyrannosaurus* temporal muscles are highly dorsoventrally oriented whereas avian temporal muscles are more rostrocaudally oriented. The muscle mPTd retains a mainly rostrocaudal orientation in the ostrich (*Struthio camelus*), but is appreciably mediolateral in parrot, chicken, and *Tyrannosaurus*.

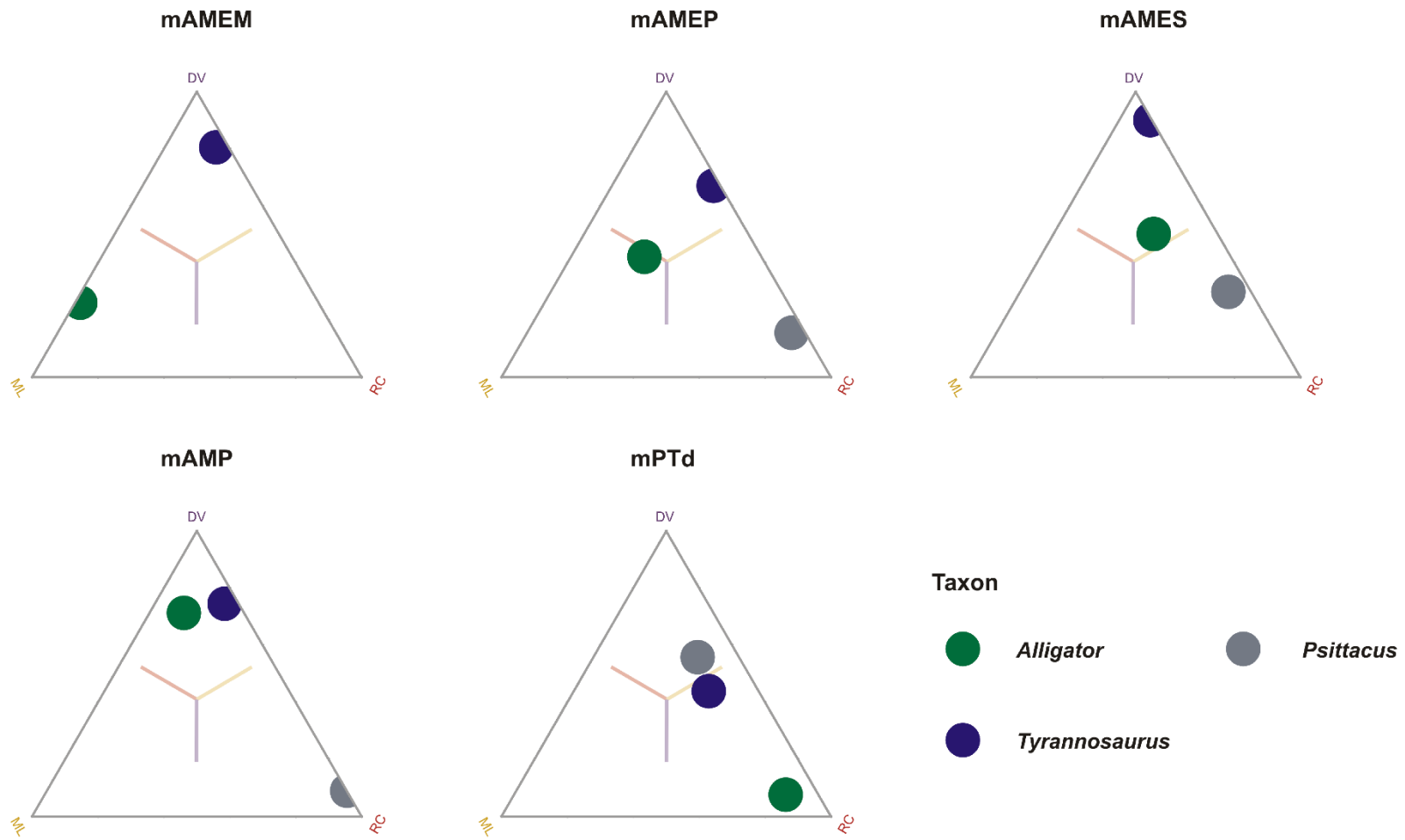

Figure 2-8. Resultants of muscles of hard biting taxa. The muscle orientations of *Alligator mississippiensis*, *Tyrannosaurus rex*, and *Psittacus erithacus* are presented. *Alligator* possesses more mediolateral resultant components than *Tyrannosaurus* or *Psittacus*. *Tyrannosaurus* muscles are highly dorsoventrally oriented and *Psittacus* muscles are highly rostrocaudally oriented. In all three taxa mPTd is uniquely oriented with respect to the temporal musculature. In *Alligator* mPTd is highly rostrocaudally oriented and possesses fewer mediolateral or rostrocaudal components. In *Tyrannosaurus* and *Psittacus* mPTd is highly dorsoventrally oriented and exhibits greater mediolateral orientation than other *Tyrannosaurus* and *Psittacus* muscles.

Chapter 3

Palatal biomechanics and its significance for cranial kinesis in *Tyrannosaurus rex*

Introduction

Vertebrate feeding adaptations resulted in a diversity of cranial structures and functions, many of which led to changes in palatal functional morphology. Despite these modifications, many reptiles maintain a series of linkages between the palate and braincase that often permit cranial kinesis. Cranial kinesis manifests as a spectrum of palatal motions among lineages (Versluys, 1910; Bock, 1964, 1999; Zusi, 1984, 1993; Gussekloo, 2000; Holliday and Witmer, 2008). Because many of the joints linking the palate to the braincase remain unfused, the skulls of many extinct species of dinosaurs, crocodylomorphs, and other fossil reptiles have also been hypothesized to have had various forms of cranial kinesis (Rayfield, 2005; Holliday and Witmer, 2008). For example, *Tyrannosaurus rex*, which has plesiomorphic, ball and socket shaped palatobasal and otic joints has been hypothesized by different authors to have possessed one of several forms of cranial kinesis (Molnar, 1998; Rayfield, 2004; Larsson, 2008). A functional paradox remains: why do mature individuals of one of the world's most forceful biting, osteophagus animals (Gignac and Erickson, 2017) ever known maintain flexible joints when the hardest biting taxa of other terrestrial lineages (e.g., crocodile, tiger, and hyena; Erickson et al., 2003; Wroe

et al., 2005; Tseng and Binder, 2010) suture their cranial elements to form rigid skulls?

Kinetic competency of *Tyrannosaurus* has been explored previously and interpretations and methods vary. Osborn (1912) first remarked on the seemingly mobile nature of particular condylar joints but suggested the surrounding bones limited any particular movement. Also citing the condylar otic joint between the quadrate and squamosal, Molnar (1991, 1998) instead inferred limited streptostyly (rotation of the quadrate about the otic joint) in *Tyrannosaurus*. Rayfield (2004, 2005a, b) inferred numerous sutural and condylar joints within the palate and face of *Allosaurus*, *Tyrannosaurus*, and other theropods to be capable of movement following finite element analysis of patterns of stresses. Larsson (2008) extended discussion of *Tyrannosaurus* kinesis and streptostyly with new details on the condylar nature of the palatobasal joint. Conversely, Holliday and Witmer (2008) described *Tyrannosaurus* and many non-avian dinosaurs as being partially kinetically competent, meaning that these taxa possess patent otic and palatobasal joints as well as protractor musculature necessary to mediate powered (driven by muscle force rather than being passive) kinesis. However, these taxa lack permissive linkages in the skull that would enable gross movements of the palate or face. Regardless, these hypotheses have yet to be fully tested in a phylogenetic functional context using 3D modeling techniques.

Permissive linkages in lizards and birds result from the elimination of bones comprising the postorbital and temporal bars, development of craniofacial

hinge joints (flexion zones), and the elimination of the epipterygoid in birds. These morphological changes manifest differently in these two clades. Species of lizards exhibit a diversity of often coupled kinetic behaviors including, but not limited to streptostyly, mediolateral motion (MLM) at the palatobasal joint, and mesokinesis (flexion of the facial skeleton about the frontoparietal joint; Rieppel 1978; Smith and Hylander 1985; Herrel et al., 2000; Metzger 2002, Evans 2003). Many species of birds, including ducks, parrots, and many neoavians also employ streptostyly and prokinesis (elevation of the beak at the craniofacial hinge) as well as concomitant fore-aft motion (FAM) about the palatobasal joint (Hofer 1950; Burton 1974a; 1974b; Hoese and Westneat 1996; Bout and Zweers 2001; Dawson et al., 2011). Although the palatobasal joint and likely other palatocranial joints are unsutured, they lack mobility in many species of lepidosaurs (Metzger, 2002; Curtis et al., 2010; Jones et al., 2011), birds (Zusi, 1993; Gussekloo, 2005), and non-avian dinosaurs (Holliday and Witmer, 2008).

We use two species of extant, kinetically competent reptiles, tokay geckos (*Gekko gecko*) and grey parrots (*Psittacus erithacus*), to model, frame, and test hypotheses of function in the extinct reptile species *Tyrannosaurus rex*. Tokay geckos eliminated the upper and lower temporal bars of their skulls, have large jaw muscles relative to their body size, strut-like pterygoid and epipterygoid bones, and palates connected to the braincase through synchondrodial (cartilaginous without a synovial cavity) otic and diarthrodial (cartilaginous with a synovial cavity) palatobasal joints (Table 3-1; Rieppel, 1984; Herrel et al., 2007; Payne et al., 2011; Mezzasalma et al., 2014; Daza et al., 2015). Herrel et al.

(1999, 2000) and Montuelle and Williams (2015) found *Gekko* to exhibit a combination of mediolateral and fore-aft streptostyly, long axis rotation of the palate, and bending of the palate about hypokinetic (palatine-pterygoid suture) joints and the mesokinetic hinge. Because the long axis rotation of the palate requires it to also swing mediolaterally, we modeled the palate accordingly in a mediolateral movement as internal palatal element kinematics remain undescribed.

Grey parrots lack upper temporal bars and epipterygoids, have strut-like lower temporal bars, pterygoids, and quadrates, and articulate the palate to the braincase via diarthrodial otic and analogous 'palatobasal' joints between the palate and parasphenoid rostrum (Bailleul and Holliday, unpublished data). Parrots employ prokinesis (Zusi, 1967) in which fore-aft motion of the palate occurs at the otic and palatobasal joints to elevate the beak about the craniofacial hinge. These movements are facilitated by large protractor and adductor muscles (Hofer, 1949, 1950), including the neomorphic psittacid pseudomasseter (mPM) and ethmomandibularis muscles (mEM; Tokita 2003, 2004; Carril et al., 2015).

Given previous research (Molnar, 1991, 1998; Carr, 1999; Rayfield, 2004, 2005; Snively et al., 2006; Molnar, 2008; Holliday, 2009; Bates and Falkingham, 2012; Gignac and Erickson, 2017), we know enough about *Tyrannosaurus* cranial anatomy to rigorously explore hypotheses of cranial behavior and function and examine the kinetic capacity of these forcefully-biting ancient predators. The skulls of *Tyrannosaurus* and many other non-avian theropod dinosaurs maintain

both upper and lower temporal bars, epipterygoids, dorsoventrally thin palatal elements, and robust scarf joints (a smooth and angled joint between two elements) between elements of the dermatocranium and palate (Molnar, 1991, 1998; Carr, 1999; Snively et al., 2006), all of which are features considered to limit cranial mobility (Holliday and Witmer, 2008). Regardless, Molnar (1991), Rayfield (2005), and Larsson (2008) hypothesized fore-aft motion via streptostyly in *Tyrannosaurus* based on the ball and socket-shaped (i.e., condylar) otic and palatobasal joints. These joints are spanned by large adductor muscles laterally (Molnar, 2008; Holliday, 2009; Bates and Falkingham, 2012; Gignac and Erickson, 2017) as well as large, tendinous protractor muscles medially (Holliday and Witmer, 2008; Holliday, 2009).

Here we test the performance of *Tyrannosaurus* finite element models compared to those of known, kinetically competent *Gekko* and *Psittacus* models. Accurately modeled jaw muscle loads and joint articulations were integrated into each model in akinetic (neutral), MLM (mediolateral motion of the palate about the otic and palatobasal joints) and FAM (fore-aft motion about the otic and palatobasal joints postures). Strains of the models were analyzed qualitatively and quantitatively to determine the optimal and, therefore, most likely posture of the *Tyrannosaurus* palate. A better understanding of the loading environment of the skull and kinetic competency of extinct dinosaur species like *Tyrannosaurus rex* illuminates vertebrate adaptations for feeding, the evolutionary development

of cranial joints, and the origins of avian-style cranial kinesis from non-avian theropod dinosaurs.

Methods

Finite element modeling is a common approach used to evaluate biomechanical performance of dinosaur skulls (Rayfield, 2004; Moazen et al., 2009; Lautenschlager et al., 2013; Lautenschlager, 2015). Although many studies employ models of taxa for specific instances of feeding behaviors, few explore changes in gape and other excursions of cranial elements during feeding cycles (e.g., Moazen et al., 2008; Lautenschlager, 2015). Here, however, we test the performance of several different kinetic postures across three taxa. The heads of *Psittacus erithacus* (MUVC AV042) and *Gekko gecko* (MUVC LI044) were scanned in a Siemens INVEON SPECT/CT (VA Biomolecular Imaging Center, Columbia, MO) with voxel sizes of 63.4 µm and 92.1 µm, respectively. A 1/6-scale model of *Tyrannosaurus rex* (BHI 3033) was scanned in a General Electric LightSpeed Ultra Multislice CT scanner (voxel size of 625 µm, 120 kV, 170 mA, OhioHealth O'Bleness Memorial Hospital, Athens, OH). CT data were segmented in Avizo Lite 9 (FEI Company, Hillsboro, OR).

Bones of the palate and the rostrum (in *Gekko* and *Psittacus*) were manually segmented using thresholds unique to each scan separately from bones of the neurocranium and dermatocranium in each model, allowing for postures to be modified (See Table 1 for segmented elements). Stereolithographical models (STL files) were generated from segmentation and

were cleaned and repositioned in anatomical postures of hypothesized kinesis in Geomagic (3D Systems, Rock Hills, SC). Skeletal elements were joined together prior to construction as finite element models (FEM). Finite element models were constructed in Strand7 (Strand7 Pty Ltd, Sydney, Australia) using four point tetrahedral elements. Joints between the palate and braincase, and kinetic hinges in *Gekko* and *Psittacus*, were then broken to simulate mobile joints. Connections between the now open elements were linked to one another with beams assigned the properties of joint materials. Beam number within the joint areas was dependent on the size of the articular surfaces of bones forming the joints. Beams were placed between nodes with one node hosting one beam.

Postural Kinetic Competency (PKC) models were constructed using the BoneLoad workflow (Grosse et al., 2007; Davis et al., 2010; Sellers et al., 2017, Fig. 3-1). BoneLoad distributes the estimated muscle forces in each postural model across the attachment sites of muscles which are in turn used to load the model. Joint materials were modeled using links and beams to emulate different articular tissue material properties (e.g., suture/ligament, hyaline cartage, bone). This approach differs from other models that included ligamentous connections modeled as continuous layers of brick elements with different material properties to emulate cranial sutures (Moazen et al., 2009; Jones et al., 2017; Reed et al., 2011; Curtis et al., 2013). In general, the models built here using linkages are more yielding than previous models. Greater flexibility in our modeled joints should allow for better dissipation of forces in biologically accurate biomechanical

environments than fully fused FEMs (e.g., Moazen et al., 2009; Jones et al., 2011).

Models were built in three positions which approximate different kinetic motions: akinesis (hereafter referred to as the neutral posture), FAM, and MLM. Each model was constructed to exhibit a neutral posture by opening the mandible to a 20° gape without shifting either the quadrate or palate. A posture resulting from FAM (prokinesis + streptostyly), and a posture resulting from MLM (streptostyly + hypokinesis + mesokinesis) created by initially shifting the quadrate at the otic joint 5° rostrocaudally and 5° medially (Fig. 3-2). Previous studies detected quadrate rotations between 5° and 10° in extant taxa (Hoese and Westneat 1996; Herrel et al. 1999; Metzger 2002; Montuelle and Williams 2015; Claes et al., 2016). A movement of 5°, therefore, is a conservative estimate of streptostylic quadrate movement.

To model soft-tissue attachment sites, models were imported to Strand7 and material properties assigned to specific regions of the models. All models were assigned isotropic materials during construction and identical bone properties (E = 13.65 GPa *sensu* Rayfield 2011; v = 0.3). Articulated palatobasal and otic joints, the frontoparietal joint, and the craniofacial hinge were built by eliminating bricks in the joint space and linking portions of the model to one another using structural beams attached to the facing sides of the joints. Other potentially mobile joints, such as the epipterygoid-pterygoid in the gecko, or the quadrate-quadratojugal joint and palatine-maxillary joint in the parrot, were left fused to focus on strains at primary locations of kinesis in the palate and

quadrate. Joints were reconstructed in *Psittacus* and *Gekko* using beam properties simulating rat cranial sutures (E = 2.35 MPa, v = 0.3; Chien et al. 2008). *Tyrannosaurus* joints were reconstructed using beam properties simulating canine patellar tendon (E = 4.57 MPa, v = 0.3; Haut et al. 1992). Joint materials of different-sized animals were used in an attempt to mimic joints of closer physiological size in the taxa of interest. Sensitivity analysis was conducted using the sutural materials of the *Tyrannosaurus* model in *Psittacus* to determine the role these values may have played in the analysis.

Muscle attachment sites were mapped onto models using information from dissection, observation, and the literature (Hofer, 1950; Abdala and Moro, 1996; Herrel et al., 1999; Tokita, 2004; Holliday, 2009; Carril et al., 2015; Fig. 3-3). Anatomical details for muscle fiber length and pennation of fibers relative to central axes were measured in *Gekko* and *Psittacus* and compared to the literature (e.g., Herrel et al., 1999; Hieronymus, 2006; Carril et al., 2015; Table 2) to estimate physiological cross–sectional area (PCSA) using equation 1 (Sacks and Roy, 1982):

$$PCSA = \frac{V_m}{l_f} \cdot \cos(\theta) \quad (1)$$

where V_M is the muscle volume, l_f is the fiber length, and θ is the pennation angle of the muscle.

The pennation angles of *Tyrannosaurus* jaw muscles were estimated to fall within known pennation angles of alligator, bird, and lizard jaw muscles based on visible osteological correlates suggestive of tendon attachments as well as

coarse phylogenetic bracketing. Hence, muscles with pennate extant homologs and informative osteological correlates were conservatively modeled as more pennate than other muscles. For example, m. adductor mandibulae externus profundus (mAMEP), which is the large muscle that attaches to the dorsotemporal fossa and is relatively pennate in most vertebrates, was modeled with 20° pennation angle, whereas m. adductor posterior (mAMP), which attaches to the body of the quadrate, was modeled as being largely parallel fibered (5° pennation angle) given the lack of clear tendinous scars on the quadrate in *Tyrannosaurus* and its relatively simple architecture in birds, non-crocodyliform suchians (Holliday and Witmer, 2009), and archosaur outgroups (e.g., lizards; Haas, 1973; Holliday and Witmer, 2007; Holliday, 2009). All muscles were modeled to have fiber lengths that were 2/3 the length of the muscle itself, which is also generally conservative across vertebrates (Bates and Falkingham, 2018).

To further justify our phylogenetically-bracketed estimates of jaw muscle architecture in *Tyrannosaurus*, we developed a sensitivity analysis to explore the effects of fiber length and pennation on PCSA. Because fiber length and pennation angle are the physiological parameters that modulate the force predicted from anatomical cross-sectional area for a given muscular geometry, PCSA and, by extension, muscle force is a function of fiber length and pennation alone. In theory, pennation can vary from 0° asymptotically to 90°, and fiber length can vary from 1 asymptotically to 0. To explore the parameter space of pennation and fiber length, we calculated the PCSA of each jaw muscle of

Tyrannosaurus for 100 values of pennation ranging from 0° to 89.1°and 100 values of fiber length ranging from 0.01 to 1, for a total of 10,000 combinations per muscle. This range captures the full potential range of the factors that contribute to PCSA in *Tyrannosaurus*.

Muscle volume, fiber architecture (Table 2), and muscle attachment centroids were then used to calculate 3D resultants of jaw muscles as well as ultimately distributed loads on the FEM *sensu* Sellers et al. (2017) using equation 2:

$$F_M = PCSA \cdot T_{specific} \quad (2)$$

where $T_{specific}$ is specific tension (Porro et al., 2011), and F_M is muscle force. The resultant muscle force and muscle attachment centroids serve as muscle parameter input in the BoneLoad workflow. Models were all constrained at bilateral, caudal bite points. All models are constrained by single nodes at the mandibular condyle of the quadrate in all planes of movement and at a series of occipital attachments near the approximate center of muscle attachments, *sensu* Snively and Russell (2007). Muscles were activated simultaneously at maximal force in each model similar to the methods used by Bates and Falkingham (2012) to estimate the bite force of *Tyrannosaurus*. Muscle activation patterns were also addressed during post hoc testing. Strain data were analyzed across the cranium and within skeletal elements to describe kinetic competency and the likelihood of kinetic postures in the analyzed taxa. Tetrahedral (“brick”) strains were sampled in specific regions of the skeletal elements of the palate. Surface tetrahedral in

regions of interest were selected as pools to sample from which included anterior, middle, and caudal portions of the palatine and pterygoid bones. The quadrate was sampled in otic, middle, and ventral regions because this bone is oriented perpendicularly to the palatine and pterygoid bones. The regions were then subsampled randomly using a random number generator (built in Microsoft Excel) to assign fifty rows of data to be included in the quantitative analyses.

We expected neutral posture models to exhibit a base level of strain in the palatal elements. Postural Kinetic Competencies exhibiting strain in the palates higher than the neutral posture models represent less likely loading conditions. Conversely, models exhibiting strain in the palates lower than the neutral PKCs were considered acceptable, more likely anatomical configurations. Although the local effects of strain on bone tissue growth and resorption is complicated (e.g., Frost, 1987; Martin, 2000; Herring and Ochareon 2005), Curtis et al. (2011), using finite element analysis for bone strain, as we are here, hypothesized that cranial elements in *Sphenodon* and other vertebrates assumed shapes that were best adapted to their average loading environments as a means of optimizing strain across the entire skull. Thus, although higher and lower strains are not fundamentally “bad” or “good,” we can expect behaviors such as joint excursions that elicit exceptionally higher strains in elements to be less optimal than other behaviors. We define structural failure in our models as strains that exceed 6000 microstrain (με) because this value is contained within ranges of the estimated strain of bone failure (e.g., Reilly and Currey, 1999; Campbell et al., 2016).

Results

Muscle and Bite Forces in Extant Species

Comparisons of bite force in FEMs and known bite forces in living animals serves as an indication of the validity of the model. The bite forces of our models fall within the known (*Gekko*) and expected (*Psittacus*) ranges of the models. Modeled *Psittacus* bite force (61.78N [rostral bite position] – 96.44N [caudal bite position]) was greater than the 16.74N reported for Monk Parakeets (*Myiopsitta monachus*) estimated using PCSA by Carril et al. (2015) as expected given that the skull of *P. erithacus* is about twice as large. Bite forces in our *Gekko* models (11.27N [rostral bite position] - 18.53N [caudal bite position]) were near ranges reported by both Anderson et al. (2008; 10.1N - 19.1N) and Herrel et al. (2007; 10.78N - 16.97N) using bite force meters.

Sensitivity Analysis of Muscle Forces in *Tyrannosaurus*

The distribution of PCSA values of our sensitivity analysis of theoretical muscle architecture are represented using a heatmap (Fig. 3-4). Although pennation angle and fiber length are the two parameters on which PCSA depends, there is a functional relationship between pennation and fiber length in which fiber length has a stronger effect on PCSA than pennation angle. For example, when we hold fiber length constant (any horizontal line on Fig. 3-4), larger values of PCSA are associated with low pennation angle, and the largest value was 64 times the smallest value (approximately equal to $\cos^{-1}(89.1°)$). When we hold pennation angle constant (any vertical line on Fig. 3-4), larger

values of PCSA are associated with shorter fiber length, and the largest value was 100 times larger than the smallest value (equal to 0.01^{-1}). This and the construction of the PCSA equation, show that the effect of fiber length is greater than that of pennation angle on PCSA (*sensu* Gans and De Vree, 1987).

Upon this heatmap (Fig. 3-4), we project the regression line of Bates and Falkingham (2018), which compiled over 1000 measured vertebrate muscles, along with plots of Bates and Falkingham's (2012), Gignac and Erickson's (2017), and our phylogenetically-bracketed *Tyrannosaurus* muscle architecture data. Bates and Falkingham's (2012) muscle force estimates used combinations of pennation angles of 0-20° and fiber lengths of 0.1-0.4 times muscle length (i.e., 1/10 to 2/5 times muscle length), which resulted in forces below the regression line, thus corresponding to higher forces. Gignac and Erickson (2017) modeled muscles with 0° pennation and a fiber length equal to muscle length, the combination of which yields the lowest possible PCSA. The PCSA estimates in *Tyrannosaurus* from the present study fall close to the regression line of all known vertebrate PCSAs published by Bates and Falkingham (2018), suggesting that the values we used are close to predictions from extant taxa and our bite force estimates are reasonable.

Bite forces in our *Tyrannosaurus* model (35,365N - 63,492N) extensively overlap with the range reported by Bates and Falkingham (2012; 18,065N - 57,158N) and are about twice the magnitude predicted by Gignac and Erickson (2017; 8,526 - 34,522N). These differences between our results and those of

Gignac and Erickson (2017) are likely due to our inclusion of pennate jaw muscles; whereas the latter authors modeled all jaw muscles as parallel fibered.

Analyses of Strain Patterns

Strain differences were found among the *Gekko* models with respect to the bones, sampling region, and posture. The neutral *Gekko* model (Fig. 3-5A; Supp. Movies 1 - 6) exhibited higher strains in the pterygoid than those in the quadrate or the palatine. The ventral portion of the epipterygoid was extremely strained around the joint with the pterygoid, which may be an artifact of the modeling process wherein the epipterygoid and pterygoid were fused together. The body of the pterygoid, however, is strained across its length, representing a higher strain concentration than in any of the other elements of the palate (Fig. 3-5A). The FAM *Gekko* model reveals high strains in the quadrate, and pterygoid suggesting that this is not an optimal posture (Fig. 3-5B). However, the MLM *Gekko* model (Fig. 3-5C) exhibits low strains in the elements of the palate, suggesting that the MLM model is a more optimal posture, along with the neutral posture. The otic process retains slightly higher strains than the other portions of the quadrate in the MLM model. The pterygoid still possesses localized higher strains (Fig. 3-5C), though these are lower compared to the pterygoid in the FAM model (Fig. 3-5B).

The MLM model of *Gekko* (Fig. 3-6) possessed lower median strain values (1731 με) than those of neutral (2277 με) or FAM (2714 με) postures (Table 3). The lowest strain values of *Gekko* are found in the palatines. However,

strains were lowest in different portions of the palatine in each of the postural models of *Gekko*. The ventral portion of the quadrate was most strained in the FAM *Gekko* model (6322 με) and least strained in the neutral posture (1767 με). Median strain values of whole elements are shown for all taxa in Table 4. The otic and middle regions of the quadrate possessed identical strain profiles in all three postures, despite differences in rotation at the otic joint. Similarly, the pterygoid exhibited a conserved pattern of caudal to rostral strain decrease across all models. The caudal to rostral pattern is observed in the FAM posture in the palatines; however, this is reversed in the neutral posture. In the MLM posture, the rostral region of the palatine was subjected to more strain than the middle region but the caudal region was subjected to the highest strain.

The *Psittacus* models also experienced differing strains in the bones, sampling region, and between postures. In the neutral *Psittacus* model (Fig. 3-5D; Supp. Movies 7 - 12), the quadrate and pterygoid experienced high strain relative to other parts of the cranium (Fig. 3-5D). The palatine, postorbital process, and the interorbital septum experienced low strains in this posture despite serving as muscle attachment sites (Fig. 3-5D). The FAM *Psittacus* model revealed high strains on the rostral aspects of many of the kinetic palatal elements (Fig. 3-5E). In the MLM *Psittacus* model (Fig. 3-5F), strains are noticeably higher at the otic process of the quadrate, the postorbital process, and the middle of the palatine compared to the FAM model (Fig. 3-5D). Strain in the pterygoid is relatively uniform throughout the bone compared to that seen in the palatine.

In *Psittacus* (Fig. 3-7), the MLM model exhibited higher overall median strain of the palate (753 με) than neutral (619 με) or FAM (543 με) models (See Table 3). Strain values of the FAM model were the lowest, as expected by observations of feeding behaviors. The MLM model possessed higher overall strains in the palatine and pterygoid, maintaining the same trend as the other *Psittacus* postures. Pterygoid strains in the MLM model increased from the middle and caudal regions to the rostral region whereas in the neutral model strain steadily decreased moving rostrally. In the FAM model peak strains were found in the caudal region of the pterygoid, however, the middle region appeared to possess decreased strain. The strain again increased in the rostral sampling region. In all three postures strain decreased from caudal to rostral in the palatines. The otic process of the quadrate possessed the highest strain values across all postural models of *Psittacus*.

Strain differences found among the *Tyrannosaurus* model's bones, sampling regions, and between postures were highlighted by areas of structural failure. The neutral *Tyrannosaurus* model (Fig. 3-5; Supp. Movies 13 - 18) exhibited low strain throughout the palate with the exception of modeling artifacts at joints of the palate. The caudal portion of the pterygoid was weakly strained whereas the body of the quadrate experienced higher strains in the neutral posture (Fig. 3-5G). The palatine and pterygoid exhibited higher strains across their rostral bodies and the quadrate showed high strain values across pterygoid and otic processes (Fig. 3-5G). The joints of the FAM *Tyrannosaurus* model (Fig. 3-5H) were increasingly strained, particularly at isthmuses and articulations with

the cranium. Lower overall strain was found throughout the FAM model, but areas of failure remained prevalent across the palate (Fig. 3-5H). The palatine of the FAM model exhibited lower overall strain than the other elements in the palate (Fig. 3-5H). The MLM *Tyrannosaurus* model found the otic joint to be highly strained, and the bodies of the quadrate, pterygoid, and palatine bones to all be highly strained (Fig. 3-5I). High strains also propagated throughout the facial skeleton in the MLM model (Fig. 3-5I). Failures in the MLM model were observed throughout the pterygoid and the dorsal ridge of the quadrate body (Fig. 3-5I). Across the *Tyrannosaurus* models, the lower temporal bar experiences high strains near the quadratojugal-jugal suture that approach or exceed levels of structural failure (Fig. 3-5G – I).

Tyrannosaurus (Fig. 3-8) exhibited different quantitative strain profiles across the three postural models. The MLM model exhibited the highest median strain values (1768 με) of the three postural models (neutral 1542 με; FAM 1259 με; see Table 3). Across all three postures the quadrate was similarly strained overall, though the middle region was more variable (Fig. 3-8). The middle region of interest was subjected to more strain than the ventral or otic regions in all postures, but especially in the MLM posture (Fig. 3-8). The neutral posture exhibited similar ventral and otic strains (1540 με and 1459 με, respectively); however, the otic strains were noticeably higher in both the MLM and FAM models (1980 με and 2029 με respectively). The pterygoid in the MLM posture of *Tyrannosaurus* was subjected to greater strain than either the neutral or FAM postures. The rostral region of the pterygoid was subjected to the least strain by

large margins in both the neutral and MLM models. The most appreciable difference between models, however, can be seen within the caudal portions of the three models (Fig. 3-8). A slight increase was observed from middle to rostral in the FAM model. In all three postures, the palatine exhibited the highest median strains in the rostral portion with similar strain patterns in the caudal and middle aspects as well. The caudal portion of the palatine was subjected to low median and overall strains in all three models, but this is especially so in the FAM model (Fig. 3-8).

Discussion

Tyrannosaurus was functionally akinetic

By incorporating cranial joint articular tissues, distributed muscle loads, and posture analysis to infer cranial performance in *Tyrannosaurus rex*, we have gained a nuanced understanding of the biomechanics of the skull. We accurately estimated the biomechanical environment of *Gekko* and *Psittacus* using PKC modeling methods and achieved lifelike results prior to modeling *T. rex* (Herrel 1999; 2000; Carril et al. 2015). Rotation of the quadrate 5º rostrocaudally and mediolaterally was sufficient to affect the rostral elements of the palate and the facial skeleton such that lifelike fore-aft and mediolateral motions were reflected in the models of both extant taxa. Functionally acceptable ranges of strain were observed in models of FAM in *Psittacus* and MLM in *Gekko*. Equally important, MLM in *Psittacus* and FAM in *Gekko* resulted in failures at joints, within individual bones, and across the palate. Thus, the loading behavior of the *Tyrannosaurus*

model also performs with acceptable accuracy with respect to the anatomical potential of the animal. Using these findings, we conclude that *Tyrannosaurus* was functionally akinetic. Although hypotheses of fore-aft palatal motion in *Tyrannosaurus* are more supported compared to those of mediolateral palatal motion, the linkages surrounding the otic joint impede fore-aft excursions of the quadrate, and the loading that the palate and craniofacial skeleton experience during bites suggests powered, fore-aft kinesis is extremely unlikely. Like paleognaths (Gussekloo, 2005), many iguanians and other lepidosaurs (Jones et al. 2017), many dinosaurs (Holliday and Witmer, 2008), stem crocodylomorphs (Pol et al., 2013), and numerous diapsid species, including *Tyrannosaurus,* remain akinetic despite possessing unsutured otic and palatobasal joints.

Cranial kinesis in *Tyrannosaurus* has been debated since shortly after the initial description of the taxon. Osborn (1912) recognized the morphological limitations of kinesis in *Tyrannosaurus*, initially describing the otic joint as immobilized by the pterygoid, quadratojugal, and squamosal via sutures between the quadrate and surrounding bones. Osborn's description of the otic joint was refuted by Molnar (1991) who recognized that, although the otic joint was surrounded by sutured elements, the joint itself was smooth and saddle shaped which in turn led to subsequent functional analyses of otic joint kinesis by Molnar (1991, 1998), Rayfield (2005), and Larsson (2008). Larsson (2008) supported inferences of propalinal (fore-aft) movement of the *Tyrannosaurus* palate, stating that movement was possible due to osteological anatomy, kinetically competent joints throughout the palate, and streptostylic movement of the quadrate. Molnar

(1991, 1998) described streptostylic movement as well, stating that the otic joint could allow for “swings in several directions” (1991, pg. 163) and was capable of resisting forces in multiple directions. Although streptostyly and propalinal palatal movement, as a result, appear reasonable in a disarticulated specimen, the rigidity of the facial skeleton, congruency of the otic joint, and the similarities between the neutral and FAM models suggest that any movement of the palate was incidental and potentially injurious to *Tyrannosaurus*. Moreover, the craniofacial skeleton of adult tyrannosaurs has numerous bony features that defy translational movements of the palate including the following: rigid, unbendable bones, a secondary palate built by massive, co-sutured maxillae, and heavily interdigitated sutural and scarf joints like the frontonasal, circummaxillary, and temporal joints (Carr, 1999; Snively et al., 2006). These lines of evidence all suggest *Tyrannosaurus* was functionally akinetic, despite possessing unsutured otic and palatobasal joints (Figs. 3-9 and 3-10).

Challenges to Modeling Kinesis and Cranial Function

Despite advances over previous modeling approaches, our process has several important sources of error and uncertainty, including tissue material properties, joint posture and range of motion, and jaw muscle activation patterns. We also acknowledge that taphonomic issues and reconstruction of fossils lead to potential sources of error in modeling extinct taxa as described by Hedrick et al. (2019). Material properties of non-osseous tissues are not well described outside of mammals and are unknown for large, extinct theropod dinosaurs.

Wang et al. (2012; testing of various material properties), Lautenschlager (2013; testing of beaks, teeth, and bone), and Cuff et al. (2015; validation study) all explored the impact of various material properties in mammal, dinosaur, and bird finite element models. We used these studies to inform our assignments of skeletal and articular properties to models, bearing in mind that Strait et al. (2005) noted that elastic properties have small impacts on model performance. We therefore constructed our joints with separate materials for the large cranium of *Tyrannosaurus* (canine patellar tendon) and the smaller crania of *Psittacus* and *Gekko* (rat cranial suture). Although sutural areas and joints were modeled in other studies (e.g., Porro et al., 2011; Moazen et al., 2009; Jones et al., 2011, 2017) as FEM elements assigned the properties of sutural or joint materials, this method retains a tightly packed area of the model which would instead be occupied by more flexible material allowing for more deformation in sutures and joints involved in cranial kinesis; cranial sutures not associated with kinesis are less flexible. We consider our method of creating open spaces within the joint capsules of the model and joining these portions using flexible beams to more accurately simulate malleable soft tissue by permitting more realistic deformation at joints; however, further studies are needed to validate these findings. Node anomalies at joint articulations are a result of this joint construction, but do not change the overall strain patterns of the model with fused joints.

Static postures in our models are merely moments in a coordinated series of motions during feeding bouts. Although we only tested 3 specific instances of what could be a dynamically changing joint articulation, recent studies of ball and

socket joints suggest that despite their seemingly flexible ranges of motion, they do not necessarily perform this way (e.g. Manafzadeh and Padian 2018). Moazen et al. (2008) suggested that the temporal ligaments in *Uromastyx* stabilized the quadrate during feeding. Analogously, Manafzadeh and Padian (2018) found that only 10% of possible postures were valid once capsular ligaments were included in the ball and socket shaped articulation. Indeed, *Tyrannosaurus* quadrates possess enlarged tuberosities on the medial portion of the otic process that bear the features of attachments for large capsular ligaments and complementary ligamentous scars adorn the lateral portion of the otic joint. Likewise, the palatobasal joint is highly congruent with a labrum of pterygoid bone nearly encompassing the basipterygoid condyle, further suggesting pronounced capsular ligaments. Thus, bony joint morphology (Holliday and Witmer 2008), loading, and postural analysis suggest that a miniscule, and likely biologically-insignificant, envelope of motion was available for the 6-bar linkage system of the robustly-built *Tyrannosaurus* palate, which spans pairs of highly congruent palatobasal, otic, and craniofacial joints compared to the relatively freely moving bird hip joints. Finally, despite slight vagaries in the articulation of our model and that of the original BHI 3033 mount (e.g., palatobasal articulations, epipterygoid-pterygoid joint), these morphologies still likely fall within the possible natural variation of the *Tyrannosaurus rex* population making our results biologically realistic and similar to other studies of posture and range of motion (e.g., Gatesy et al. 2010; Mallison 2010; Claes et al. 2017; Olsen et al. 2017).

We modeled jaw muscles as contracting synchronously at maximal force even though it was likely that, as has been shown in other diapsids, there is variation in the firing sequence and magnitude of cranial musculature (Busbey, 1989; Nuijens et al., 1997; Herrel et al., 1999; van der Meij and Bout, 2008; Vinyard et al., 2008, Perry and Prufrock, 2018). Protractor and adductor muscles show variation in activation pattern during the feeding cycle, and the loads these muscles impart appear to help stabilize the cranial joints (Cundall, 1983; Herrel et al., 1999; Holliday and Witmer, 2008). Moreover, the orientation and osteological correlates of the m. protractor pterygoideus indicate that it was highly tendinous, likely pennate, and oriented dorsoventrally and mediolaterally (Holliday, 2009). This architecture suggests m. protractor pterygoideus had very limited excursion, and, at best, held the palate against the braincase, restraining its movements and filling a largely postural role.

Finally, to further understand the role of muscle loads and constraints on the model, we conducted post hoc tests with neutral *Tyrannosaurus* models using occipital constraints as well as differential activation of the protractor muscles. Constraints on the occipital surface of the skull were modeled to mimic cervical muscle loads imparted during inertial feeding mechanisms (Snively and Russell 2007; Snively et al., 2014) as well as to free the jaw joint from artificial constraints. Additionally, protractor muscles were toggled on and off in the neutral *T. rex* model to test for their effect on palatal strains. Protractor muscles were found to not alter the distribution and range of strains in the palate suggesting they may not be functionally important, and even may be potentially

vestigial. Conversely, occipital constraints shifted and diminished the strains experienced by the quadrate and pterygoid, but increased strains experienced by the epipterygoid as it was cantilevered by its laterosphenoid attachment. Regardless, the low strains experienced by the braincase in the neutral and FAM models in all tests indicate that although the palate was incapable of movement, it was capable of dissipating high strains away from the braincase, thus insulating the neurosensory capsules of the head (Holliday and Witmer, 2008).

Conclusion

This study presents a unique method of exploring *Tyrannosaurus* cranial kinesis that incorporates anatomically-distinct, distributed muscle loadings, reconstructions of joint tissues, varying postures of cranial elements, and ultimately analysis of cranial performance using finite element modeling. Its new approaches differ from previous inferences of muscle architecture (Gignac and Erickson, 2017), joint function (Molnar, 1991; Rayfield, 2004, 2005a, b,) and joint kinematics (Larsson 2008). The findings presented here offer a nuanced, integrative approach to testing biomechanical hypotheses of cranial function in extant as well as extinct vertebrate species. Not only are these methods applicable to testing *a priori* assumptions about kinematics and function in living animals, but they also offer a detailed approach to testing behavioral and functional hypotheses in animals that are impossible to explore using *in vivo* approaches. Few modeling studies incorporate multiple lines of evidence, such as multiple postures, joint tissues, and distributed muscle loadings in such

diverse species, and here we illustrate how powerful these inferential approaches can be using *Tyrannosaurus* as a case study. These approaches found inferences of gross cranial mobility in *Tyrannosaurus* to be unsupported and that *Tyrannosaurus* was functionally akinetic.

Table 3-1. Temporal bars, pterygoid shape, joint type, segmented skeletal elements, constructed joints, and mobile elements represented in each taxon in this study. Mobile elements are defined as elements of the palate that are capable of moving as a result of being joined to the cranium by joint and sutural materials only in the finite element model. These entities are consistent across postures within each taxon.

Taxon	Temporal Bars	Pterygoid Shape	Joint Type or Shape	Elements Segmented	Joints Modeled	Mobile Elements in Final Model
Gekko	None	Strut-like	Otic: Synchondroidal Palatobasal: Diarthrodial	Palatine, Pterygoid, Rostrum, Quadrate, Mandible, Neuro/dermatocranium	Palatobasal, Otic, Frontoparietal Hinge	Rostrum, Palatine, Pterygoid, Epipterygoid, Quadrate
Tyrannosaurus	Upper and Lower	Mediolaterally thin	Otic: Ball and Socket Palatobasal: Ball and Socket	Palatine, Pterygoid, Rostrum, Epipterygoid, Ectopterygoid, Vomer, Quadrate, Mandible, Neuro/dermatocranium	Palatobasal, Otic	Pterygoid, Epipterygoid, Ectopterygoid, Quadrate
Psittacus	Lower	Strut-like	Otic: Diarthroidal Palatobasal: Diarthroidal	Palatine, Pterygoid, Jugal, Rostrum, Quadrate, Mandible, Neuro/dermatocranium	Palatobasal, Otic, Craniofacial Hinge	Rostrum, Palatine, Pterygoid, Quadrate, Jugal

Table 3-2. Muscle parameters used to estimate physiological cross sectional areas and jaw muscle force used in finite element models.

		mAMES	mAMEM	mAMEP	mAMP	mPSTs	mPSTp	mPTd	mPTv	mPPT	mEM	mPM	mLPT	mDM
Fiber Length (cm)	*Gekko*	1.3		1.1	0.8	1.3	0.8	0.8	0.8	0.4			0.8	1
	T. rex	46	52	57	28	55	41	32	28	10			6	25
	Psittacus	1.6		1.5	0.3	1.4		1.2	1.0	1.0	1.6	2.1		0.7
Pennation Angle (θ)	*Gekko*	20		0	5	0	0	15	15	5			5	5
	T. rex	0	0	0	15	10	10	10	15	15			0	5
	Psittacus	20		20	0	6.66		14.54	4.09	0	2.57	0		5.52
Muscle Volume (cm^3)	*Gekko*	0.445		0.180	0.463	0.141	0.128	0.093	0.391	0.072			0.028	0.066
	T. rex	20971	17729	11914	37120	7792	2668	40106	8562	2187			545	8981
	Psittacus	1.07		0.070	0.006	0.026		2.63	1.54	0.036	0.098	1.24		0.084
Force (N)	*Gekko*	9.25		4.58	16.84	3.11	4.28	3.44	13.77	4.49			1.12	1.96
	T. rex	13343	9841	6635	39859	4209	1865	34816	8820	5489			3180	10206
	Psittacus	21.17		13.41	6.90	6.20		63.11	47.38	11.38	19.99	17.59		35.37

Table 3-3. Median strain of entire palate by model. Quadrate, pterygoid, and palatine regions of interest are taken into account in these medians.

Taxon	Posture	Median Strain
Gekko gecko	Neutral	2277.36
	MLM	1731.44
	FAM	2714.28
Tyrannosaurus rex	Neutral	1542.46
	MLM	1768.37
	FAM	1259.19
Psittacus erithacus	Neutral	619.13
	MLM	753.24
	FAM	543.55

Table 3-4. Median strain of palate elements organized by posture for each taxon. Multiple regions of interest are taken into account in determining the median values of each bone (quadrate, pterygoid, and palatine).

Taxon	Bone	Posture	Median Strain
Gekko gecko	Palatine	Neutral	1346.01
	Pterygoid	Neutral	2822.19
	Quadrate	Neutral	2516.53
	Palatine	MLM	620.17
	Pterygoid	MLM	1731.44
	Quadrate	MLM	4094.59
	Palatine	FAM	2300.19
	Pterygoid	FAM	2759.20
	Quadrate	FAM	4341.22
Tyrannosaurus rex	Palatine	Neutral	995.86
	Pterygoid	Neutral	1993.55
	Quadrate	Neutral	1540.88
	Palatine	MLM	1024.31
	Pterygoid	MLM	2348.10
	Quadrate	MLM	1980.55
	Palatine	FAM	534.07
	Pterygoid	FAM	1259.19
	Quadrate	FAM	2029.88
Psittacus erithacus	Palatine	Neutral	326.41
	Pterygoid	Neutral	1121.62
	Quadrate	Neutral	412.29
	Palatine	MLM	753.24
	Pterygoid	MLM	884.82
	Quadrate	MLM	258.73
	Palatine	FAM	455.94
	Pterygoid	FAM	587.26
	Quadrate	FAM	210.53

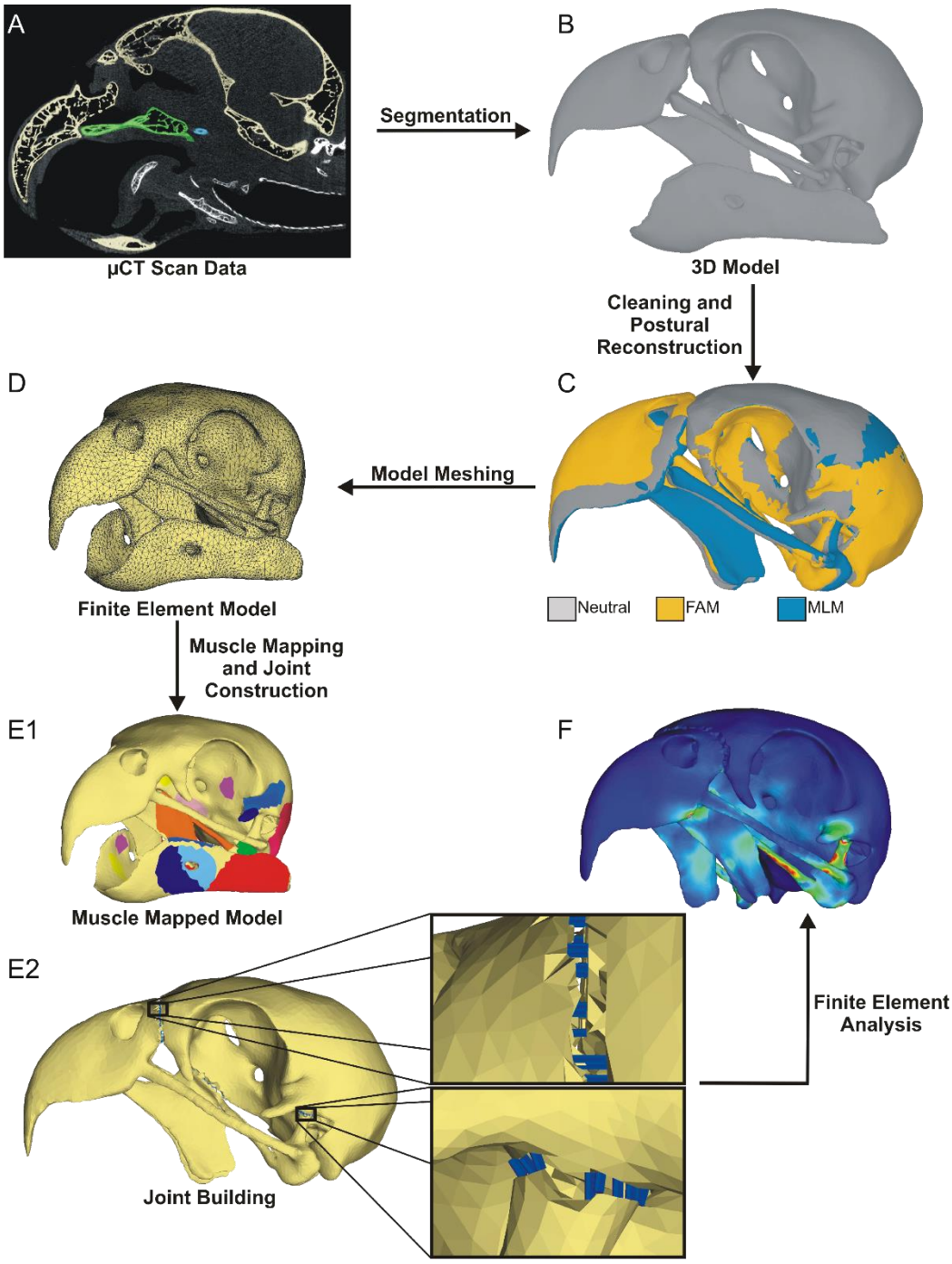

Figure 3-1. Postural Kinetic Competency modeling workflow followed in this study. **(A)** Microcomputed Tomography data is segmented to build 3D models by segmenting individual bones (or bony segments; e.g., beak, braincase) as separate elements **(B). (C)** 3D models are reconstructed in kinetic postures with individual elements realistically articulated. **(D)** The resulting models are imported into Strand7 as stereolithographical files and are meshed using 4-node tetrahedra. **(E1)** Meshed models are prepared for finite element analysis (FEA) by mapping muscles on the surface and eliminating tetrahedra in joint areas. **(E2)** Beams are attached to the facing sides of joint surfaces and are given material properties reflecting capsular or sutural ligaments. **(F)** The resulting finite element model is loaded using distributed muscle forces via the BoneLoad MATLAB program and Strand7 FEA software.

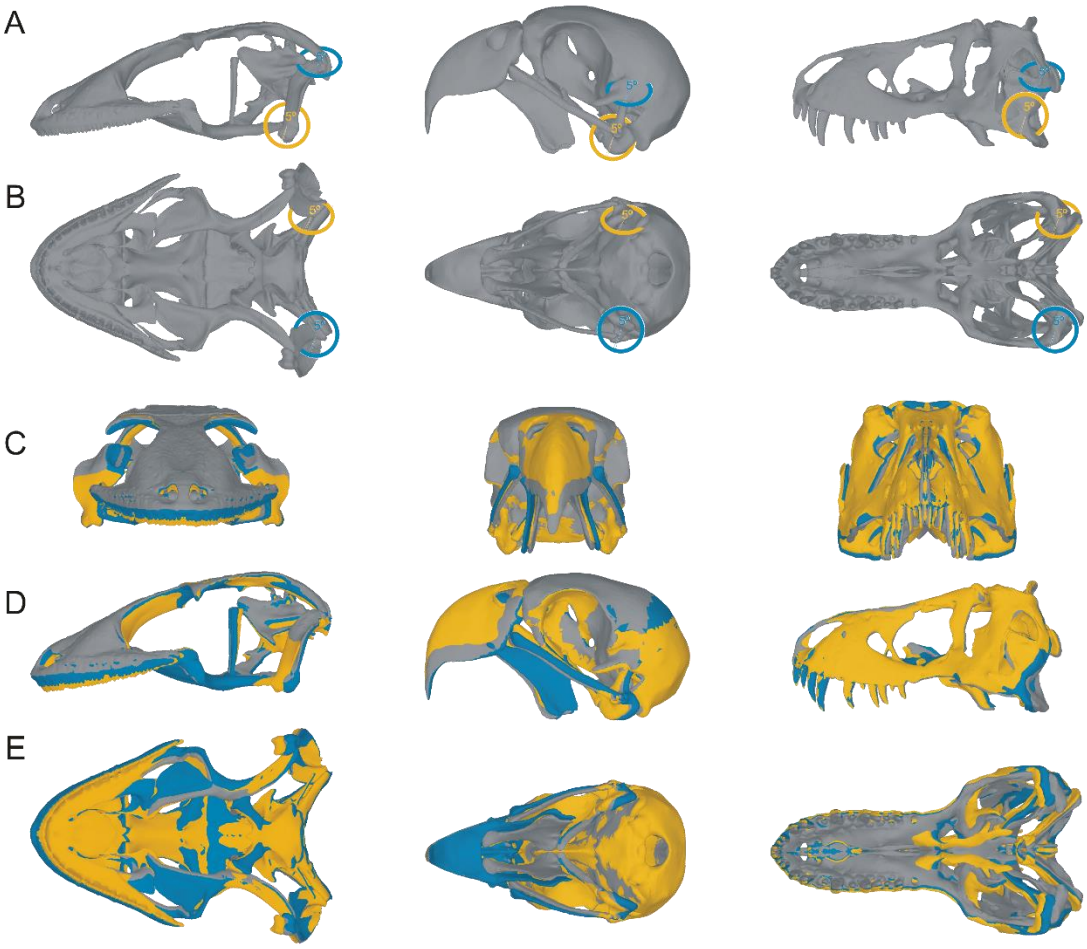

Figure 3-2. Comparisons of postures using overlays of each of the three models: **Left**, *Gekko gecko*; **Middle,** *Tyrannosaurus rex*; **Right,** *Psittacus erithacus* showing postural change in left lateral **(A)** and ventral **(B)** views and in rostral **(C)**, lateral, **(D)**, and ventral **(E)** views showing overlaid postural configurations used to model kinetic competency. Postures are overlaid using the jaw joint as the origin of the axes. Neutral models are represented in grey, FAM models in orange, and MLM models in blue. Angles of rotation/translation at the otic joint are shown using color-coded angle measurements in **(A)** and **(B)**.

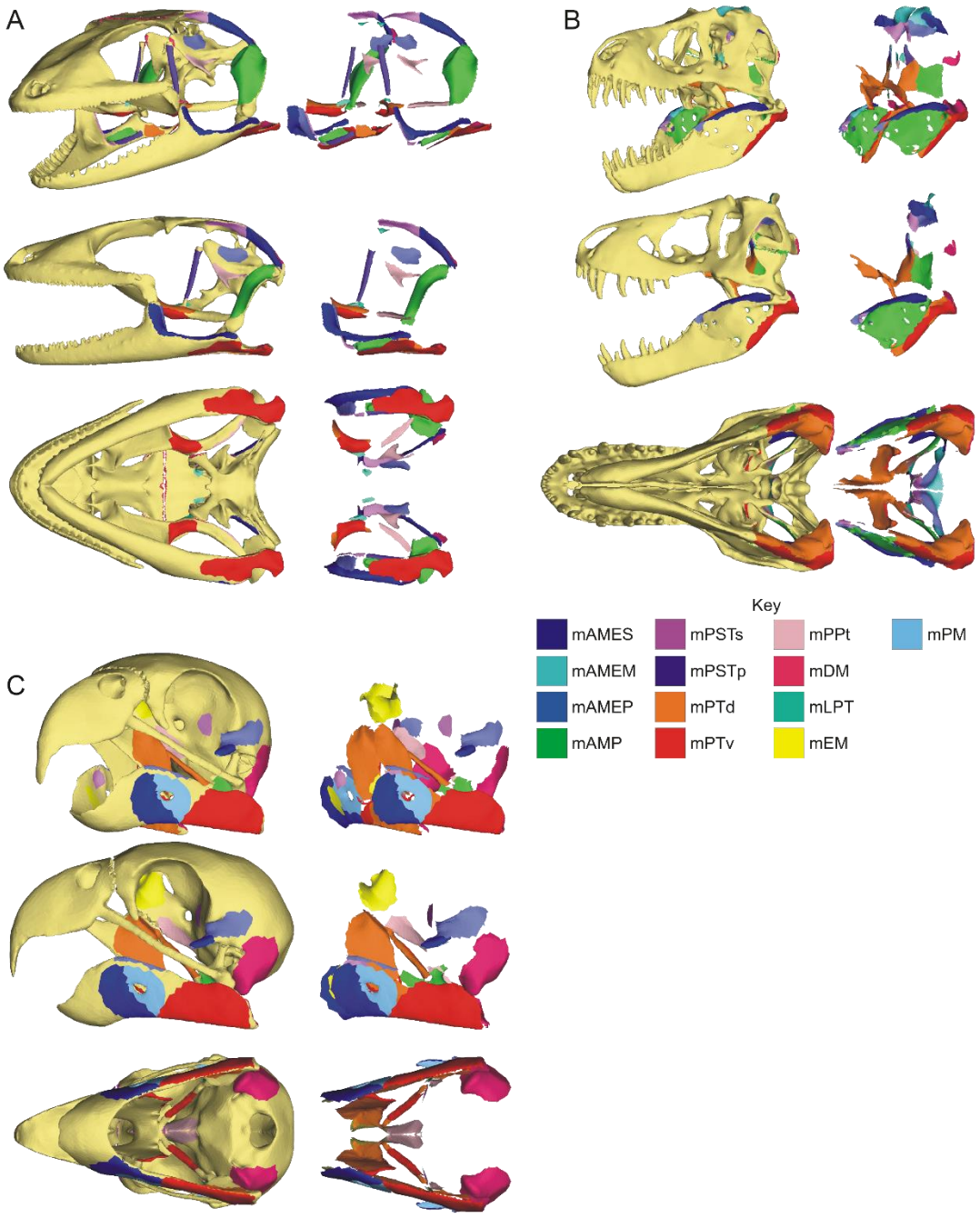

Figure 3-3. Mapped attachments of jaw muscles used to load finite element models of **(A)** *Gekko gecko*; **(B)** *Psittacus erithacus,* and **(C)** *Tyrannosaurus rex* in **Top:** left oblique; **Middle**: left lateral; and **Bottom**: ventral views for each taxon. Muscle map colors follow same palate and hypotheses of homology as Holliday (2009).

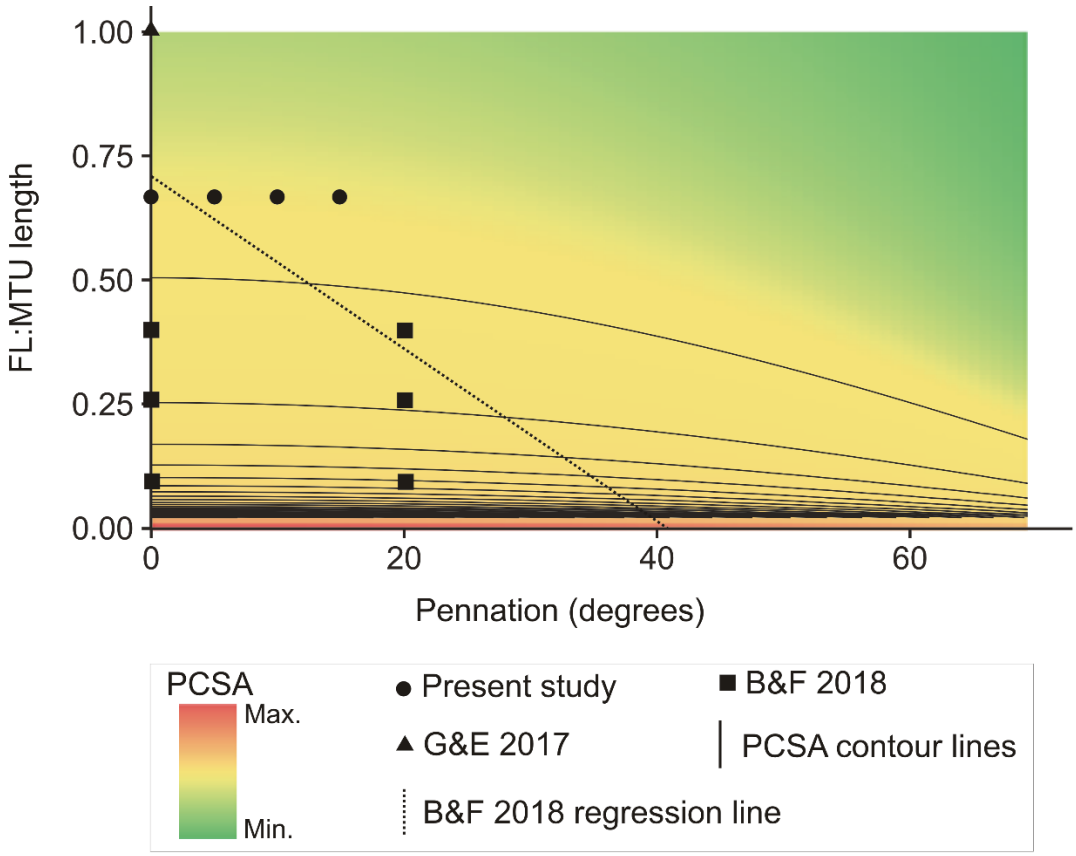

Figure 3-4. The relationship between fiber length, pennation angle, and force in muscle physiology and its application to reconstructing function in fossil taxa using recent case studies. PCSA is a function of pennation angle and fiber length and is mapped as a heatmap with contour lines. We replotted the regression line from Bates and Falkingham 2018 (labeled "B&F 2018") showing the classic prediction that increasing pennation in order to accommodate shorter muscle fibers increases PCSA. PCSA values from recent studies, Gignac and Erickson 2017 (labeled "G&E 2017") and Bates and Falkingham 2018, of *Tyrannosaurus* cranial biomechanics are also plotted to show similarities in approaches.

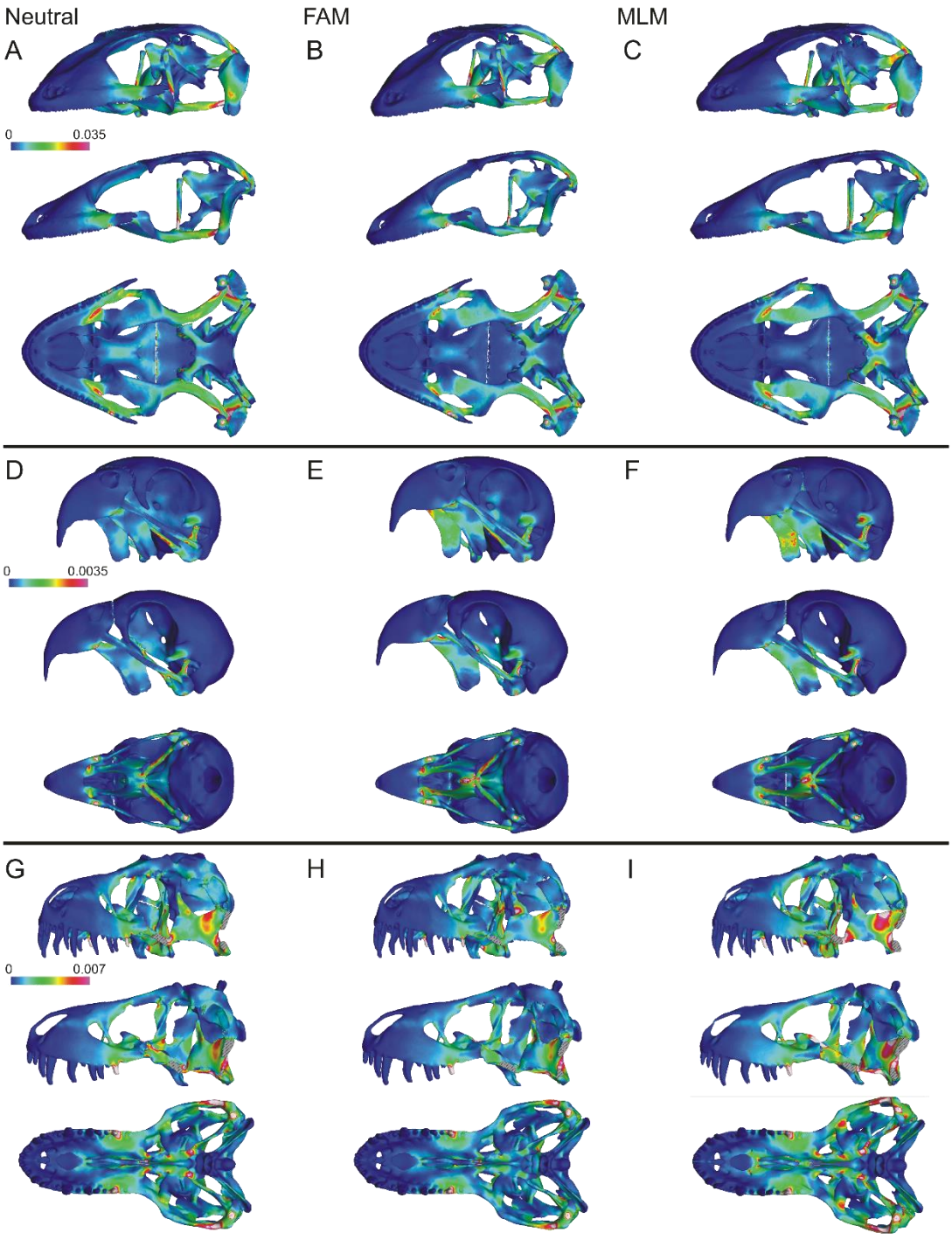

Figure 3-5. Heat maps depicting Von Mises strains in *Gekko gecko* **(A - C)**, *Psittacus erithacus* **(D - F)**, and *Tyrannosaurus rex* **(G - I)** in **Left**, Neutral; **Middle,** FAM; and **Right**, MLM postures of each taxon. Models are shown in left oblique **(top)** left lateral **(middle)**, and ventral **(bottom)** views. Heat maps show strains in postural models with all muscles fired simultaneously. Areas of high strain appear in warmer colors; white areas are beyond the scales presented with the models. Cooler colors depict areas of low strain concentration. Bones of the left lateral dermatocranium (i.e., portions of the maxilla, jugal, lacrimal, postorbital, quadratojugal bones) have been removed on heat maps of *T. rex* to show details of the palate, although all bones were in place for the analysis.

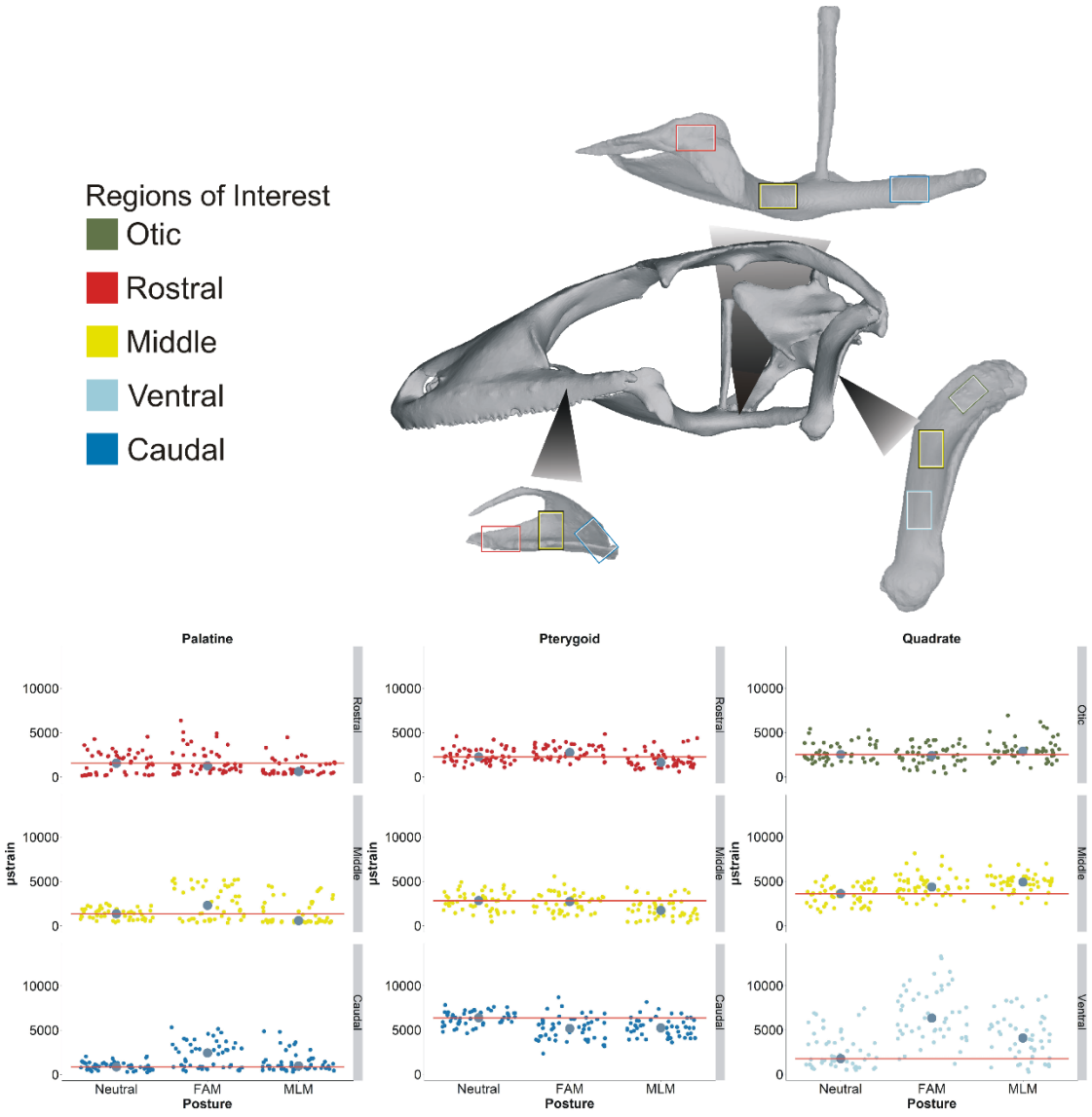

Figure 3-6. Strains of regions of interest in the palatal elements of *Gekko gecko*. Regions of interest and scatter plots showing individual sample points as well as median strains (color-coded by sampling region) are represented. Otic, Middle, and Ventral regions correspond to sampling of the quadrate whereas Rostral, Middle, and Caudal regions correspond to sampling areas of the palatine and pterygoid. Each sampling region consists of 50 tetrahedra sampled randomly from the surface of the skeletal element. Horizontal lines representing the median value of the neutral posture are shown in red in each region of the palatal bones to facilitate comparison across postures.

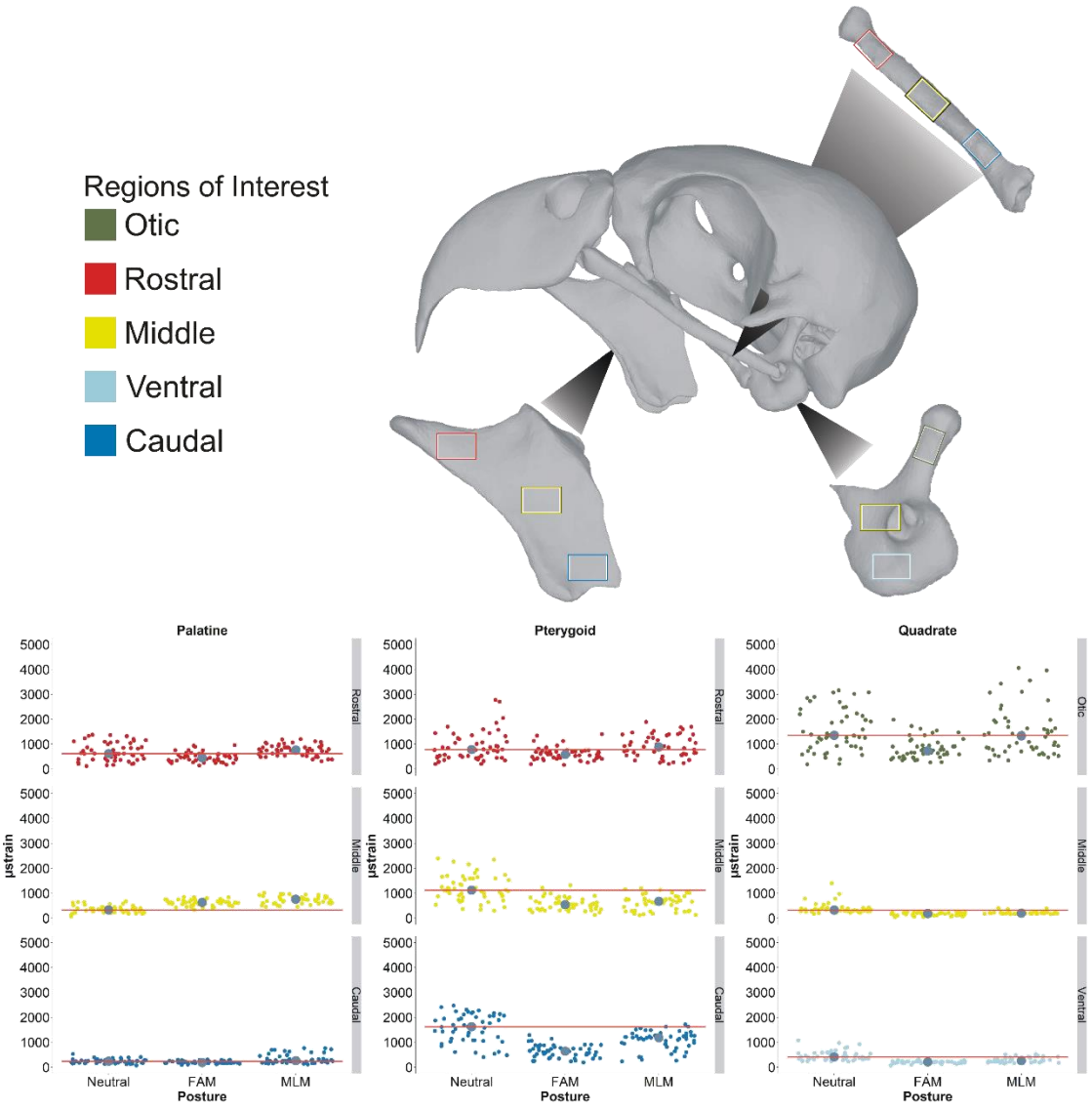

Figure 3-7. Strains of regions of interest in the palatal elements of *Psittacus erithacus*. Regions of interest and scatter plots showing individual sample points as well as median strains (color-coded by sampling region) are represented. Otic, Middle, and Ventral regions correspond to sampling of the quadrate whereas Rostral, Middle, and Caudal regions correspond to sampling areas of the palatine and pterygoid. Each sampling region consists of 50 tetrahedra sampled randomly from the surface of the skeletal element. Horizontal lines representing the median value of the neutral posture are shown in red in each region of the palatal bones to facilitate comparison across postures.

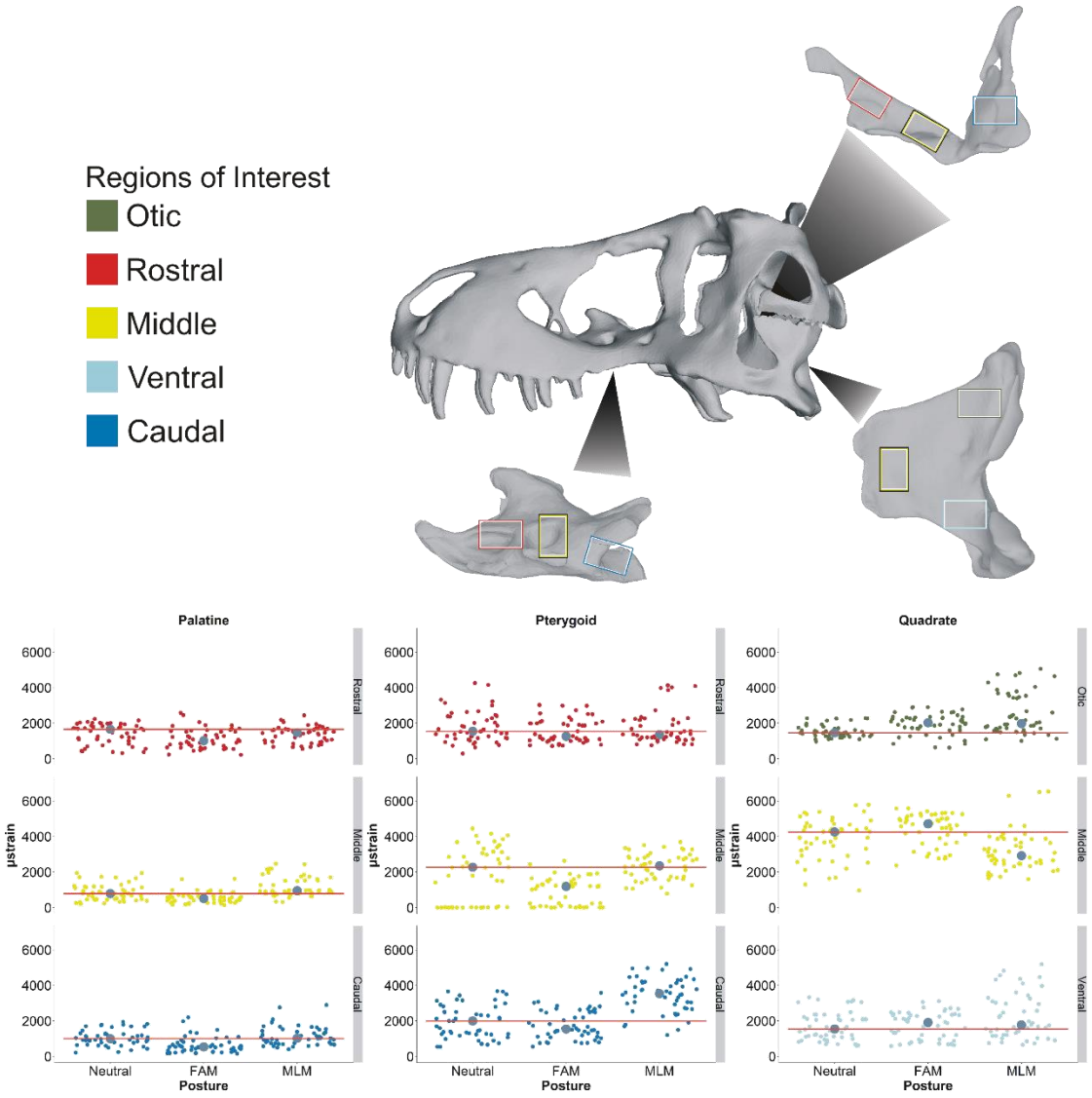

Figure 3-8. Strains of regions of interest in the palatal elements of *Tyrannosaurus rex*. Regions of interest and scatter plots showing individual sample points as well as median strains (color-coded by sampling region) are represented. Otic, Middle, and Ventral regions correspond to sampling of the quadrate whereas Rostral, Middle, and Caudal regions correspond to sampling areas of the palatine and pterygoid. Each sampling region consists of 50 tetrahedra sampled randomly from the surface of the skeletal element. Horizontal lines representing the median value of the neutral posture are shown in red in each region of the palatal bones to facilitate comparison across postures.

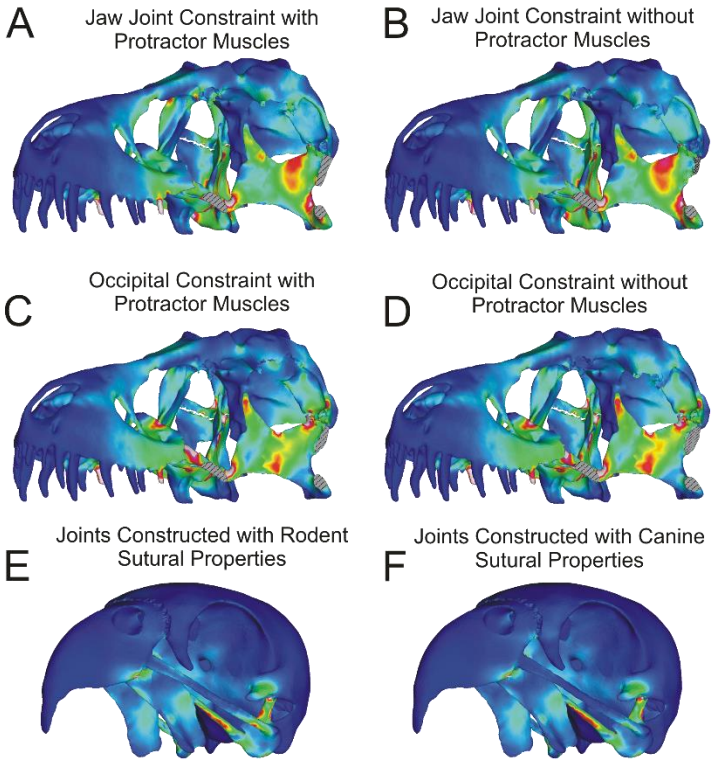

Figure 3-9. Comparison of neutral postures of *Tyrannosaurus rex* and *Psittacus erithacus* in left rostrolateral view showing effects of protractor muscle activation, constraints, and sutural materials on the behavior of models. Jaw joint constraints with activated **(A)** and deactivated **(B)** protractor muscles reveal few differences in strains in the model. Occipital constraints with activated **(C)** and deactivated **(D)** protractor muscles reveal significant differences in strain distribution in the palate. Regions of models with hatching represent areas that have been cut away to allow for better visualizations of internal structures. *Psittacus erithacus* is presented to show differences between using rodent sutural properties **(E)** and canine sutural properties **(F)**. Rodent sutural properties were used in *Psittacus* and *Gekko* and canine sutural properties were used in *Tyrannosaurus*. Sutural properties were considered based on taxon size.

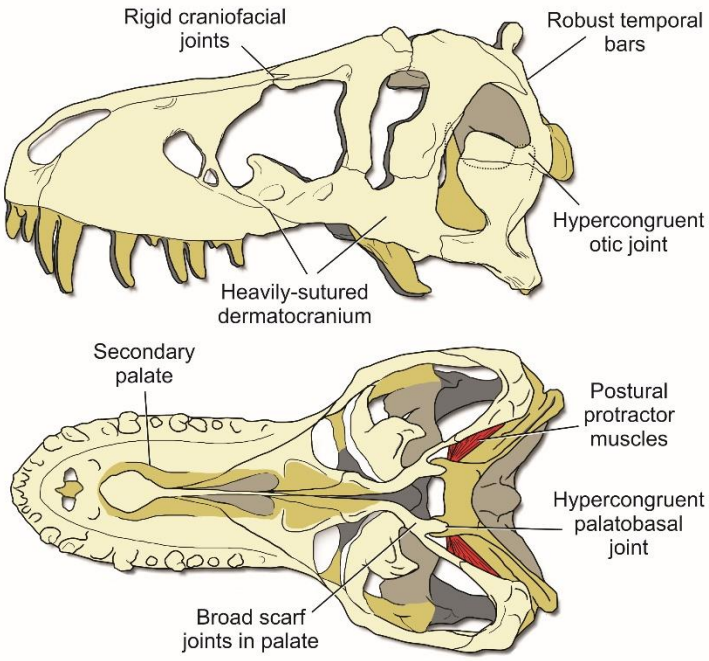

Figure 3-10. Illustration of *Tyrannosaurus* skull in left lateral **(top)** and ventral **(bottom)** views with key functional characteristics of the feeding apparatus. Numerous features of the skull of *Tyrannosaurus* suggest it was not capable of substantial cranial kinesis.

Chapter 4

Analysis of the Biomechanical Environment of the Feeding Apparatus of Parrots Using Finite Element Models, Statistics, and Bone Mechanics

Introduction

All organisms acquire energy using feeding behaviors appropriate for, and constrained by, their functional morphology (Schwenk 2000; Ross and Iriarte-Diaz 2014). Muscular and skeletal systems work in concert to form a feeding apparatus capable of processing food items efficiently; enabling diverse organisms to exploit specific ecological niches. The morphological characteristics of the feeding apparatus can be used to define groups of organisms and to track evolutionary changes across groups. Morphological diversity within groups presents a number of problems to tracking evolutionary changes. The most successful extant tetrapod group, with over 10,000 recognized species residing in every major biome on every continent and waterway, birds (Class Aves), exhibit many different feeding behaviors across multiple feeding system morphologies (Prum et al. 2015; Navalon et al. 2018).

Avian feeding mechanisms include specialized skimming, probing, tearing, manipulating, and prying beaks of various shapes and sizes. Despite this variability, and regardless of diet, closely related groups of birds tend to possess similarly-shaped beaks and palates (Fig. 4-1; Bright et al. 2016; Felice et al. 2018; Navalon et al. 2018). How structurally similar beaks and palates are capable of performing diverse feeding behaviors is understudied given the

ecological diversity of birds (Herrel et al. 2005a; 2005b; Schweizer et al. 2014). Parrots (Order: Psittaciformes) are one major group of birds that engages in multiple diverse diets and feeding behaviors despite largely similar beaks across most members of the family (Hackett et al. 2008; Suh et al. 2011; Jarvis et al. 2014).

Extant parrots occupy coastal, forest, and montane environments across the Southern Hemisphere and engage in varied diets known to include nuts and seeds (*Melopsittacus undulatus, Psittacus sp.*), leaves (*Strigops habroptila*), fruits (*Psittrichas fulgidus*), flowers and nectar (*Trichoglossus sp.*, *Loriculus sp.*), mammals and birds (*Nestor sp.*), and invertebrates (Richardson and Wooller 1990; Francisco et al. 2002; Miller and Fowler 2014; Schweizer et al. 2014; Toft and Wright 2015; Froggatt and Gill 2016). The most common dietary preference of parrots is granivory or seed-eating. Morphologically distinct parrot species such as the Grey Parrot (*Psittacus erithacus*; Africa), Scarlet Macaw (*Ara macao*; South America), Palm Cockatoo (*Probosciger aterrimus*; Indonesia to Australia), and Ringneck Parakeet (*Psittacula krameri*; Indian subcontinent) occupy similar ecological niches of granivory, attesting to the commonality of this diet globally within parrots. Exploring the underlying mechanisms of how parrots are capable of engaging in disparate dietary ecologies requires biomechanical testing and analysis.

The parrot feeding apparatus exhibits many musculoskeletal adaptations used in a vast range of activities including feeding, climbing,

and object manipulation behaviors (Homberger 1980; Livezey 1992; Tokita et al. 2007; Homberger 2003; Auersperg et al. 2011; Carril et al. 2015). The heads of parrots are capable of such a wide range of activities in part because they employ extensive cranial kinesis (Homberger 2003; Toft and Wright 2015). The movement of parrot heads is observable between the cranium and the rostrum at the highly mobile craniofacial hinge (Tokita et al. 2007; Carril et al. 2015; Toft and Wright 2015). Exploring the underlying mechanisms of how parrots are capable of engaging in disparate dietary ecologies through biomechanical testing and analysis enables us to track evolutionary changes across avian lineages by observing differences in the feeding apparatus.

Biomechanical studies have been conducted in numerous taxa to explore the role of cranial musculoskeletal systems on feeding behaviors (Dumont and Herrel 2003; Herrel and O'Reilly 2006; Habegger et al. 2010; Dumont et al. 2014). Material properties testing, fluid mechanics analysis, finite element analysis (FEA), kinematics, and X-ray Reconstruction of Moving Morphology (XROMM) have been used to explore feeding behaviors in animals such as bats (Aguirre et al. 2003; Dumont et al. 2005), fishes (Holzman et al. 2008; Ferrara et al. 2011; Gidmark et al. 2014; Camp et al 2015), and lizards (Throckmorton 1976; Herrel et al. 1996; Lee et al. 1999). Among avians specifically, biomechanical studies of feeding systems have included paleognathes (Attard et al. 2016), parrots (Homberger 2003), sparrows (Hoese and Westneat 1996), and finches (Nuijens et al. 2000; Van der Meij et al. 2004; Herrel et al. 2005; Van der Meij et al. 2006; Herrel et al. 2010), as well as general discussions of avian

cranial kinesis (Bock 1966; Meekangvan et al. 2006). However, studies of the avian feeding apparatus using FEA are not yet prevalent in the literature, though examples do exist (Degrange et al. 2010; Herrel et al. 2010; Soons et al. 2010). Finite element analysis is required to fully understand the gentle nuances of skeletal form and function change between morphologically comparable organisms. Whereas shape analyses are useful tools for evaluating functional morphology, FEA is capable of further analyzing working system as well. Further biomechanical study of wide ranging and diverse, yet morphologically similar taxa, such as parrots, is integral to understanding evolutionary trends in the avian lineage.

Morphological evaluation of the kinetic linkage system and phylogenetic relationships of parrots is virtually unexplored with few exceptions of discussions of the basic principles of cranial kinesis (Bock 1999; Tokita 2003; Tokita et al. 2007) and descriptions of the biomechanical environment of the cranium (Homberger 1980; Carril et al. 2015). Based on currently available data and known morphological and ecological characteristics of parrots, we generated two predictions about the biomechanical environment of parrots and characters of parrots in the context of current phylogeny: 1) that parrots with similar diets, body sizes, and muscular force generating capabilities will exhibit similar character evolution across a phylogenetic tree, and 2) that measures of pterygoid shape and relative muscle force acting on the pterygoid will generate

comparable bending resistance properties in the pterygoids of different parrots.

Because of their diverse diets and morphologically similar and highly-derived cranial morphology, parrots provide an ideal case for studying the biomechanics of the feeding apparatus and tracking its evolution through a lineage of related organisms. Hofer (1950), Homberger (1980, 2003), Carril et al. (2015), and Froggatt and Gill (2016) described the muscle actions and general organization of the biomechanical environment of the parrot feeding apparatus. The parrot feeding apparatus is biomechanically defined by a hyper mobile craniofacial hinge, a dorsoventrally extended palatine, tubular pterygoid, and musculature that elevates and retracts the maxilla and palate.

Parrots have a number of derived musculoskeletal features that offer insight into feeding behavior. Temporal musculature (m. adductor mandibulae externus superficialis; mAMES, m. adductor mandibulae externus medialis; mAMEM, m. adductor mandibulae externus profundus; mAMEP, m. adductor mandibulae posterior; mAMP, and m. pseudomasseter, mPM, m. pseudomasseter profundus; mPSTp, m. pseudotemporalis superficialis; mPSTs), as in many other taxa, and musculus ethmomandibularis (mEM) adduct the mandible and many muscles of the parrot cranium act to control cranial kinesis (see Homberger 2003; Tokita 2003; Tokita et al. 2007). Musculus pterygoideus ventralis (mPTv) acts to pull the palatines caudally in respect to the neurocranium and mandible. Musculus protractor pterygoideus (mPPt) acts to raise the maxilla whereas musculus pterygoideus dorsalis (mPTd) acts to lower the maxilla.

The pterygoid acts as a rod in the heads of neognathe birds that are capable of cranial kinesis (Fig. 4-2A and 4-2B; Simonetta 1960; Hoese and Westneat 1996; Homberger 2003). Hoese and Westneat (1996) determined that a coupled pterygoid linkage model between the quadrate and palatine best predicted movement of the beaks of sparrows during bouts of song production. The pterygoid, as a coupled linkage element, is subjected to stresses in multiple orthogonal directions simultaneously and must be capable of resisting shear, compression, and tension throughout the shaft of the bone. The capability of the pterygoid, as well as the quadrate and palatines, to effectively moderate stresses and strains are largely unknown in parrots. The interaction between muscular and skeletal elements in the hyper-mobile parrot cranium are key components of parrot feeding behaviors and influence dietary preferences.

We analyze our first prediction using finite element models (FEM) and finite element analyses to investigate the biomechanical environment of the feeding apparatus of parrots and to discuss the evolutionary relationships of parrots and falcons. Our second prediction is assessed through analysis of the biomechanical environment of parrots and falcons to determine how those biomechanical environments manage stresses associated with feeding. We conclude by analyzing ancestral reconstructions of biomechanical and geometric properties of parrot crania and describe trends using a tree informed by Hackett et al. (2008), Mayr (2010), Kirchman et al. (2012); and Prum et al. (2015). Our methods and

biomechanical analyses will lead to an increase of our knowledge of the biomechanical environments of kinesis and birds overall. The new methods used methods used here can also be applied to other vertebrate taxa and their biomechanical environments. Ultimately, these new methods and biomechanical analyses will lead to a better understanding of evolution of feeding traits overall.

Methods

Materials and Imaging

The skulls of *Strigops habroptila* (FMNH 23529), *Nestor notabilis* (FMNH 289312), *Psittacus erithacus* (MUVC AV042), and *Falco peregrinus* (KU 90085) were scanned in a Siemens INVEON SPECT/CT (VA Biomolecular Imaging Center, Columbia, MO). The head of *Brotogeris chrysopterus* (FMNH 330249) was scanned in a BIR, Inc., Actis scanner with an image-intensifier detector and FeinFocus X-ray (University of Texas High-Resolution X-ray CT Facility, Austin, TX). *Deroptyus accipitrinus* (MUVC AV074) was scanned in a Zeiss Xradia Versa 510 (X-ray Microanalysis Core Facility, Columbia, MO). Finally, the skull of *Conuropsis carolinensis* (MCZ 342347) was scanned in a Nikon/X-Tek HMXST225 (Harvard Center for Nanoscale Systems, Cambridge, MA). Scan parameters of specimens discussed in this study are shown collectively in Table 1 and a phylogenetic tree of the specimens constructed using relationships in Hackett et al. (2008), Mayr (2010), Kirchman et al. (2012), and Prum et al. (2015) is shown in Fig. 4-1.

Model Construction

Microcomputed tomography (μCT; see Fig. 4-3A) data were segmented in Avizo Lite 9 (FEI Company, Hillsboro, OR). All bones were segmented as individual elements except the fused neurocranium. Stereolithographical (STL) models were generated for these segmented elements, smoothed, and independently segmented bones were placed in articulation. A single model file was constructed from multiple files, each containing single skeletal elements in Geomagic 2013 (3D Systems, Rock Hills, SC) (Fig. 4-3B). This permitted individual elements to retain their independent position in the skull without creating artefacts of skull fusion at joints in the next step of the modeling process. During this process the mouth of each model was opened to approximately 20°, measuring the angle from the base of the quadrate and using the tomial tooth (if present; if not the caudal maxillary ramphotheca insertion was used) and angulus mandibulae (caudal border of mandibular ramphotheca).

The finished STL models were imported into Strand7 (Strand7 Pty Ltd, Sydney, Australia) where they were meshed to create finite element models (FEM) using four-point tetrahedral elements and avian cranial bone material properties (*sensu* Rayfield 2011; E = 13.65 GPa, v = 0.3). Individual skeletal elements were joined to one another after meshing using beams which were assigned joint material properties (Chien et al. 2008; E = 2.35 MPa, v = 0.3). The number of beams per joint articulation

area is dependent on the size of the joint and distance from one element to another; joint beams were assigned maximum lengths of 0.5 – 1.0 mm.

Muscle Reconstruction and Force Estimation

Muscle attachment sites were mapped onto FEMs using information obtained through dissection of *Psittacus erithacus* and *Falco sparverius* (American kestrel MUVC AV070; approximation for *F. peregrinus*), observation of osteological correlates on museum specimens, and literature searches (Fig. 4-3C; Hofer 1950; Hull 1991; Tokita, 2004; Sustaita 2008; Lautenschlager et al. 2014; Carril et al., 2015). Individual muscle maps are shown for each taxon in Figs. 4 – 6. Central axes of tendons were measured in *Psittacus erithacus* to determine anatomical details of muscle fiber length and pennation of fibers. These were compared to the literature (Sustaita 2008; Carril et al., 2015; Table 2) and used to estimate physiological cross–sectional area (PCSA) using equation 1 (Sacks and Roy, 1982):

$$PCSA = \frac{V_M}{l_f} \cdot \cos(\theta) \quad (1)$$

where V_M is the muscle volume, l_f is the fiber length, and θ is the pennation angle of the muscle. Jaw muscle forces were calculated using muscle volume, fiber architecture, and centroids of muscle attachment sites. Resultant force vectors were assigned to muscle attachment sites in FEMs *sensu* Sellers et al. (2017) and Cost et al. (2019) and using equation 2:

$$F_M = PCSA \cdot T_{specific} \quad (2)$$

where $T_{specific}$ is specific tension (Porro et al., 2011), and F_M is muscle force. Calculated muscle parameters serve as input for the BoneLoad workflow (Davis et al. 2010; Sellers et al. 2017; Cost et al. in press) which enables distributed force loading at muscle attachment sites in FEMs. All models were constrained bilaterally at the jaw joint of the quadrate and at a posterior bite point along the lateral bony surface of the rostrum. This bite point was posterior to the tomial tooth in all taxa, and the constraints were fixed in all axes prior to loading (Fig. 4-3E).

Scan Processing for Geometric Analysis

Microcomputed tomography scans were secondarily processed to measure geometric properties of the pterygoid bone (Fig. 4-3G; Lieberman et al. 2004). The left pterygoid was oriented using orthogonal slices in Avizo such that the shaft of the pterygoid was oriented obliquely. CT images were resampled using this view and slices containing the left pterygoid were cropped out of the larger data set for processing using BoneJ (Doube et al. 2010), a plugin for ImageJ (Schneider et al. 2012). Images were then processed using the threshold tool to produce black and white images of the pterygoid and surrounding space (See Table 1 for threshold values). These images were processed using Slice Geometry in BoneJ to calculate cross-sectional area (CSA) of the bones. Principal

stresses are shown as acting in particular directions along the z-plane such that mediolateral stresses are forces acting upon the z-plane in a mediolateral direction.

Muscle Orientation Visualization, Finite Element, and Geometric Analysis

Muscle resultants were analyzed using ternary plots, which were constructed to display muscle resultant vectors (*sensu* Cost et al. in prep.; Fig. 4-3D). We analyzed the strain patterns of the whole quadrate, pterygoid, and palatine from the left side of each model (Fig. 4-3F). Individual brick strain values were collected from Strand7, and a strain profile for each bone in each taxon was developed. The strain values were simplified to equivalent Von Mises strains (ε_{eq}) using equation 3 (Chen and Han 1988):

$$\varepsilon_{eq} = \frac{2}{3} \cdot \sqrt{\frac{3(\varepsilon_{xx}^2+\varepsilon_{yy}^2+\varepsilon_{zz}^2)}{2} + \frac{3(\gamma_{xy}^2+\gamma_{yz}^2+\gamma_{zx}^2)}{4}} \quad (3)$$

where ε_{xx} is the strain in the xx direction, ε_{yy} is the strain in the yy direction, ε_{zz} is the strain in the zz direction, γ_{xy} is the strain in the xy direction, γ_{yz} is the strain in the yz direction, and γ_{zx} is the strain in the zx direction.

The shape of the distribution and the median strain allow comparisons across taxa. The data is truncated on the high end at 3000 με, which represents a “high but physiological level of normal strain” (Rubin et al. 1992, p. 306). Snively and Russell (2002) determined that low resolution models (2000 to 3000 tetrahedral elements) were capable of producing sufficiently accurate data in

finite element modeling and determined that “higher resolution would obviate instances of strain artifacts”. More recent studies have expanded upon the view that higher resolution models are more capable of eliminating accidental modeling artifacts as computer models have increased in complexity (e.g. Dumont et al. 2009; Rayfield 2011; Bright 2014). Our models are approximately 100 times this size, and are therefore of significant resolution that strain artifacts are considerably less likely to manifest in the data (see Table 1). The median values, represented by a vertical black bar within the data, include all strain values and therefore show a representative median strain in each palatal element.

Muscle forces were evaluated using three separate measures. Total force of all cranial muscles was measured against the skull width of the specimens. Skull width was measured across the skull at the quadrates. Bite force for each taxon was calculated using a posterior bite caudal to the tomial tooth; when absent the approximate location of the caudal edge of the ramphotheca was used to place bite points on models. Direction specific muscle forces acting on the pterygoid were calculated for mPTd and mPTv by multiplying the estimated muscle force of each muscle by its directional component (rostrocaudal or dorsoventral) and adding the two resulting directional muscle forces together. Rostrocaudal muscle force was plotted against cross-sectional area (CSA) of the pterygoid. Rostrocaudal force down the shaft of the pterygoid

(compression) was calculated using the shaft of the pterygoid and the midline ridge of the interorbital septum in ventral view as rays of the angle. Dorsoventral muscle force was plotted against the second moment of area (I) along the dorsoventral axis. Dorsoventral angles of pterygoids were calculated using the shaft of the pterygoid and an inferred plane from the pterygopalatine articulation to the foramen magnum in left lateral view as rays of the angle. Rostrocaudal and dorsoventral angles of pterygoids are shown in Table 3.

Geometric properties of the pterygoid were analyzed for resistance to compression and bending (Fig. 4-3G). The second moment of area (I), which indicates resistance to bending in an axis, is reported about dorsoventral (I_{DV}) and mediolateral (I_{ML}) axes (Biewener and Taylor 1986; Demes et al. 1991; Demes and Jungers 1993; Cole and Van der Meulen 2011). The polar moment of area is also reported here (J). The polar moment of area, like second moments of area, indicates rigidity, but in regard to torsional loads in the midshaft of the pterygoid (Selker and Carter 1989; Demes and Jungers 1993; Van Eijden 2000; Cole and Van der Meulen 2011). Section moduli (Z), which represent bending strength in specific planes, are reported in dorsoventral (Z_{DV}) and mediolateral (Z_{ML}) planes (Demes and Jungers 1993; Ruff 2000; Cole and Van der Meulen 2011). We also report median ellipticity, and CSA of the pterygoid, which is proportional to resistance to axial loading along the diaphysis. Geometric property values of the pterygoid are presented in Table 3. The CSA of the diaphysis of the pterygoid was used in combination with principal stress in mediolateral (xx), dorsoventral (yy), and rostrocaudal (zz) directions (gathered

from FEA data) along the z-plane to qualitatively analyze the pterygoid's resistance to bending (Fig. 4-3H). Articular surfaces were not described in to bending resistance; however, the articular surfaces are represented in the FEA results of the bending resistance data.

Character Analysis

Phylogenetic trees were analyzed using Mesquite 3.6 (Maddison and Maddison 2018) (Fig. 4-3I). Trees were constructed using molecular data and phylogenies from Hackett et al. (2008), Mayr (2010), Kirchman et al. (2012), and Prum et al. (2015). Nineteen continuous traits and 5 discrete traits were documented in the taxa sampled in this study. Ancestral reconstructions of continuous traits were analyzed using squared-changed parsimony (Maddison 1991; Garland Jr. et al. 1997). Discrete traits were analyzed using maximum likelihood (ML) reconstruction (Pagel 1999). The characters are presented in Table 4. A λ transformation was effected on branch lengths of the tree, ultrametrically aligning the branch tips at the sampled specimens (Pagel 1999).

Results

Three-dimensional Muscle Orientations and Relative Forces

Muscle resultants are displayed for each taxon in Figs. 7 (*Falco*), 8 (A, *Nestor*; B, *Strigops*; C, *Psittacus*) and 9 (A, *Brotogeris*; B, *Conuropsis*; C, *Deroptyus*). Ternary plots are shown for individual muscles in Fig. 4-10. The temporal musculature is largely rostrocaudal overall with variations

and a few exceptions (Fig.10). The mAMEM (Fig. 4-10A) of both strigopoid parrots are largely rostrocaudal (54.7% in *Nestor* and 33.6% in *Strigops*), though *Strigops* exhibits a larger dorsoventral component (58.1%) and *Nestor* a small mediolateral component (10.2%). *Conuropsis*, *Deroptyus*, and *Psittacus* all possess mPM (Fig. 4-10G); *Falco*, *Nestor*, *Strigops*, and *Brotogeris* do not possess this muscle. In *Conuropsis* and *Deroptyus* mPM exhibit a highly dorsoventral orientation (78.2% in *Conuropsis* and 80.3% in *Deroptyus*) whereas in *Psittacus* the orientation of mPM is largely mediolateral (69.9%) with small rostrocaudal (10.0%) and dorsoventral (20.1%) components. In all of the parrots sampled mAMP (Fig. 4-10D) is highly rostrocaudal (between 55.3% in *Strigops* and 91.8% in *Nestor*) with some small variation dorsoventrally (44.2% in *Strigops*), mediolaterally (20.2% in *Conuropsis*), or both (17.8% dorsoventrally and 9.5% mediolaterally in *Deroptyus*) because of the almost parallel orientation between the quadrate and mandible. The pseudotemporalis muscles (m. pseudotemporalis profundus, mPSTp, Fig. 4-10E in *Falco* only; m. pseudotemporalis superficialis, mPSTs, Fig. 4-10F) are overall highly similar across taxa. In all of the taxa presented here, mPSTs is contains rostrocaudal (between 38.6% in *Strigops* and 71.7% in *Deroptyus*) and dorsoventral components (between 25.4% in *Deroptyus* and 56.5% in *Strigops*); *Falco* exhibits the most dorsoventral orientation of all taxa studied (74.8%). In *Falco* mPSTp contains less mediolateral orientation (8.6%) and slightly more rostrocaudal orientation (15.9%). Musculus adductor mandibulae posterior possesses substantial dorsoventral (74.4%) and mediolateral (23.4%) orientation in *Falco*.

Because mAMP is attached to the quadrate and mandible, its resultant orientation is heavily influenced by the orientation of the quadrate to the mandible. The quadrate is rotated medially and at an oblique angle to the mandible in *Falco* relative to its position in parrots.

The pterygoideus muscles (m. pterygoideus dorsalis, mPTd, Fig. 4-10H; m. pterygoideus ventralis, mPTv, Fig. 4-10I; m. protractor pterygoideus, mPPt, Fig. 4-10J; and m. ethmomandibularis, mEM, Fig. 4-10K) possess substantial mediolateral orientations and dorsoventral orientations in the case of mPPt; in *Nestor* (Fig. 4-8A) and *Falco* (Fig. 4-7) the dorsoventral orientations of mPPt are greater than in the other taxa presented here (72.5% in *Nestor* and 69.4% in *Falco*; Fig. 4-10). Musculus pterygoideus dorsalis exhibits appreciable rostrocaudal (between 30.1% in *Falco* and 65.9% in *Strigops*) components in all taxa. *Falco* exhibits the largest mediolateral (29.4%) component in mPTd. The unique parrot muscle mEM originates as a belly of mPTd and develops so that it attaches superiorly on the ethmoid and the medial mandible inferiorly. The resulting orientation of the muscle is extremely dorsoventrally oriented (between 76.8% in *Psittacus* and 94.9% in *Strigops*), and its attachments along the midline of the cranium and the medial portion of the mandible cause a small mediolateral component (between 4.9% in *Strigops* and 16.5% in *Psittacus*) to exist in all taxa as well. Variable, but small, rostrocaudal components (between 0.2% in *Strigops* and 8.4% in *Brotogeris*) of orientation are also associated with the muscle, but mEM is

largely a dorsoventral muscle used to close the jaw. The orientation of mPTv is largely rostrocaudal (between 33.4% in *Conuropsis* and 64.5% in *Strigops*) and mediolateral (between 27.1% in *Brotogeris* and 44.9% in *Conuropsis*). In parrots the attachments of mPTv are along the ventral borders of the palatine and pterygoid, passing ventrally to the mandible and wrapping onto the lateral and caudal quarter of the mandible. The lateral mandibular attachment of mPTv also exists in *Falco*, though this attachment is smaller than in parrots.

Dorsoventral height of the palatine shelves and their resulting protrusion ventral to the mandible, as well as angle of the pterygoid, influence the dorsoventral components of mPTv. *Psittacus* (33.9%; Fig. 4-8C) and *Conuropsis* (21.7%; Fig. 4-9B) possess relatively superior attachments to the palatine and pterygoids than other taxa, thereby increasing the dorsoventral components of mPTv. Taxa with palatine and pterygoid attachments of mPTv relatively closer to the mandibular attachment dorsoventrally exhibit smaller relative dorsoventral components of the muscle. Musculus depressor mandibulae (mDM; Fig. 4-10L) exhibits an orientation like that of mEM that is extremely dorsoventral in all parrot taxa (between 85.4% in *Brotogeris* and 99.1% in both *Strigops* and *Deroptyus*; Fig. 4-10). *Brotogeris* (14.5%; Fig. 4-9A) and *Falco* (22.3%; Fig. 4-7) exhibit rostrocaudal orientations as well in mDM, which separates their points in Fig. 4-10 from the other taxa. Despite orientations that are close to parallel, mEM and mDM are located on opposite sides of the jaw joint and therefore perform opposite actions. Musculus ethmomandibularis adducts the mandible whereas mDM abducts the mandible.

Relative Muscle Forces and Bending Resistance of the Pterygoid

Verwaijen et al. (2002), Herrel et al. (2005a), and O'Brien et al. (2019) found that skull width was the best predictor of bite force in lacertid lizards, finches, and crocodilians, respectively. Bearing this in mind, we predicted that the total muscle forces in respect to the width of their skulls would show a similar result in parrots (Fig. 4-11A). The expected relative total muscle force (F_T) is predicted by the regression line in Fig. 4-11A. The calculated regression model accounts for 86.7% of the variance of the sampled data.

Strigops, possessing the largest skull width, also possesses the largest F_T and is represented in the upper right region of the graph. *Strigops* is slightly above predicted relative F_T force given its skull width. *Conuropsis* and *Deroptyus* also slightly over perform and have larger than predicted muscle forces for their skull widths. *Nestor* and *Falco* are both below the predicted F_T for their skull widths. This means that *Nestor* and *Falco* are the only underperforming taxa presented here. *Brotogeris* and *Psittacus*, on the other hand, possess the predicted amount of total force for their skull widths. *Brotogeris* also possesses the smallest skull in width and volume and also possesses the smallest F_T, placing it in the lower left region of the graph as a result. The remaining taxa cluster together in the central area of the graph. This shows that their heads are of relatively similar size and produce similar F_T for their sizes.

Bite force (F_B) in relation to skull width appear appreciably different from the relationship between F_T and skull width (Fig. 4-11B). The regression model of these data accounts for 37.4% of the variance. *Strigops* maintains a high F_B in relation to skull width and all other parrots, with the exception of *Nestor*, also produce F_B slightly higher than expected in relation to their skull widths. *Nestor* and *Falco* both produce F_B lower than those expected for their respective skull widths. The mechanical advantage (MA) of parrots in this study is defined by the relationship between F_T and F_B (Fig. 4-11D). Total muscle force, F_T, is the in-lever of the system and F_B is the outlever of the system. The fulcrum of this lever system is the jaw joint, and because of this the feeding apparatus can be described as a 3rd class lever. Mechanical advantage appears to show a different relationship than the F_B versus skull width graph does (Fig. 4-11C). The regression model of these data accounts for 66.3% of the variance in the data. *Strigops* and *Psittacus* maintain high relationships between the produced bite forces with regard to the total muscle force that the parrots are capable of producing. Remarkably, *Brotogeris* generates a higher than expected bite force for the total muscle force that it produces. *Deroptyus* produces approximately the expected bite force for the total muscle force it generates whereas *Conuropsis* produces slightly under the expected amount of bite force for total force. *Nestor* and *Falco* generate the lowest bite force for the amount of total muscle force each produces; *Falco* generates the least bite force given its total force production of all sampled taxa.

Geometry and Bending Resistance of the Pterygoid

Forces of mPTd and mPTv decomposed into rostrocaudal and dorsoventral components were plotted (Fig. 4-12A and 12B) against CSA and I_{DV} respectively. A regression model for Rostrocaudal Force vs CSA and Dorsoventral Force vs. I_{DV} were fitted to their respective plots. The regression model for Rostrocaudal Force vs CSA accounts for 63.7% of the variance in the data. The Dorsoventral Force vs. I_{DV} regression model accounts for 14.2% of the variance in the data. Values closest to this predictive linear model represent the taxa most closely approaching the predicted values. Values above and below the predictive linear model represent taxa that are overbuilt and underbuilt, respectively, to resist the bending which their pterygoids are subjected to. Rostrocaudal forces represent axially compressive forces along the shaft of the pterygoid (Fig. 4-12A). Taxa that appear best constructed to resist compressive forces include *Psittacus*, *Strigops*, and *Conuropsis*. *Deroptyus* and *Nestor* possess overbuilt pterygoids whereas *Falco* and *Brotogeris* possesses underbuilt pterygoids. Dorsoventral forces acting on the pterygoid are acting in tension along the diaphysis (Fig. 4-12B). Of the taxa sampled, *Deroptyus* and *Nestor* are closest to the expected resistance to dorsoventral bending. *Strigops*, *Falco*, and *Brotogeris* are all underbuilt whereas *Conuropsis* and *Psittacus* are overbuilt.

We report medians of collected values for geometric properties along the diaphysis of the pterygoid and we exclude the articular surfaces

at the rostral and caudal ends (Table 3). The section moduli in both planes are similar in *Nestor*, *Strigops*, and *Psittacus*. *Brotogeris* possesses the lowest section moduli and *Conuropsis* and *Deroptyus* possess similarly low section moduli in single planes; dorsoventrally in *Conuropsis* and mediolaterally in *Deroptyus*. The opposing section moduli of *Conuropsis* and *Deroptyus* (mediolateral and dorsoventral respectively) exhibit slightly higher bending resistance estimates. *Falco* exhibits section moduli that are in the middle of the range presented for all taxa.

Plots of pterygoid CSA are variable across the taxa sampled here (Figs. 5 and 6). The stress range was informed by known limits of compressive fracture stresses in bovine, human, and avian bone (Pennycuick 1967, 1968; Yamada 1970; Currey 2006; Hart 2017). Principal stresses in the taxa presented here (Figs. 5 and 6) are reported in the range of -150 to 150 MPa; cooler colors indicate compression of the pterygoid (0 to -150 MPa) and warmer colors tension of the pterygoid (0 to 150 MPa). Colors outside of the range register as white in the finite element analysis. The white color values represented in the heat maps indicate failure of bone.

The strigopoid parrots *Nestor and Strigops* exhibit substantially different pterygoid CSAs from other parrots sampled (Fig. 4-14A and 14B). *Nestor* and *Strigops* both exhibit areas of high stress along the entirety of the pterygoid shaft in areas of lower CSA, especially when forces are applied to the pterygoid in rostrocaudal and mediolateral directions. The tensed rostral portion of the pterygoid appears to exhibit the highest stress concentration in the pterygoid

shaft. Dorsoventral forces also cause high stresses, though in *Strigops* the higher CSA of the caudal portion of the pterygoid appears to dissipate stress and resist bending more than the rest of the pterygoid shaft.

Psittacid parrot (*Psittacus*, *Brotogeris*, *Deroptyus*, and *Conuropsis*; Fig. 4-14C – 14F) pterygoids exhibit both smaller CSAs and lower stress concentrations than the pterygoids of the strigopoid parrots. In *Psittacus* the caudal portion of the pterygoid shaft is subjected to relatively high stresses from forces oriented rostrocaudally. This area coincides with a relatively small CSA in *Psittacus* pterygoids and the articulation with the mobile quadrate which is likely imparting force directly on the pterygoid. An area of intermediate CSA caudal to the lowest CSA region of the pterygoid shaft here is also subjected to very high stresses in relation to mediolateral forces acting on the pterygoid (Fig. 4-14C). *Psittacus* and *Conuropsis* have similar rostral pterygoid profiles of stress in rostrocaudal force application. *Brotogeris* is the smallest taxon presented here and the pterygoid CSA ranging between approximately 0.2 and 0.7 mm^2 is the smallest CSA among these taxa (Fig. 4-14D). Stress on the pterygoid of *Brotogeris* is in the middle range throughout the diaphysis. The diaphysis of the pterygoid appears to uniformly react to forces in all directions which are all representative of the middle range of stress.

Conuropsis and *Deroptyus* are overall more similar to one another than any of the other taxa presented here are to one another (Figs. 4-14E, 14F, respectively). The two taxa have similar CSA ranges (~0.2 to 1.1

mm^2 in *Deroptyus* and ~0.2 to 1.3 mm^2 in *Conuropsis*) and appear to express similar stress profiles. *Conuropsis* exhibits a lower overall stress within the shaft of the pterygoid. However, *Deroptyus* exhibits similarly low stress concentrations in respect to the rostrocaudal and mediolateral forces acting on the pterygoid (Fig. 4-14F). The rostroventral aspect of the pterygoid of *Conuropsis* shows higher stress concentrations in the diaphysis (Fig. 4-14E). These rostroventral stress concentrations are not represented in *Deroptyus*.

Quantitative Strain Sampling of the Palate

Variation in strain profiles are extensive between the strigopoid (*Strigops* and *Nestor*) and psittacoid (*Psittacus*, *Brotogeris*, *Deroptyus*, and *Conuropsis*) parrots. The median values of the data for the quadrates are all reasonably similar; *Brotogeris* and *Falco* representing the lowest and highest median values respectively (Table 6). This is not the case in either the palatine or the pterygoid, where the median values range considerably in their value. In the palatine and the pterygoid *Brotogeris* represents the lowest median; though this is likely indicative of the size of *Brotogeris*. The parrots *Nestor* and *Psittacus* exhibit similar strain profiles in the palatine and pterygoid. *Conuropsis* and *Deroptyus* also possess similar palatine and pterygoid strain profiles. The general shapes of the palatine and pterygoid profiles of *Brotogeris* are similar to other parrots, though the overall range of the values are lower than the other parrots. The range and median are reflective of the forces produced by the cranial musculature of *Brotogeris*, which is similar to that of *Falco*. The range of *Strigops*

values and the median in the palatine and pterygoid are lower than most other parrots except for *Brotogeris*, despite the large size of the *Strigops* cranium.

Falco performs in a similar matter to all Psittaciformes taxa with regards to strains in the quadrate (Fig. 4-15). The median strain, indicated by a vertical black bar in the graphs, is higher in *Falco* than it is in the Psittaciformes taxa also, indicating that the overall environment of the quadrate is relatively more strained in *Falco* than it is in parrots. The environments of the palatines and pterygoids are more disparate than that of the quadrates. In the palatine (Fig. 4-15B) and pterygoid (Fig. 4-15C) *Falco* exhibits strain profiles that approximate the shape of those of the small parakeet *Brotogeris* rather than those of other parrots.

Trait Evolution

Phylogenetic trees based on Hackett et al. (2008), Mayr (2010), Kirchman et al. (2012), and Prum et al. (2015) traced continuous and discrete character traits independently. Trees with continuous traits are described using squared-change parsimony which describes a unit of evolutionary change equivalent to the steps between characters described in discrete analyses (Maddison 1991). Discrete characters, on the other hand, are described as estimates of rates of evolution using maximum likelihood (Pagel 1999). Discrete characters attempt to recreate ancestral states using probabilistic maximum likelihood. The likelihoods below are

discussed in terms of estimated rate of gains of traits and - log likelihood (- log L) probabilities at the terminal nodes. The discrete characters presented here are morphological as well as ecological in nature.

Figure 4-16 shows ancestral reconstructions for the character traits for median Z_{DV}, median ellipticity, median palate strain, and total muscle force divided by skull volume. More trees are contained in supplemental data. Median ellipticity and median Z_{DV} trees trace characteristics of pterygoid geometry across parrots (Fig. 4-16B). The overall shape of the pterygoid in cross-section tracked via the shape parameter ellipticity shows that the shape of the pterygoid is appreciably consistent across all taxa sampled here. *Strigops*, *Psittacus* and *Conuropsis* are all derived from the basal condition (Fig. 4-16A). However, *Psittacus* and *Conuropsis* appear to be more derived than *Strigops*. Median Z_{DV} as a measure of bending resistance appears to be most derived in the Neotropical parrots *Brotogeris*, *Conuropsis*, and *Deroptyus* and also in *Falco*, compared to the hypothesized ancestral condition (Fig. 4-16B). *Nestor* appears to have secondarily evolved a character state similar to the root node section modulus (both exhibiting squared-lengths of 0.167) whereas *Strigops* and *Psittacus* have evolved character states different from the ancestral condition and the Neotropical condition. Median CSA (Fig. 4-16C) and median I_{DV} (Fig. 4-16D), bending resistance informing characteristics of shape, appear to be unifying character states of the Neotropical parrots *Brotogeris*, *Deroptyus*, and *Conuropsis*. *Psittacus*, *Strigops*, and *Nestor* are all derived from one another and the Neotropical parrots.

Median strains of the quadrate (Fig. 4-17A), palatine (Fig. 4-17B), pterygoid (Fig. 4-17C), and the median strain of the entire palate (Fig. 4-17D) were analyzed as continuous characters of the strain populating the skeletal elements during a bite. Squared-change parsimony of this character indicates that all sampled taxa are uniquely derived in their capabilities to exhibit the unique strain associated with each skeletal element as well as the palate as a whole. Two exceptions to this are the median strains exhibited by the quadrates of the strigopoid parrots *Nestor* and *Strigops* which are closely related and the strains exhibited by the palatines of the Neotropical parrots *Deroptyus* and *Conuropsis* which also appear closely related. Median palate strain is the widest ranging character trait traced in these trees overall.

The shape characters I_{min} (Fig. 4-18A), I_{max} (Fig. 4-18B), Z_{min} (Fig. 4-18C), Z_{max} (Fig. 4-18D), I_{ML} (Fig. 4-19A), and Z_{ML} (Fig. 4-19B) are indicative of the minimum and maximum values of the pterygoid diaphysis to resist bending in the major (I and Z “min”) and minor (I and Z “max”) axes of the bone and the second moment of area and section modulus in the mediolateral axis and plane, respectively. All six shape measures are characterized by similar rates of evolution among the Neotropical parrots whereas the other parrots are derived from one another and the Neotropical parrots. An exception to this is exhibited by the strigopoid parrots in I_{ML} (Fig. 4-19A) only. *Nestor* and *Strigops* possess similar rates of evolution in the character values representing the state for I_{ML}.

Biomechanically important aspects of the position of the pterygoid in the cranium, the angles at which the pterygoid articulates with the palatobasal joint in Z (rostrocaudal; Fig. 4-19C) and Y (dorsoventral; Fig. 4-19D) planes, are highly variable across the sampled parrots. The evolutionary rates of both characters appear to be very similar and steady. The relationships at the branch tips for these characters do not appear to show any close relationships between the sampled taxa though. Polar moments (J) is the final character of shape described in this analysis (Fig. 4-20A). Polar moments are related to other shape characters and the Neotropical parrots, as in other shape characters, are grouped together whereas the other parrots and *Falco* are again derived from one another and the Neotropical parrots.

Continuous characters related to size, but not used in calculations of relative force, included body mass (Fig. 4-20B), skull length (Fig. 4-20C), and skull volume (Fig. 4-20D). The strigopoid parrots group together for body size evolution. *Psittacus* groups with the Neotropical parrots and *Falco* for body size. Skull length is more variable in its representation of character states across the tree. *Psittacus* and *Falco* group together as exhibiting similar character states (i.e. have similar skull lengths). Skull volumes in the sampled taxa again similar in *Nestor* and *Psittacus*. The estimated rates of evolution for skull length are far lower than for skull volume (389.49 compared to 9.22) among the sampled parrots.

Character states of force are reported as calculated total (absolute) cranial muscle force (Fig. 4-21A), bite force (Fig. 4-21B), relative total force (Fig. 4-21C),

and relative bite force (Fig. 4-21D). The character states for total cranial and bite force are measured in Newtons (N) whereas the relative forces are calculated as Newtons per millimeter (N/mm). Total muscle force states are similarly probable with the exceptions of the absolutely largest and smallest taxa; *Strigops* and *Brotogeris* respectively. Bite force is more variable overall. Character states (force produced) are similar in *Nestor* and *Brotogeris*, though the rates of evolution between the two taxa are appreciably different. Likewise, *Psittacus* and *Deroptyus* generate similar bite forces, though the rates of evolution describing the separation between these taxa are smaller than those between *Nestor* and *Brotogeris*. Relative muscle and bite forces eliminate size from the character state by dividing the absolute muscle and bite forces by the width of the skull. These characters, therefore, are not continuous across the size range, but are more reflective of the force production capabilities of each taxon. Character states for relative total force (Fig. 4-21C) are similar in *Nestor*, *Psittacus*, and *Falco*. Rates of evolution between *Psittacus* and *Nestor* are higher than between either and *Falco*. Relative bite force (Fig. 4-21D) characters group the Neotropical parrots together with one another. Rates of evolution across this character are high and character states are separated by few steps throughout the parrots.

Bite force as a unit of total force (bite force divided by the total force; Fig. 4-22A) and skull width (Fig. 4-22B) are the final continuous characters analyzed in this study. Character states of bite force divided by

total force represent the taxon's relative bite force production per overall force generation. The most derived taxon in this character set is *Brotogeris*, which produced a greater than predicted bite force for its total force generation (Fig. 4-11C). *Deroptyus*, *Conuropsis*, and *Nestor* exhibit similar character states; however, *Deroptyus* and *Conuropsis* are reconstructed here as sister taxa and possess a smaller rate of evolution difference than *Nestor* and either of the other taxa. *Deroptyus* and *Conuropsis* therefore cluster together and separately from *Nestor*. Skull width (Fig. 4-22B) is a size dependent character; width from quadrate to quadrate measured in millimeters. Character states are similar in *Psittacus*, *Deroptyus*, *Conuropsis*, and *Falco* (because their skulls measure between 30 and 38mm wide). Rates of evolution for skull width are higher than for skull length in parrots and lower than skull volume overall.

The ecological discrete characters presented in this study are the most extensive discrete characters, offering a larger number of character states, and aim to describe the likelihood of evolution of particular niche roles in parrots sampled here. Primary diet (Fig. 4-22C) was generalized to include five categories; carnivory was considered ancestral (primarily eating meat; assigned state "0"), granivory (seed and fruit eating treated equally, "1"), omnivory (food generalists; "2"), nectarivory (nectar and flower eating; "3"), and folivory (leaf eating; "4"). Parrots are largely granivorous (*Psittacus*, *Conuropsis*, and *Deroptyus* in this study) and this common characteristic, especially in the non-strigopoid parrots, may be indicated in the low estimate of rate of evolution and the high –log likelihood, which indicates a lower probability of evolutionary

change. *Brotogeris* is an exception among the non-strigopoid parrots, primarily feeding on nectars and flowers. Probabilities for this trait's evolution are around 10 – 15% (indicated by the color yellow on the internal nodes). Folivory and omnivory are similarly probable until the strigopoid parrots and the psittacid parrots differentiate in this tree despite being represented by a single taxa each; *Nestor* is omnivorous and *Strigops* is a folivore.

Habitat (Fig. 4-22D) was also generalized and was assigned 3 categories; jungle/rainforest habitats were considered ancestral for parrots (assigned state "0"), montane/open cliff and man-made structures ("1"), and non-jungle deciduous and coniferous forest (this includes subtropical laurel forests, "2"). Throughout this tree the probabilities of internal nodes retain a 33% probability. Neotropical parrots *Brotogeris* and *Deroptyus* and the Afrotropical parrot *Psittacus* are all assigned the ancestral character state. *Conuropsis*, native to a subtropical region, and *Strigops*, native to subtropical laurel forests, were assigned to the same character state. *Nestor* and *Falco* were assigned the montane, cliff, and man-made structure character. As characters are each assigned across 33% of the sample the internal node probability appears to directly reflect this assignment. Internal node probabilities indicate that regardless of clade habitat use is predicted to be equally probable among all species.

Presence and absence of the muscles mAMEM (Fig. 4-23A), mPM (Fig. 4-23B), and mEM (Fig. 4-23C) are presented and dichotomous traits

(presence or absence only). Presence of mAMEM and absence of mPM and mEM are considered the ancestral state characters for these three character traits. The tree for mEM expresses the lowest rate of evolution, likely because mEM (Fig. 4-23C) is a muscle described for all parrots and therefore only *Falco* exhibits the ancestral condition of not possessing mEM. On the other hand, mAMEM (Fig. 4-23A) is often indistinguishable from mAMES, rather than truly absent, in parrots. The muscle mAMEM is therefore described in few parrots outside of the strigopoid parrots. The evolutionary rate for the loss or masking of this muscle is therefore estimated to be higher among parrots by this tree (estimated rate of 0.1081 and –logL of 3.6851). Rates of evolution and probability of development of mPM are likewise high (estimated rate of 0.2418 and –logL of 4.4596). A parrot specific muscle of diverse presence, mPM is accounted for in *Deroptyus*, *Conuropsis*, and *Psittacus* only. Probability of presence at the nodes is represented as approximately 45 – 50% for non-psittacid parrots.

The final discrete characters represented here are skeletal characters, namely the presence of the tomial tooth (Fig. 4-23D) and the presence of a suborbital arch (Fig. 4-24A). The tomial tooth is a bony structure on the rostrum present in some parrots and falcons, therefore considered to be ancestral for parrots, and the suborbital arch is a parrot specific structure, though not found in all parrots, therefore its absence is considered ancestral. A bony tomial tooth (Fig. 4-23D) is present in the Neotropical parrots as well as *Falco*. Its absence in *Psittacus* and the strigopoid parrots does not appear to affect the rate of evolution of this character (0.1646) or its -logL (4.0495) substantially. The

suborbital arch is a bony structure that has been shown to have evolved multiple times across parrots independently of other cranial musculoskeletal elements in parrots (Tokita et al. 2007). The rate of evolution of the bony suborbital arch (Fig. 4-24A) is fairly high (17.9492) and its evolution also has an appreciable probability (-logL = 4.8520). The bony suborbital arch is present in *Strigops*, *Deroptyus* and *Conuropsis*. Internal nodes throughout the tree indicate a 50% probability of the possessing a suborbital arch at that node.

Discussion

Muscle Orientations and Force

Temporal muscles (mAMES, mAMEM, mAMEP, mAMP, mPSTs, mPSTp, and mPM) possess considerable rostrocaudal components in all sampled taxa. One exception to this is the mAMP of *Falco* which is more dorsoventrally and mediolaterally oriented. Mediolateral components of these muscles are largely the result of mediolateral expansion of the braincase of birds that resulted from increased encephalization during the time that the avian skull (Balanoff et al. 2013; Bhullar et al. 2016; Fabbri et al. 2017). The exceptions to this are the parrot-specific temporal muscle mPM, which is variably attached in the temporal region at the zygomatic process or the suborbital arch. The mPM is attached to the suborbital arch in *Conuropsis* and *Deroptyus* and to the postorbital process in *Psittacus*. The resulting orientations of these muscles are therefore highly

dorsoventral instead of rostrocaudal as their cranial attachments are almost directly dorsal to their mandibular attachments. The suborbital arch and attached mPM change only this muscle and therefore do not change the overall jaw closing muscle orientation. The mAMP in *Falco* is more mediolaterally and dorsoventrally oriented. Because of the relationship between mAMP attachments and the quadrate, differences in the use of the palate and orientation of the quadrate are notable in the orientation of mAMP. In all parrots the quadrate rotates at the jaw joint to open the mandible and at the otic joint to initiate cranial kinesis. *Falco* does not actively engage considerable kinesis and the quadrate is obliquely angled to the mandible and cranium. The oblique orientation of the quadrate and the postorbital ligament restrict movement at both the otic and jaw joints. Hull (1991) reports a maximum change at the craniofacial joint of 3° for *Falco* during bouts of cranial kinesis using a cadaveric specimen, which is unlikely to be a statistically significant movement. The movement described by Hull (1991) likely exceeds the natural capabilities of *Falco* due to the absence of active muscular restraint of the palate by mPPt and mPTd. Similarly, Claes et al. (2017) determined that domesticated chickens (*Gallus gallus domesticus*) were capable of rotating their quadrates between 3 – 5˚ to effect 11 – 15˚ of kinesis at the nasofrontal hinge. Cost et al. (in press) showed that a 5˚ rotation of the quadrate, the upper rotational limit of Claes et al. (2017), in modeled lepidosaurs and archosaurs can produce biologically relevant and important stress patterns that inform the biomechanical environment of the feeding apparatus.

The pterygoideus muscles are largely responsible for mobilization and stabilization of the palate and cranial kinesis (Hofer 1950; Burton 1974; Vanden Berge and Zweers 1993; Homberger 2003). In parrots and falcons, mPTv wraps around the ventral border of the mandible and attaches to the caudolateral side. Regardless of orientation of the palatine shelf (parrots possess more vertical orientation than falcons), mPTv originates on the ventral surface of the palatine and inserts on the caudal and lateral side of the mandible. The size of the mandibular attachment influences the resultant plotted in ternary space; for example, *Psittacus* (Fig. 4-8A) and *Conuropsis* (Fig. 4-9B) possess wide mandibular attachments that cause the resultant to exhibit a centroid that has large mediolateral and rostrocaudal components but also substantial dorsoventral components as well. The resultant orientation may also relate to overall palatine length rostrocaudally as longer vertical palatine shelves in parrots cause the palatine and pterygoid attachments of mPTv to be more ventral than those taxa with shorter palatine shelves such as in *Falco*. The height of palatine shelves was not measured in this study and as such, further investigation into the relationship between palatine shelf length and resulting mPTv orientation is needed.

The mEM is also a unique muscle with a highly dorsoventral resultant orientation that exhibits some small rostrocaudal and mediolateral components. Attaching dorsoventrally on the ethmoid superiorly and medial mandible inferiorly, this muscle mainly adds to jaw

closing force production in parrots (Hofer 1950; Burton1974; Vanden Berge and Zweers 1993; Homberger 2003; Tokita 2003; Carril et al. 2015; Toft and Wright 2015). The added force of this muscle enables parrots to dramatically increase their bite force in relation to birds of similar size. Sustaita and Hertel (2010), for example, calculated falcon bite forces between 4 N in *Falco sparverius* and 14 N in *Falco mexicanus*. Parrots of approximately similar size generate estimated bite forces ranging from 39 N in *Conuropsis carolinensis* to 62 N in *Psittacus erithacus* (see Table 5). The highly dorsoventral nature of mEM's orientation enables the muscle to apply all of its force directly to closure of the jaw, which is advantageous for the seed-cracking dietary requirements of most parrots.

Quantitative Sampling

Overall, many of the strain profiles of the cranial bones of parrots and the falcon *Falco* appear to be generally similar (Fig. 4-13A). Median and peak strains are reported in Table 6. In isolation, extreme peak strains appear catastrophic in some elements; however, these singular peak strains do not relay information about surrounding elements, connected joint tissues, or artifacts of the modeling process. The median and peak values can be used to infer whether an element of the palate is highly strained by the forces acting on it during feeding or if the opposite is true. The palatine and pterygoid of *Falco* are both strained similarly to that of *Brotogeris* despite *Falco* being approximately 7 times heavier and possessing a head with 4 times as much volume. The truncated high end is most appreciable in the pterygoid subset of data. The palatine data also contains an

appreciable view of this truncated data, but overall it appears that the palatine more uniformly exhibits middle and lower end strains. The median values in the palatine and pterygoid of most taxa presented here are approaching the high end of the data. Martin (2000) and Curtis et al. (2011) noted that sustained levels of με above 3000 με could lead to bone remodeling and our median με, though on the higher end of our data, do not approach this level. Instead, the bulk of the με values reported here reside within the “Physiologic” (homeostasis) and “Overload” (increased modeling/remodeling) ranges described by Martin (2000). Curtis et al. (2013) noted that models with patent sutures “lead to a more consistent higher strain magnitude over the skull” (pg. 4). However, it is notable that the palatines of *Conuropsis* and *Deroptyus* approach this value. The pterygoid of *Psittacus* most closely approaches the high end of strain values but is followed closely by *Conuropsis*, *Deroptyus*, and *Nestor*.

The capability of parrots to propagate high strain throughout the palate regularly without detriment is important in the context of cranial kinesis. Constant, if not consistent, pulling and pushing and of the palatal elements in bouts of kinesis require the system to be able to withstand high strains and the potentially associated elastic deformations, without plastically deforming and causing the feeding apparatus to become irreparably damaged. *Falco* and *Brotogeris* (and to a lesser extent *Strigops*) are not subjected to the high-end strain of the other taxa presented here. Elastic deformation of the feeding apparatus in the style

of cranial kinesis may not play a significant role in the behavioral ecology of these animals. The diet of *Brotogeris* consists of nectar, fleshy (i.e. soft) fruits, and small seeds (0.85 mm diameter; Siqueira et al. 2015) and does not necessitate high strain inducing force generation within the palate as taxa with larger or harder dietary components require to access food items in hard shells and fruits (Pizo et al. 1995; Francisco et al. 2002; Ragusa-Netto 2004). *Strigops* με values in relation to food item toughness are comparable to *Brotogeris*, however; the leaves and berries which *Strigops* feeds on are highly fibrous and the bill, not the palate, is highly specialized to deal with the disparate requirements of its diet (Gray 1977; Kirk et al. 1993; Butler 2006; Froggatt and Gill 2016).

Falco, on the other hand, feeds on small mammals, reptiles, and other birds and does not generate either high bite forces or high degrees of cranial kinesis to feed; Hull (1991) reports approximately 3° of movement in *F. peregrinus* at the craniofacial hinge. The rigors of dispatching with prey are not concentrated in the feeding apparatus for *Falco*, rather they kill their prey using momentum, body mass, and their talons to knock prey out of the sky (for birds and bats) or to pin prey to the ground (non-volant mammals and reptiles) and then use their tomial teeth and neck muscles to break the necks of their prey. This may impart shear stress on the feeding apparatus, but forces about the neck were not applied to our model. Muscle forces that were applied in our models do not appear to communicate high strains to the skeletal elements of the palate in *Falco*.

Geometry and Bending Resistance of the Pterygoid

The pterygoid in kinetic taxa serves both as an attachment site for muscles and functions as a propulsive skeletal element of cranial kinesis in the skull. Axial loads on the pterygoid propel the bone, and thereby the entire palate, rostrocaudally at the same time that the pterygoid muscles are loading the bone orthogonally. The capability of the pterygoid to resist bending and shear is therefore extremely important to the mechanical environment of the palate and to the ecological fitness of the animal. In parrots this translates to a need to have the pterygoid retain a rigidity during rostrocaudal and mediolateral mobilization (by both the quadrate and palatine) while simultaneously resisting forces directed dorsoventrally and mediolaterally as a result of pterygoideus muscle (mPTd and mPTv) actions and attachments to the pterygoid.

Psittacus, *Nestor*, and *Strigops* have similar estimates of resistance to bending and torsion in all measurements of pterygoid geometry. Muscle forces of mPTd and mPTv decomposed to represent these loads (Fig. 4-12A and 12B) suggests that the pterygoid is relatively overbuilt in *Psittacus* compared to *Nestor* and, dorsoventrally, to *Strigops* as well. The graph of dorsoventral tension (Fig. 4-12B) supports this inference. *Psittacus* is optimally built to withstand compressive forces, but the dorsoventral data indicates that *Psittacus* is overbuilt in regard to withstanding bending forces oriented dorsoventrally. *Strigops* is similarly

optimal in regard to compressive forces but instead is underbuilt in resistance to dorsoventral tensile forces. *Nestor* and *Deroptyus* are both overbuilt to withstand compressive rostrocaudal and tensile dorsoventral forces; though both are closer to optimal in regard to tensile forces than they are compressive forces. *Conuropsis* is also overbuilt in regard to tensile forces but is nearly optimally built for withstanding compressive forces. This is similar to *Psittacus*, but to a much lesser degree in the tensile forces in particular. *Brotogeris* and *Falco* are underwhelming performers in resisting forces on the pterygoid. Because Hull (1991) showed that *Falco* possesses minimal kinetic capabilities we assume that it does not require a robust pterygoid for the purpose of resisting loads associated with cranial kinesis. The similarly low resistances in *Brotogeris* leads to inferences of weaker or lesser bouts of cranial kinesis in this small parakeet as well. The axial muscle loads in relation to axial bending are shown in Fig. 4-12A and 12B.

Each parrot taxon exhibits strengths and weaknesses in pterygoid CSA related to the resistance to bending when forces are isolated in specific directions. For instance, the strigopoid parrots appear to be weakly adapted to resisting purely dorsoventral and mediolateral forces compared to the psittacid parrots. Likewise, it appears that the New World parrots (*Brotogeris*, *Deroptyus*, and *Conuropsis*) better resist bending near the quadrate (caudally) whereas *Psittacus* better resists bending forces near the palatine (rostrally). These trends may be related either to diet or to familial relationships. More investigation is

required to determine the relationship between specific bending resistances in the pterygoid and phylogeny.

Trait Evolution

Phylogenetic trees from Hackett et al. (2008), Mayr (2010), Kirchman et al. (2012), and Prum et al. (2015) informed trees used to analyze continuous and discrete data in a phylogenetic context. The resulting trees show some similarities between parrots and falcons. The parrots *Nestor* and *Strigops* are unique in most regards from one another, the other parrots, and *Falco*. The strigopoid parrots exhibit character states that are proximate to one another in predicted muscle force. The strigopoid parrots are not more similar to *Falco*, however, and maintain a derived status from the outgroup as well. Measures of ellipticity as a character in *Nestor* are nearing those in *Falco* yet they remain derived from one another. *Strigops* is similar to *Falco* in median palate strain only. *Psittacus* traits are intermediate between the strigopoid parrots and the Neotropical parrots. The ellipticity trait in *Psittacus* is shared with the Neotropical parrot *Conuropsis* but is different from all other taxa. *Psittacus* predicted muscle force, on the other hand, presents as a character state that is shared with *Strigops* identically and both are proximate to *Nestor*'s character state. Median palate strain and median Z_{DV} are both character states uniquely exhibited by *Psittacus*.

Shape characteristics (I_{DV}, I_{ML}, Z_{DV}, Z_{ML}, CSA, I_{min}, I_{max}, Z_{min}, Z_{max}, and J) across the trees united the Neotropical parrots. Strigopoid parrots and *Psittacus* were at times similar, though not as tightly grouped as *Brotogeris*, *Deroptyus*, and *Conuropsis* were. It appears that a somewhat uniform, though differently sized, shape is prevalent in the pterygoids of Neotropical parrots, though the pterygoid appears to handle strains differentially, possibly influenced by size and muscle force; evidence of this can also be seen in Figs. 12, 14, and 17 as well as Tables 4 and 7.

Absolute muscle force (Fig. 4-21A) and absolute bite force (Fig. 4-21B) appear to recreate the graphs shown in Fig. 4-11A and 11B with a phylogenetic signal. Bite force standardized as the output of total force (BF/MF) shows an unexpected outcome (Fig. 4-22A). All parrots were expected to generate high bite forces in relation to the total muscle force produced by the cranial musculature once controlled for size (BF/SW; Fig. 4-21D). However, *Brotogeris*, the smallest parrot sampled here generated a higher than expected bite force per total force produced (Fig. 4-11C) and this caused the phylogenetic signal to exhibit *Brotogeris* occupying a highly derived position in the tree. All other taxa sampled in this study occupy comparable positions to one another based on squared branch lengths in this tree.

Conclusions

Parrots engage in a wide variety of diets employing a number of different feeding behaviors to do so. This is managed using largely similar cranial

morphologies across studied parrots. Falcons possess a cranial morphology that is more raptorial, though some morphological similarities can be observed. The biomechanical loading environments of these two families possess many similarities despite fundamentally different feeding behaviors. Previous studies (Bright et al 2016; Navalon et al. 2018), and shape data analyzed in the pterygoid here, indicate that the shape of the feeding apparatus does not reflect diet. However, we find that muscle orientation and increased bite forces generated by granivorous and folivorous parrots do appear to be related. We found that the performance of muscles in generating high bite forces is integral for parrot diet preference. Additionally, the bending resistance and associated propulsive kinematics of the pterygoid are important aspects of the parrot feeding apparatus. Whereas the shape of the feeding apparatus was not related to the diets of parrots, muscle parameters and kinematics of the palate appear to be indicative of the capabilities of parrots to access and utilize difficult food sources that are inaccessible to other birds.

Identifying key components of the biomechanical environment of the feeding apparatus of birds that lead to dietary niche partitioning and the mechanical foundation for cranial kinesis is integral in tracking the evolution of birds and the development of the feeding apparatus as a whole system. The methods and analyses described in this study are integral to discovering and understanding the underlying kinematic

biomechanical principles of feeding in not only birds, but also other non-mammalian tetrapods.

Table 4-1. Scanning and processing parameters and skull measurements of specimens included in this study.

Taxon	Specimen number	Scan resolution (μm)	Skull Length (mm)	Skull Width (mm)	Skull Volume (mm^3)	ImageJ Threshold (%)	No. of Tetrahedra
Falco peregrinus	KU 90085	125^3	64.53	36.56	8561.45	97.55	727501
Nestor notabilis	FMNH 289312	127^3	91.43	39.66	14006.09	99.31	537486
Strigops habroptila	FMNH 23529	127^3	79.58	47.26	23383.52	99.17	730652
Psittacus erithacus	MUVC AV042	63^3	66.24	34.69	11907.93	98.66	495239
Brotogeris chrysoptera	FMNH 330249	163^3	39.70	18.96	2135.98	99.79	566806
Conuropsis carolinensis	MCZ 342347	88^3	49.53	30.67	6463.45	99.16	1031150
Deroptyus accipitrinus	MUVC AV074	56.9^3	56.56	38.11	10332.33	99.31	1074531

Table 4-2. Muscle parameters used to estimate physiological cross sectional areas and jaw muscle force used in finite element models. Muscle attachment areas are reported as proximal (P) and distal (D) attachments.

Parameter	Taxon	mAMES	mAMEM	mAMEP	mAMP	mPSTs	mPSTp	mPTd	mPTv	mPPT	mEM	mPM	mDM
Fiber Length (mm)	*Falco*	16.3		9.7	3.1	10.2	7.0	7.3	10.6	4.4			6.8
	Nestor	19.4	11.9	11.3	3.7	11.9		9.7	8.5	12.1	17.6		9.49
	Strigops	23.4	15.1	12.4	5.9	16.6		15.3	13.5	14.1	30.0		13.5
	Psittacus	15.9		15.0	3.5	13.7		12.1	9.7	10.3	16.9	20.5	6.9
	Brotegeris	7.6		8.8	1.9	7.7		6.7	5.6	5.9	9.9		3.8
	Conuropsis	9.6		9.7	1.6	9.5		8.4	6.7	9.8	12.1	8.3	5.4
	Deroptyus	12.3		13.1	2.1	11.8		9.9	8.6	10.1	17.1	10.9	10.1
Pennation Angle (θ)	*Falco*	20		20	0	7	2.57	14.25	3.5	0			5.25
	Nestor	20	0	20	0	6.66		14.54	4.09	0	2.57	0	5.52
	Strigops	20	0	20	0	6.66		14.54	4.09	0	2.57	0	5.52
	Psittacus	20		20	0	6.66		14.54	4.09	0	2.57	0	5.52
	Brotogeris	20		20	0	6.66		14.54	4.09	0	2.57	0	5.52
	Conuropsis	20		20	0	6.66		14.54	4.09	0	2.57	0	5.52
	Deroptyus	20		20	0	6.66		14.54	4.09	0	2.57	0	5.52

Parameter	Taxon	mAMES	mAMEM	mAMEP	mAMP	mPSTs	mPSTp	mPTd	mPTv	mPPT	mEM	mPM	mDM
Muscle Attachment Area (mm^2)	*Falco*	P:132.08 D: 22.26		P: 15.71 D: 13.82	P: 9.47 D: 11.07	P: 6.96 D: 9.21	P: 10.83 D: 14.77	P: 59.65 D: 27.38	P: 62.34 D: 78.69	P: 6.27 D: 15.52			P: 10.63 D: 21.45
	Nestor	P: 31.08 D: 4.25	P: 3.79 D: 64.99	P: 8.12 D: 16.81	P: 18.57 D: 7.62	P: 27.43 D: 8.86		P: 164.89 D: 91.53	P: 69.50 D: 189.98	P: 23.34 D: 6.76	P: 45.76 D: 12.40		P: 144.62 D: 27.59
	Strigops	P: 156.74 D: 36.80	P: 14.06 D: 167.33	P: 28.11 D: 59.21	P: 40.52 D: 22.70	P: 39.14 D: 29.65		P: 141.19 D: 82.45	P: 87.78 D: 198.27	P: 52.02 D: 28.25	P: 59.49 D: 25.77		P: 140.50 D: 36.03
	Psittacus	P:15.38 D: 96.35		P: 52.13 D: 15.10	P: 16.29 D: 14.46	P: 15.09 D: 12.75		P: 192.26 D: 102.67	P: 46.71 D: 178.65	P: 32.62 D: 15.53	P: 72.94 D: 21.12	P: 11.56 D: 76.21	P: 155.53 D: 22.39
	Brotogeris	P: 11.24 D: 40.14		P: 14.00 D: 9.94	P: 3.28 D: 4.28	P: 6.67 D: 3.18		P: 32.14 D: 18.59	P: 21.39 D: 34.25	P: 7.00 D: 3.45	P: 16.10 D: 3.11		P: 20.41 D: 8.93
	Conuropsis	P: 15.52 D: 56.17		P: 30.41 D: 10.34	P: 4.88 D: 6.42	P: 9.22 D: 5.50		P: 83.16 D: 76.15	P: 38.55 D: 107.48	P: 18.43 D: 5.49	P: 2.45 D: 5.79	P: 29.86 D: 35.51	P: 63.89 D: 24.06
	Deroptyus	P: 29.11 D: 109.99		P: 80.02 D: 16.08	P: 7.95 D: 6.48	P: 18.03 D: 5.94		P: 131.67 D: 92.79	P: 79.85 D: 159.65	P: 16.94 D: 10.88	P: 26.62 D: 5.88	P: 12.76 D: 33.01	P: 37.93 D: 22.81
Muscle Volume (mm^3)	*Falco*	1710.1		214.4	47.8	122.9	133.8	467.5	1121.4	69.7			584.9
	Nestor	454.3	505.8	206.3	71.9	308.3		1831.3	1592.6	258.7	723.6		1117.1
	Strigops	2990.3	1735.8	793.6	277.1	856.1		2541.9	2820.4	836.4	1866.8		1670.9
	Psittacus	1204.5		716.6	79.2	286.0		2606.3	1532.6	392.6	1139.6	1203.4	817.03
	Brotogeris	277.7		157.2	11.3	55.7		251.6	232.4	45.7	129.9		81.9
	Conuropsis	487.3		284.6	13.1	103.4		1000.1	702.5	165.7	285.5	404.9	341.1
	Deroptyus	1207.5		861.1	22.7	202.8		1650.6	1522.1	209.0	383.9	362.7	458.6
Force (N)	*Falco*	19.74		5.21	2.99	2.25	5.49	9.24	19.28	1.36			2.76
	Nestor	6.86	11.11	5.49	5.71	7.44		54.52	55.17	6.25	12.29		35.31
	Strigops	33.62	34.48	19.06	14.03	15.43		43.07	54.29	17.79	18.66		32.12
	Psittacus	21.17		13.41	6.90	6.20		63.11	47.38	11.38	19.99	17.59	35.37
	Brotogeris	10.23		5.04	1.69	2.15		10.92	12.37	2.30	3.94		6.39
	Conuropsis	14.26		8.24	2.52	3.25		34.68	31.48	5.09	7.05	14.69	18.99
	Deroptyus	27.58		18.59	3.24	5.11		48.64	52.73	6.21	6.74	9.94	13.46

Table 4-3. Characters measured and used in phylogenetic tree construction and ancestral state analysis. Thirty-three characters were used in reconstructing ancestral states and phylogenetic relationships of 6 parrot and one falcon. Squared length refers to the overall branch squared-length of continuous characters. Rate of change and - log L (- log likelihood) describe the rate of evolution and probability of change, respectively, in discrete character analyses. Greater - log L indicate lower probabilities of change.

Character	Type of Variable	Element Measured	Source	Squared Length	Rate of Change	- log L
Median Strain-Pterygoid	Continuous	Pterygoid	FEM	1.3591		
Pterygoid angle with palatobasal in Z plane (°)	Continuous	Pterygoid	FEM	61.6616		
Pterygoid angle with palatobasal in Y plane (°)	Continuous	Pterygoid	FEM	187.9836		
Median Imin	Continuous	Pterygoid	CT Scan	0.0096		
Median IDV	Continuous	Pterygoid	CT Scan	0.0248		
Median IRL	Continuous	Pterygoid	CT Scan	0.0065		
Median Imax	Continuous	Pterygoid	CT Scan	0.0160		
Median Zmin	Continuous	Pterygoid	CT Scan	0.0176		
Median ZDV	Continuous	Pterygoid	CT Scan	0.0266		
Median Zmax	Continuous	Pterygoid	CT Scan	0.0188		
Median ZRL	Continuous	Pterygoid	CT Scan	0.0086		
Median CSA	Continuous	Pterygoid	CT Scan	0.3178		
Median Ellipticity	Continuous	Pterygoid	CT Scan	1.5001		
Polar Moment (J)	Continuous	Pterygoid	CT Scan	0.0473		
Median Strain-Quadrate	Continuous	Quadrate	FEM	0.2209		
Median Strain-Palatine	Continuous	Palatine	FEM	2.1383		
Palate Strain	Continuous	Palate	FEM	4.3169E5		
Skull volume (mm^3)	Continuous	Skull	FEM	9.2222E7		
Skull Length (mm)	Continuous	Skull	CT Scan	389.4974		
Skull Width (mm)	Continuous	Skull	CT Scan	164.7204		
Total Muscle Force (N)	Continuous	Muscles	FEM	73806.4196		

Bite Force (N)	Continuous	Muscles	FEM	3660.8361		
Bite Force/Total Muscle Force	Continuous	Muscles	FEM	0.0585		
Muscle Force/Skull Volume	Continuous	Muscles/ Skull	FEM	0.0002		
Relative Bite Force	Continuous	Muscles/ Skull	FEM	1.3879		
Relative Muscle Force	Continuous	Muscles/ Skull	FEM	28.9189		
Body Mass (g)	Continuous	Entire Body	Literature	2.5952E6		
Main Diet	Discrete	Ecology	Literature		0.1251	10.9129
Primary Habitat	Discrete	Ecology	Literature		20	7.6903
Presence of mAMEM	Discrete	Muscle	Observation and Literature		0.1081	3.6851
Presence of mPM	Discrete	Muscle	Observation and Literature		0.2418	4.4596
Presence of mEM	Discrete	Muscle	Observation and Literature		0.0559	2.8599
Tomial Tooth Present	Discrete	Skull	Observation and Literature		0.1646	4.0949
Presence of Suborbital Arch	Discrete	Skull	Observation and Literature		17.9492	4.8520

Table 4-4. Median geometric properties of the pterygoid bones of sampled taxa.

Taxon	RC Pterygoid Angle (°)	DV Pterygoid Angle (°)	I_{DV} (mm^4)	I_{ML} (mm^4)	J (mm^4)	Z_{DV} (mm^3)	Z_{ML} (mm^3)	CSA (mm^2)	Median ellipticity
Falco	46.53	35.49	0.063	0.081	0.136	0.114	0.138	0.705	0.906
Nestor	36.52	31.22	0.114	0.225	0.318	0.167	0.238	1.149	0.553
Strigops	41.94	38.05	0.284	0.221	0.504	0.348	0.283	1.744	1.353
Psittacus	41.28	46.33	0.235	0.115	0.374	0.265	0.198	0.977	2.106
Brotogeris	44.29	50.41	0.023	0.03	0.051	0.058	0.064	0.54	0.724
Conuropsis	52.46	48.19	0.06	0.029	0.088	0.104	0.074	0.565	2.057
Deroptyus	45.04	33.22	0.045	0.068	0.109	0.097	0.122	0.662	0.821

Table 4-5. Bite forces, body mass, and relative bite force of taxa discussed in this study. Data for *Falco peregrinus* and all parrots are generated in our study. Data for *F. sparverius*, *F. columbarius*, and *F. mexicanus* are from Sustaita and Hertel (2010) male specimens and *Myiopsitta monachus* from Carril et al. (2015) serve as comparisons. Relative bite forces are calculated by dividing bite force by skull width (BF/SW). Skull width is reported in Table 1. Body masses for *F. peregrinus* and all parrots were gathered from Dunning (2007).

Taxon	Bite Force (N)	Mean Body Mass (g)	Relative Bite Force (this study only)
Falco peregrinus	9.90	611	0.271
F. sparverius	3.99	108.9	
F. columbarius	4.17	138	
F. mexicanus	13.79	503.7	
Nestor notabilis	27.16	956	0.685
Strigops habroptila	101.31	2000	2.144
Psittacus erithacus	61.78	333	1.781
Brotogeris chrysoptera	21.15	54.5	1.116
Conuropsis carolinensis	39.08	100	1.274
Deroptyus accipitrinus	61.03	246	1.601
Myiopsitta monachus	16.74	120	

Table 4-6. Median and peak strains of individual bones of the palate.

Taxon	Bone	Peak Microstrain (με)	Median Microstrain (με)
Falco	Palatine	1259.61	221.98
Falco	Pterygoid	1500.55	341.69
Falco	Quadrate	60126.05	524.15
Nestor	Palatine	15413.37	1275.91
Nestor	Pterygoid	7191.14	1076.24
Nestor	Quadrate	41620.97	361.07
Strigops	Palatine	8561.51	409.89
Strigops	Pterygoid	4630.51	525.42
Strigops	Quadrate	67979.49	394.012
Psittacus	Palatine	22821.54	1107.25
Psittacus	Pterygoid	12988.93	1710.77
Psittacus	Quadrate	15180.61	462.48
Brotogeris	Palatine	2031.39	200.43
Brotogeris	Pterygoid	2804.33	249.23
Brotogeris	Quadrate	7423.55	207.54
Conuropsis	Palatine	11228.57	1672.85
Conuropsis	Pterygoid	9719.81	1351.68
Conuropsis	Quadrate	83184.15	471.69
Deroptyus	Palatine	8598.16	1489.44
Deroptyus	Pterygoid	13780.03	1236.72
Deroptyus	Quadrate	34330.33	384.58

Table 4-7. Discrete character states used to analyze phylogenetic trees using maximum likelihood ancestral state reconstructions. Primary diet and habitat are gathered from the literature. Other characters are observed from skulls and the literature.

Taxon/Character	Main Diet	Primary Habitat	Presence of mAMEM	Presence of mPM	Presence of mEM	Presence of Tomial Tooth	Presence of Suborbital Arch
Available Character States	0 – Carnivory 1 – Granivory 2 – Omnivory 3 – Nectarivory 4 – Folivory	0 – Jungle or Rainforest 1 – Montane, Cliff, or Man-made Structures 2 – Subtropical Deciduous or Laurel forest	0 – Present 1 – Absent	0 – Absent 1 – Present	0 – Absent 1 – Present	0 – Present 1 – Absent	0 – Absent 1 – Present
Falco peregrinus	0	1	0	0	0	0	0
Nestor notabilis	2	1	0	0	1	1	0
Strigops habroptila	4	2	0	0	1	1	1
Psittacus erithacus	1	0	1	1	1	1	0
Brotogeris chrysopterus	3	0	1	0	1	0	0
Conuropsis carolinensis	1	2	1	1	1	0	1
Deroptyus accipitrinus	1	0	1	1	1	0	1

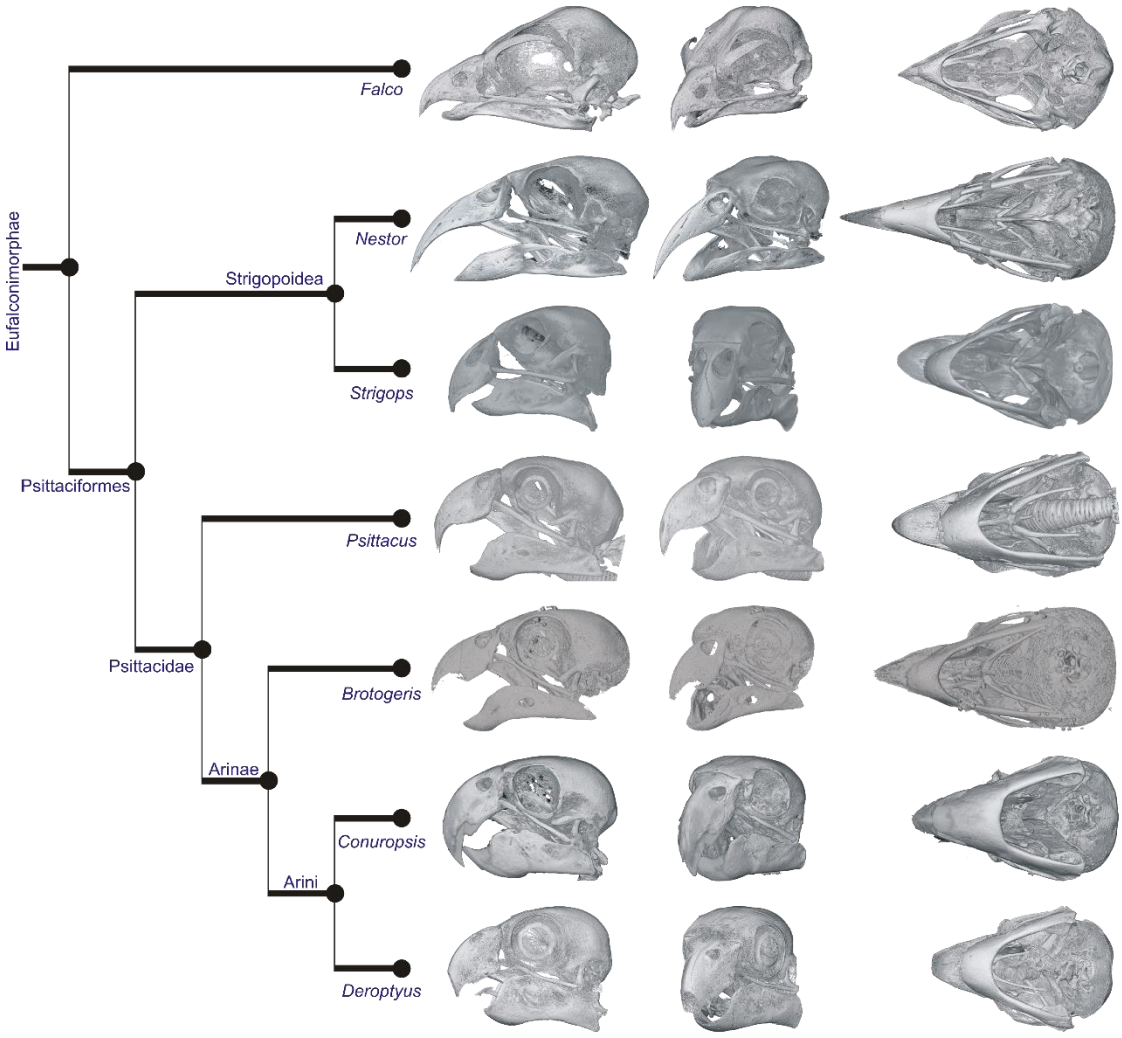

Figure 4-1. Phylogenetic relationships of parrot and falcon species used in this study. The phylogenetic tree used in this study was built using Hackett et al. (2008), Mayr (2010), Kirchman et al. (2012), and Prum et al. (2015) as base models. Parrot skulls are characteristically shaped; possessing a strongly decurved rostrum and rectangular overall skull shape. Parrots also possess dorsoventrally tall palatine shelves that are easily seen in all views, particularly in ventral (right) and left lateral (left) views.

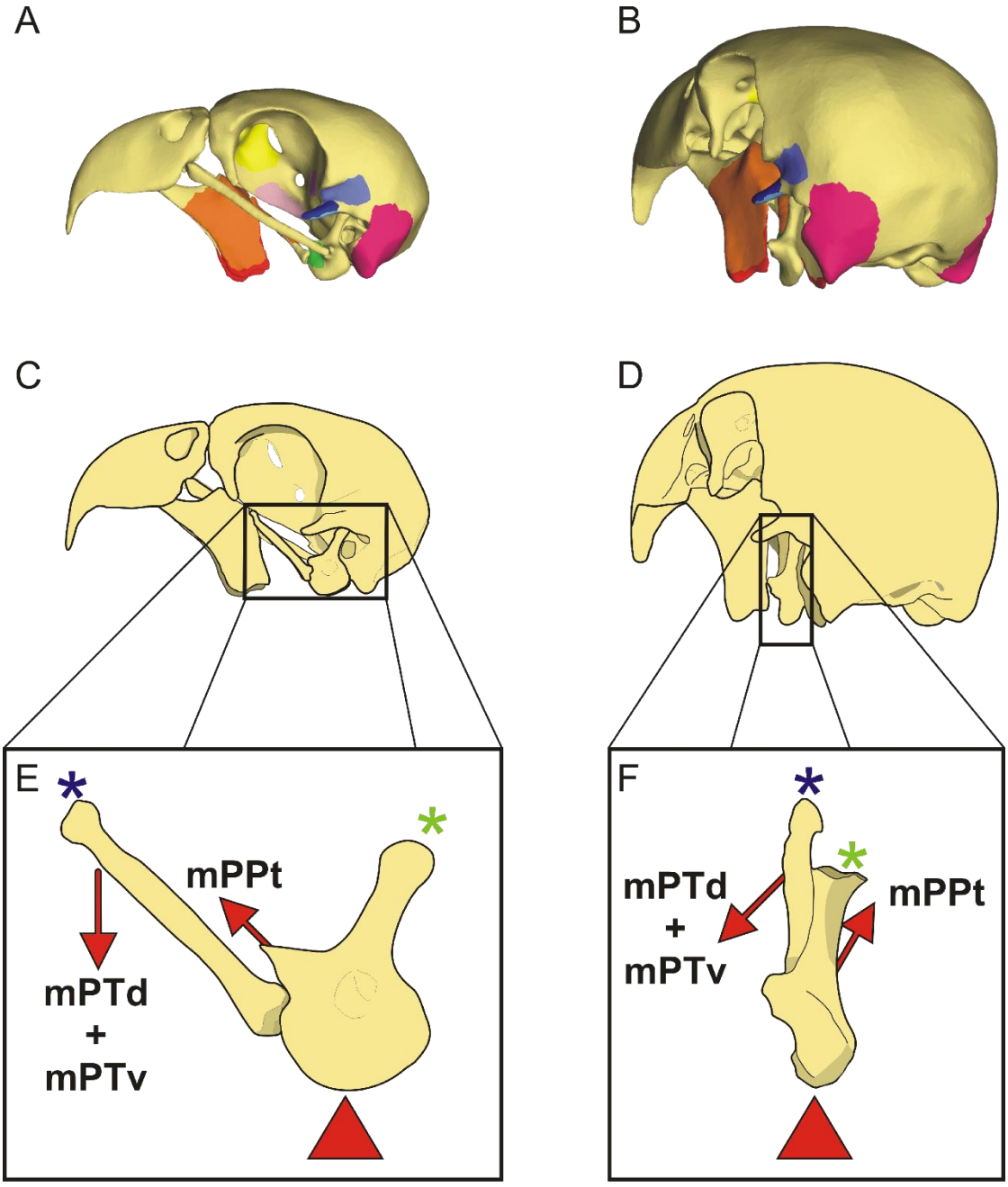

Figure 4-2. 3D lever analyses of the pterygoid bone. **(A)** Left lateral view and **(B)** Oblique caudal view of Psittacus erithacus model. **(C)** Left lateral line and **(D)** oblique caudal drawings of the skull with the jugal removed. **(E)** Left lateral and **(F)** oblique caudal views of the quadrate and pterygoid. Arrows indicate direction of force on the pterygoid and quadrate. Asterisks (*) indicate joints which the pterygoid and quadrate rotate about during cranial kinesis. The triangle at the base of the quadrate is the jaw joint with the mandible and acts as the fulcrum in this system.

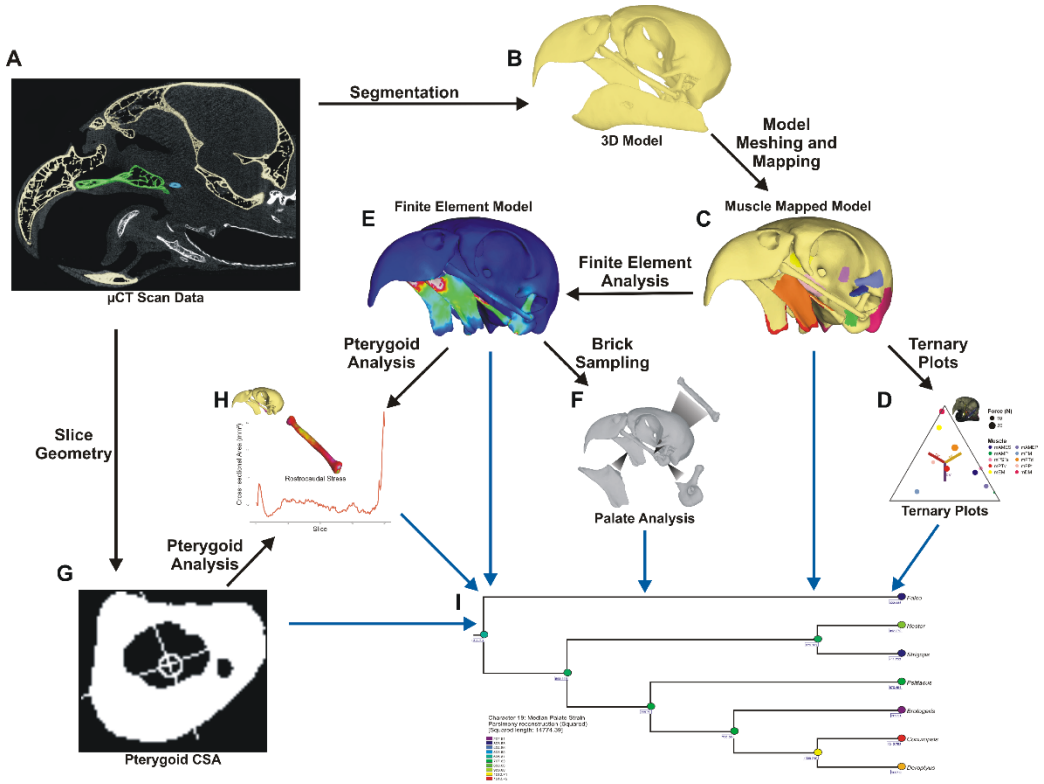

Figure 4-3. Steps in creating models and generating data analyzed and discussed in this study. **(A)** All data is generated from microcomputed tomography (μCT) scans of deceased individuals and/or dry skulls. **(B)** Scans are segmented to retain joints and models are comprised of individual elements assembled, articulated, and smoothed for finite element modeling (FEM) in Geomagic. **(C)** Models are then meshed and muscle attachments are assigned as brick properties to the meshed FEMs. The muscle attachment sites are analyzed to determine their area and centroid coordinates and muscle orientations are calculated from these data. Muscle forces are estimated using physiological cross-sectional areas (PCSA), fascicle length, and muscle volume. **(D)** Muscle forces and orientations are reduced to point resultants and plotted in ternary space to analyze orientation relationships among taxa. **(E)** Finite element analyses (FEA) are conducted on finished FEMs. **(F)** Further analyses are conducted by sampling individual elements of the palate. **(G)** The pterygoids are isolated in the CT and μCT scans and oriented orthogonally to the screen. **(H)** After thresholding in ImageJ pterygoids were processed using Slice Geometry in BoneJ to determine cross-sectional area (CSA) and were analyzed in coordination with FEA data gathered from the pterygoid. **(I)** All generated data is used to inform phylogenetic relationships between taxa sampled in this study. Continuous and discrete characters were analyzed for rates of evolution and ancestral reconstructions.

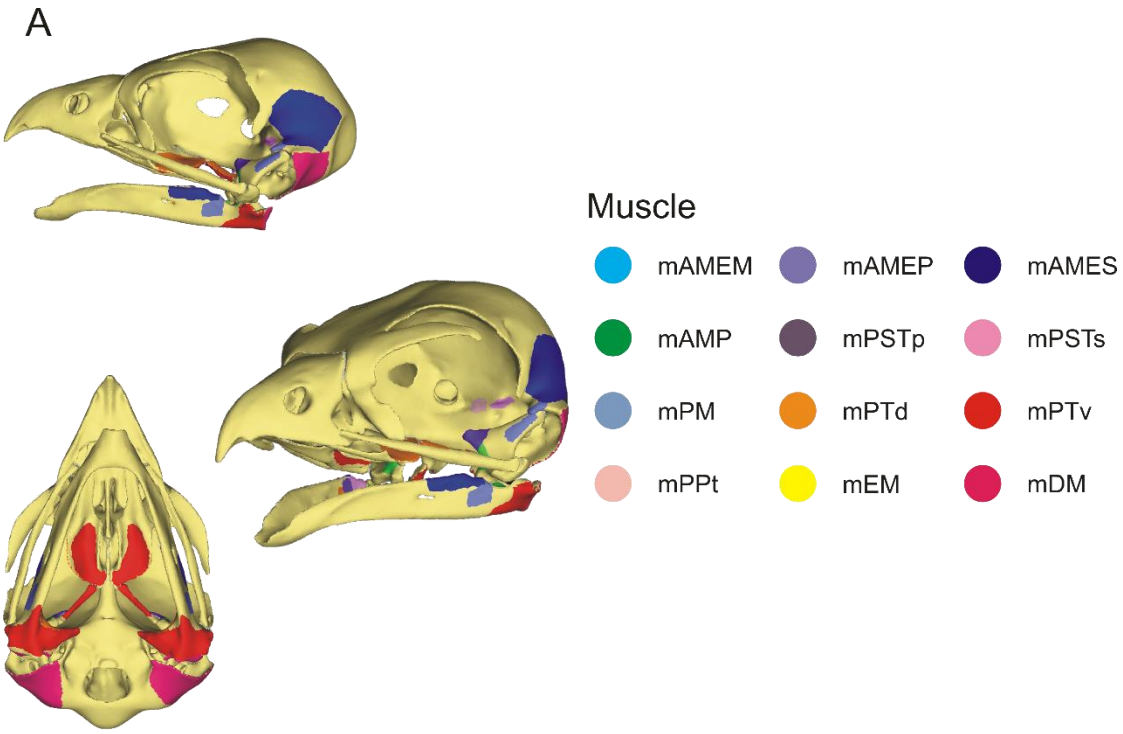

Figure 4-4. Left lateral (top), oblique (middle), and ventral (bottom) views of muscle attachments. **(A)** *Falco peregrinus* model. Muscles are mapped onto the bony morphology. Muscle abbreviations are as in Methods.

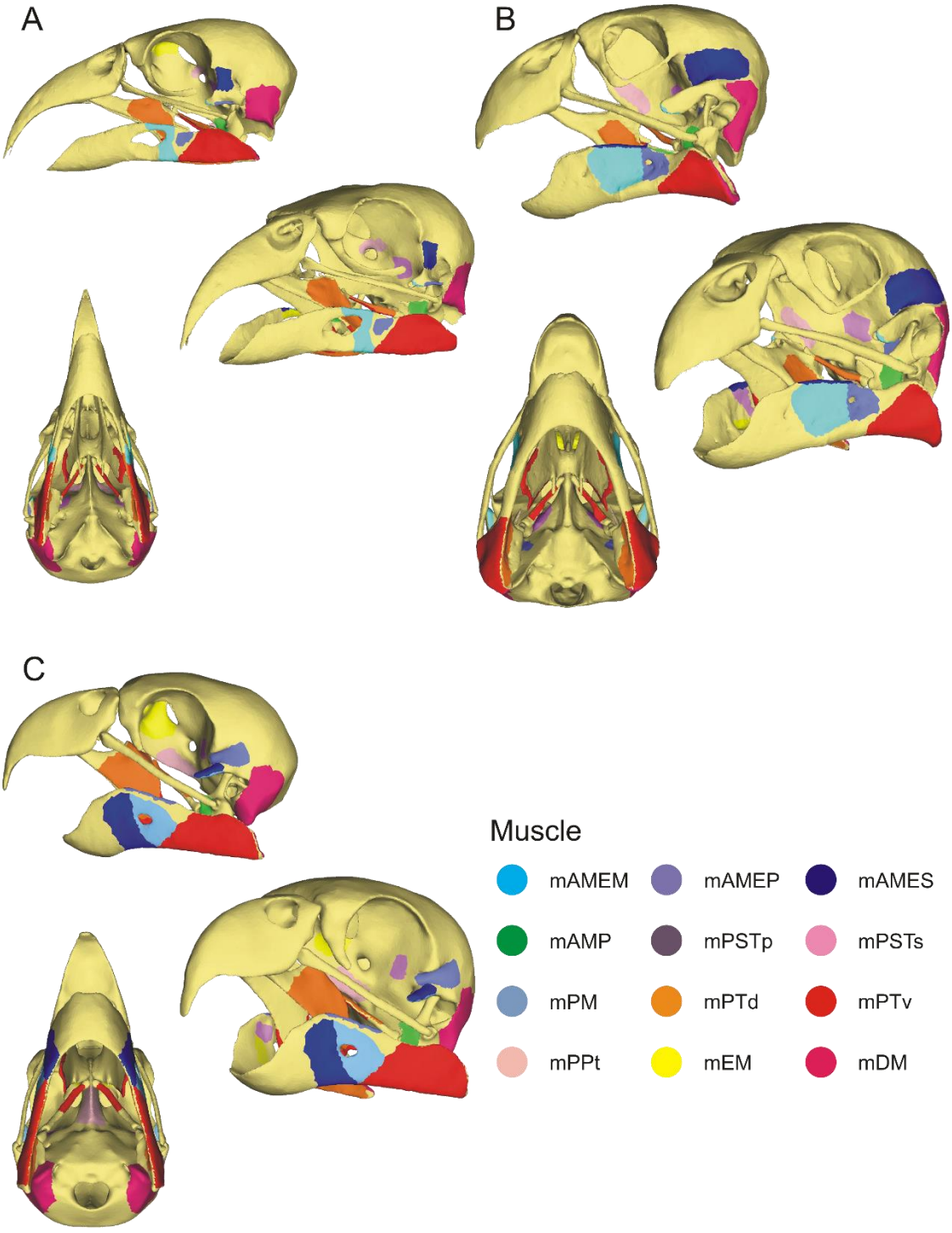

Figure 4-5. Left lateral (top), oblique (middle), and ventral (bottom) views of muscle attachments. **(A)** *Nestor notabilis* model. **(B)** *Strigops habroptila* model. **(C)** *Psittacus erithacus* model. Muscles are mapped onto the bony morphology. Muscle abbreviations are as in Methods.

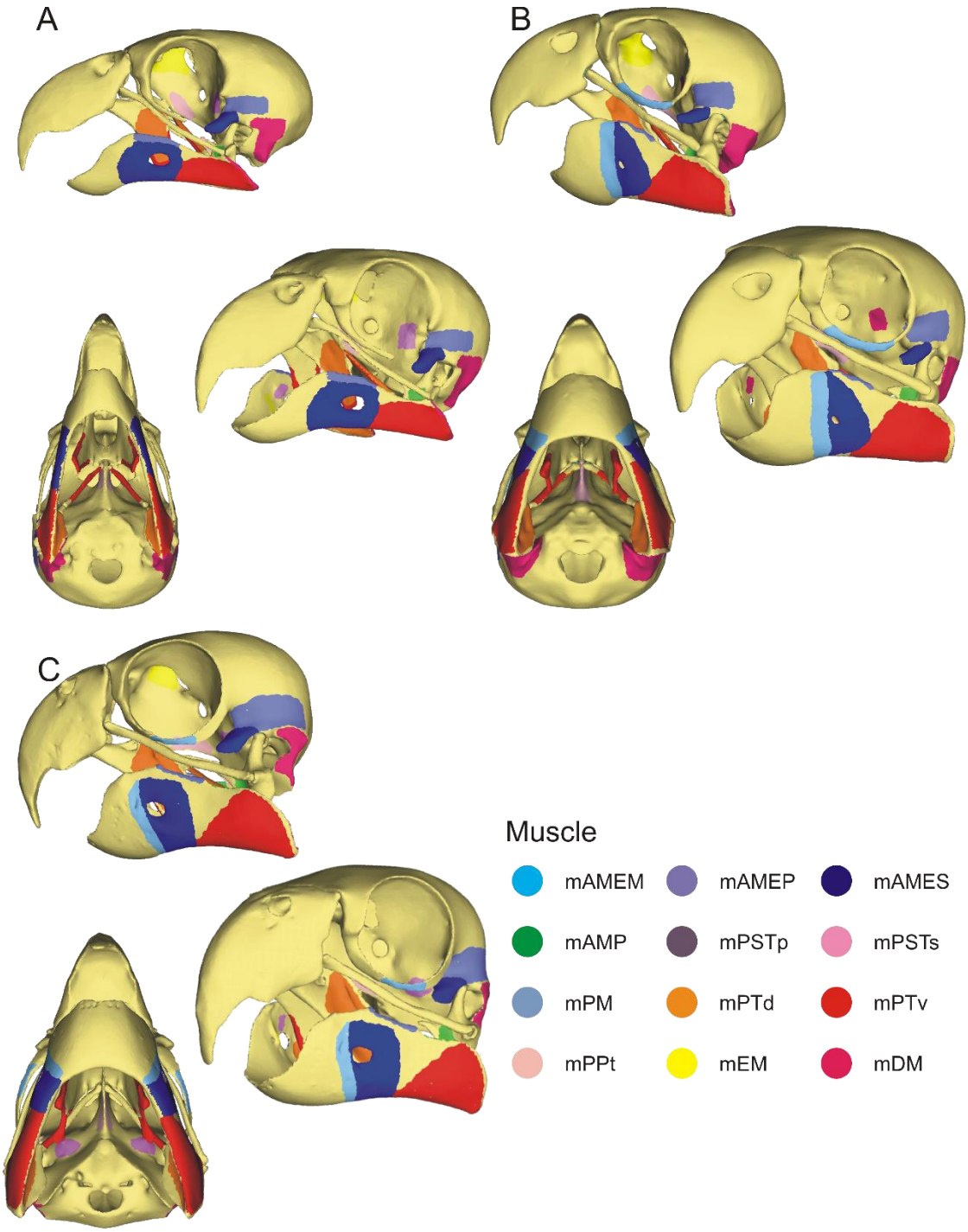

Figure 4-6. Left lateral (top), oblique (middle), and ventral (bottom) views of muscle attachments. **(A)** *Brotogeris chrysopterus* model. **(B)** *Conuropsis carolinensis* model. **(C)** *Deroptyus accipitrinus* model. Muscles are mapped onto the bony morphology. Muscle abbreviations are as in Methods.

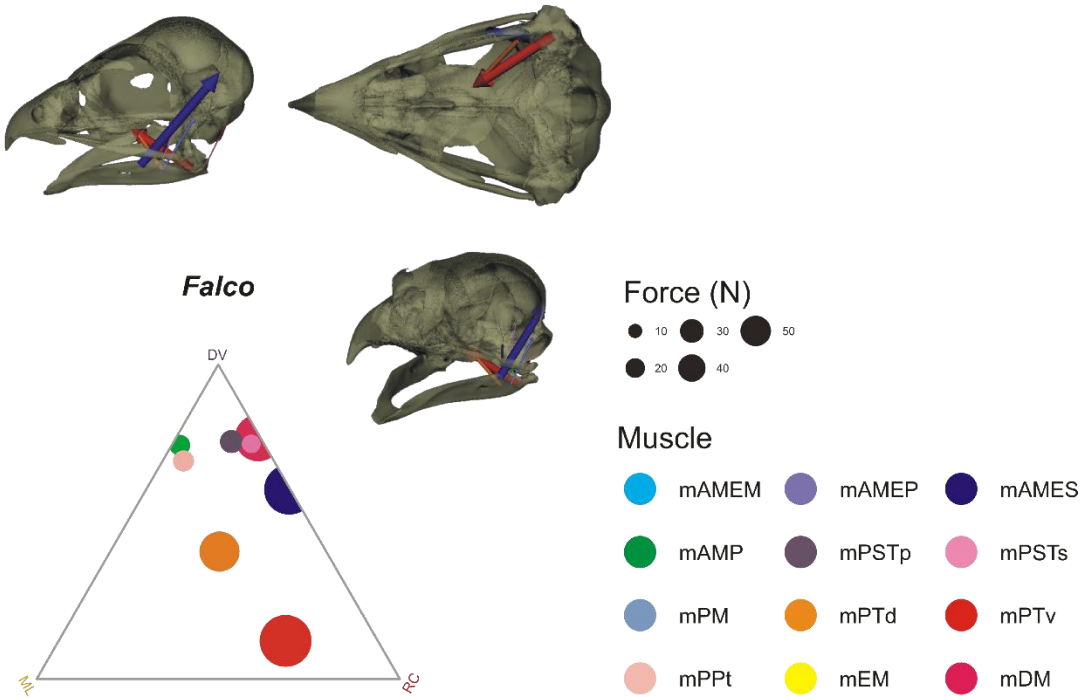

Figure 4-7. Ternary plot of muscle orientation with muscle force of each muscle indicated by point size for a single taxon. *Falco peregrinus* is presented here in left lateral (top left), ventral (top right), and left oblique (bottom) views. The muscles of *F. peregrinus* are largely dorsoventral, and so cluster near the top of the ternary plot. mPTv exhibits large rostrocaudal components whereas mPTd exhibits nearly equal resultant components in all three axes.

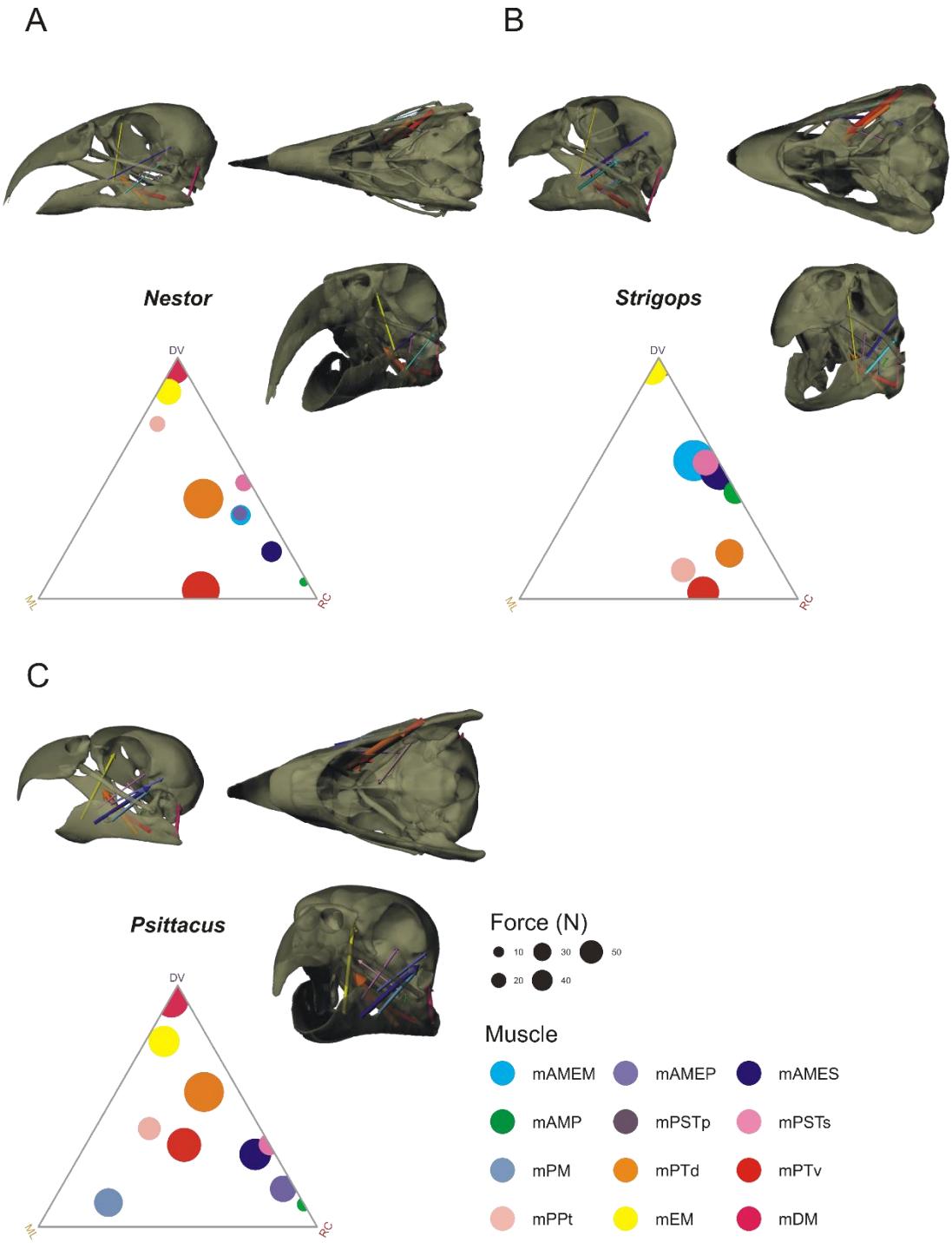

Figure 4-8. Ternary plot of muscle orientation with muscle force of each muscle indicated by point size for single tax. **(A)** *Nestor notabilis* in left lateral (top left), ventral (top right), and left oblique (bottom) views. **(B)** *Strigops habroptila* in left lateral (top left), ventral (top right), and left oblique (bottom) views. **(C)** *Psittacus erithacus* in left lateral (top left), ventral (top right), and left oblique (bottom) views. The muscles of *N. notabilis* and *S. habroptila* are largely rostrocaudal, and so cluster near the bottom right of the ternary plot. *Psittacus erithacus* possesses much more homogenous muscle resultants.

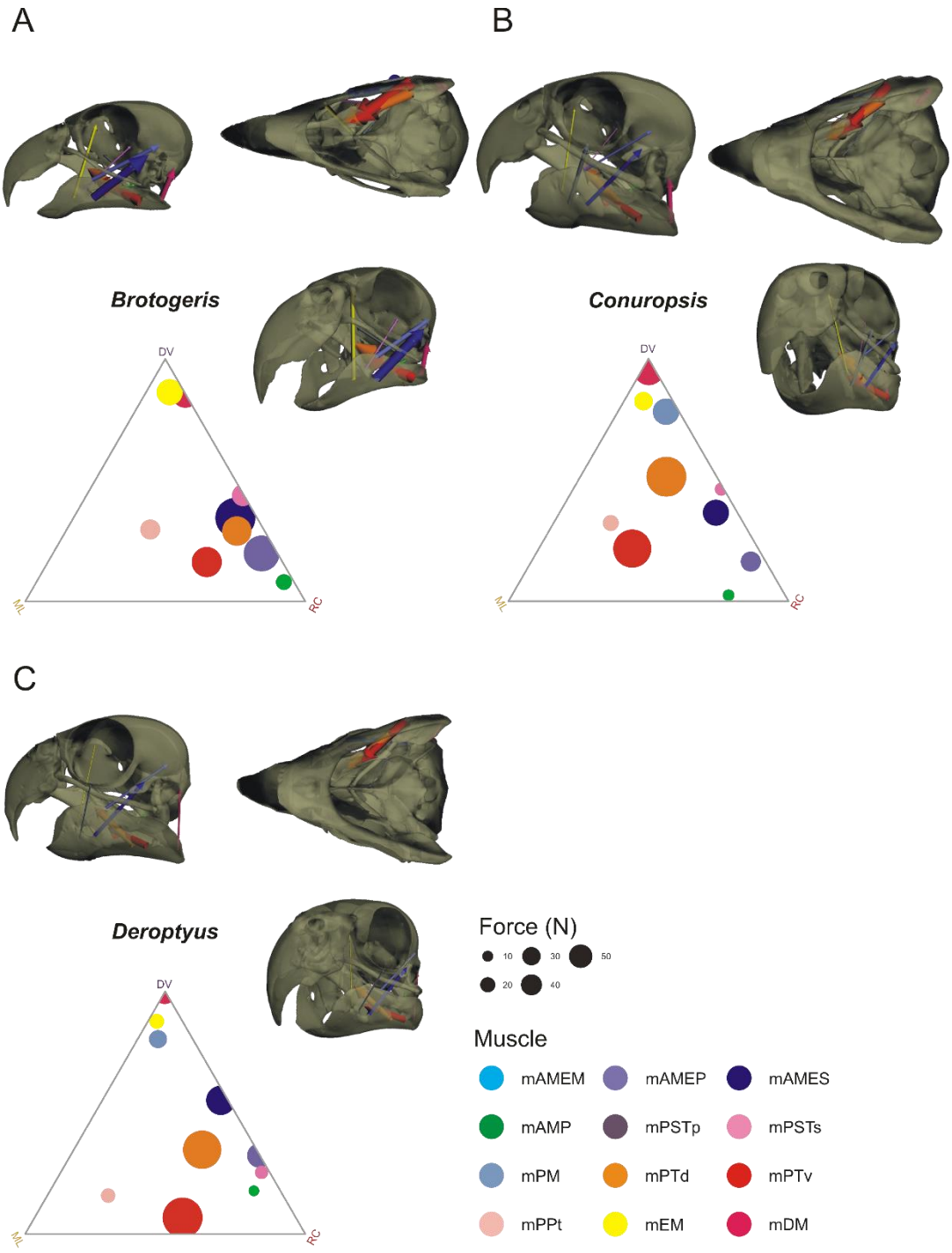

Figure 4-9. Ternary plot of muscle orientation with muscle force of each muscle indicated by point size for a single taxon. **(A)** *Brotogeris chrysopterus* in left lateral (top left), ventral (top right), and left oblique (bottom) views. **(B)** *Conuropsis carolinensis* in left lateral (top left), ventral (top right), and left oblique (bottom) views. **(C)** *Deroptyus accipitrinus* in left lateral (top left), ventral (top right), and left oblique (bottom) views. *Brotogeris* possesses largely rostrocaudal muscles whereas *Conuropsis* and *Deroptyus* possess appreciably homogenous muscle resultants.

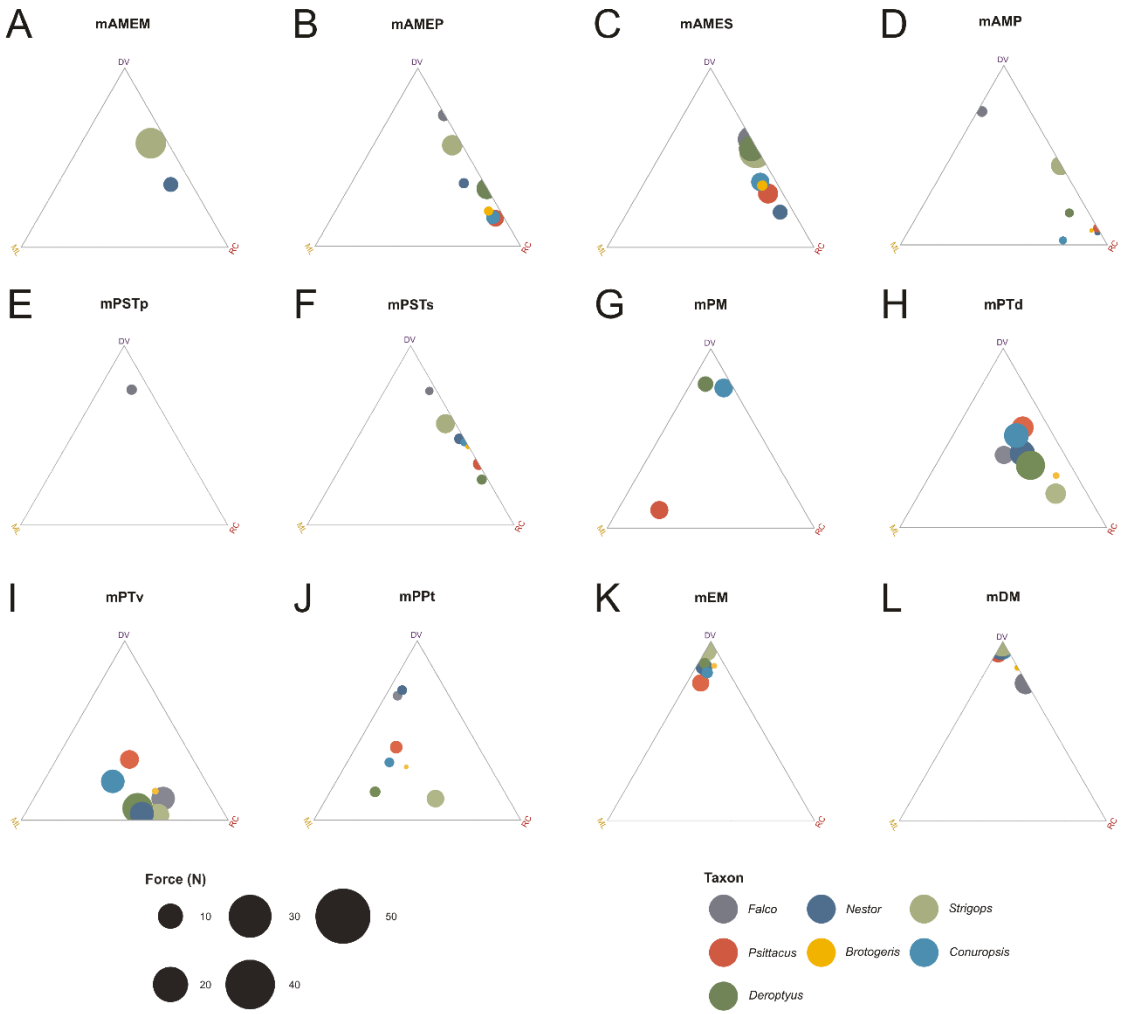

Figure 4-10. Ternary plots of muscle orientation with muscle force of each muscle indicated by point size. Temporal **(A – G)**, pterygoideus **(H – J)**, and depressor (**L)** muscle orientation and estimated forces displayed in ternary space. Side average orientations of temporal muscles are displayed with their estimated muscle forces indicated by point size.

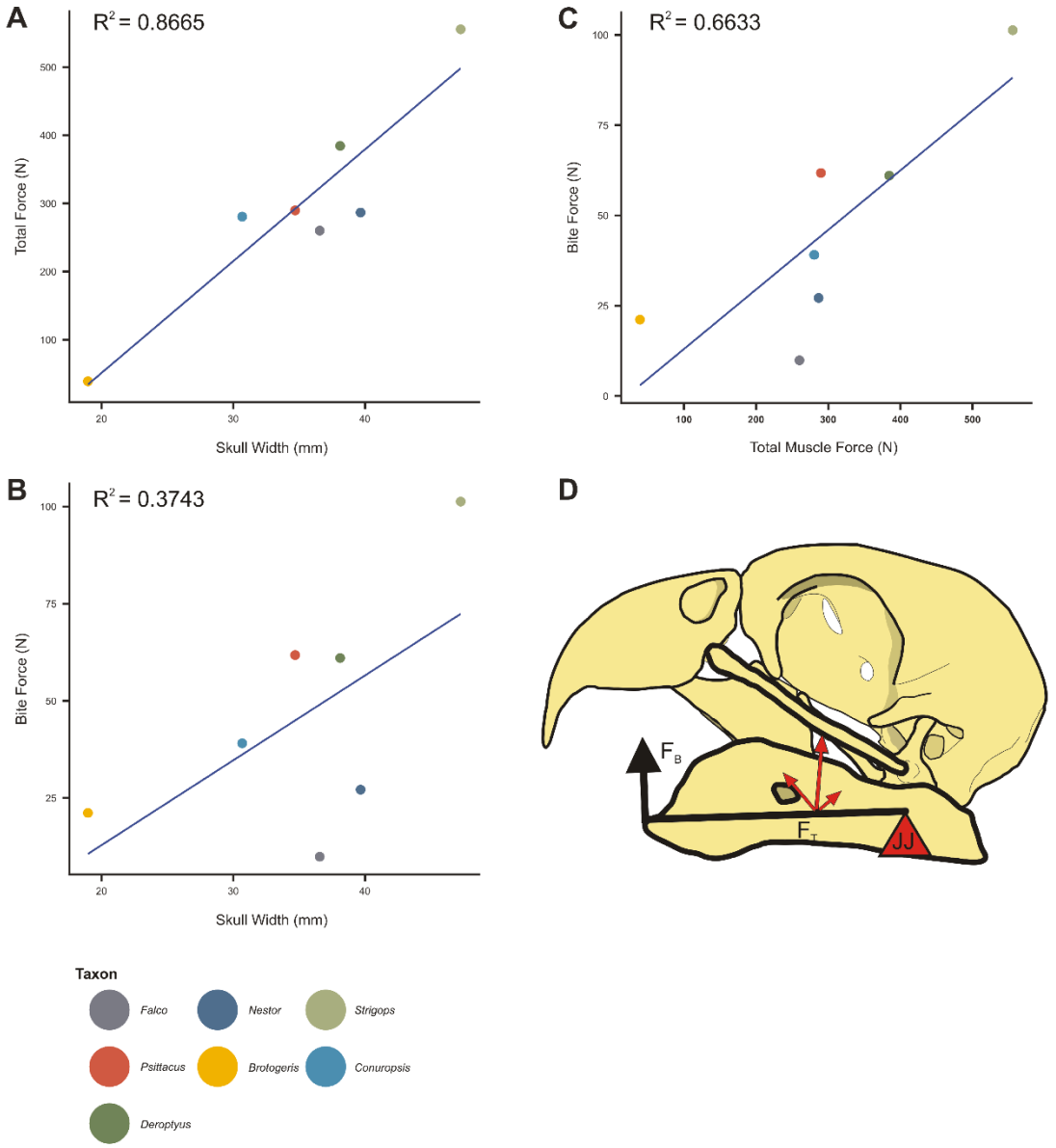

Figure 4-11. Relative muscle forces predicted by skull width and bite force generation plotted against total force production. **(A)** Total muscle force produced by sampled taxa relative to skull width. **(B)**. Bite force generated by sampled taxa relative to skull width. **(C)** Bite force generated by sampled taxa relative to total force produced. Muscle forces differing from the predicted value are either higher (above) or lower (below) than the regression line which represents a linear model in each graph of the effects of x on y. **(D)** A graphical representation of mechanical advantage of the 3rd class lever system of the jaws using *Psittacus erithacus* as an example. Using the jaw joint (JJ) as a fulcrum, total muscle force (F_T) acts on the lever between the load, producing bite force (F_B) and the fulcrum.

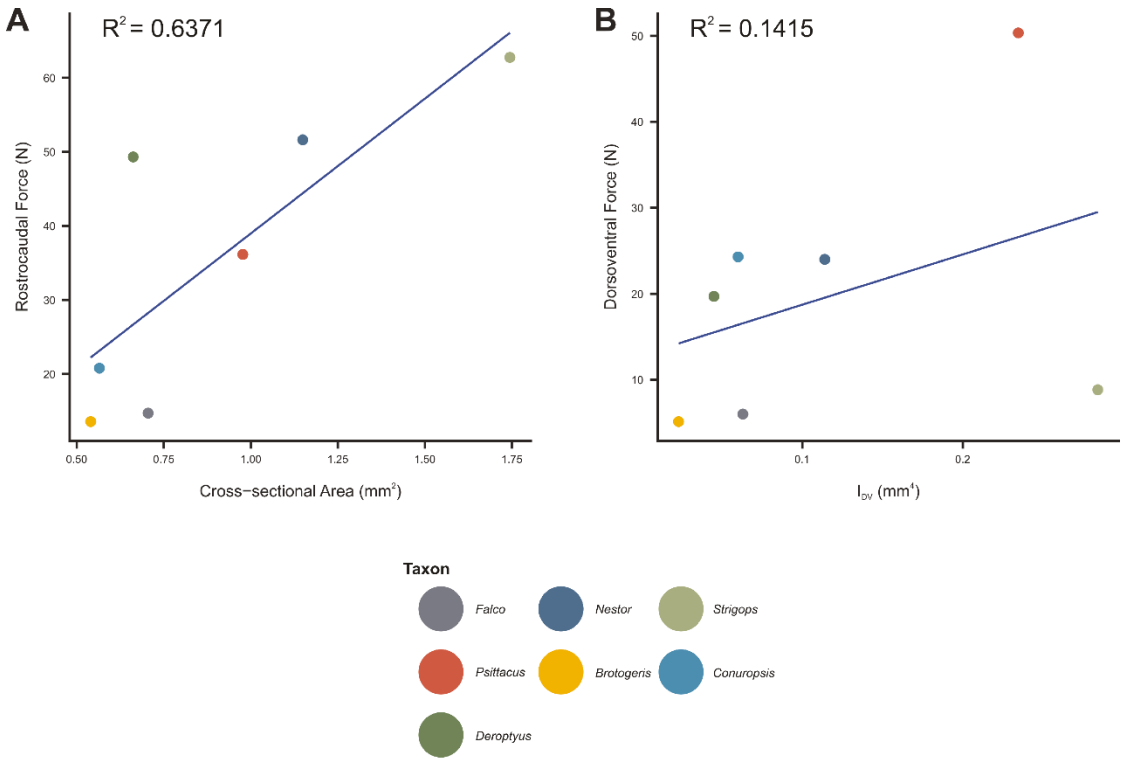

Figure 4-12. Plots of components of pterygoideus muscle forces acting on the pterygoid and the resistance to bending in the directions of the component forces. **(A)** Rostrocaudal force (N) plotted against CSA of the pterygoid. **(B) D**orsoventral force (N) plotted against I_{DV}. Taxa with values in proximity to the regression line are considered to be possess pterygoids adequately built for resisting pterygoideus muscle forces. Taxon values above the regression lines are considered to be overbuilt (i.e. possess higher relative bending resistances than muscle forces). Taxon values below the regression line are considered to be underbuilt (i.e. possess lower relative bending resistances than muscle forces).

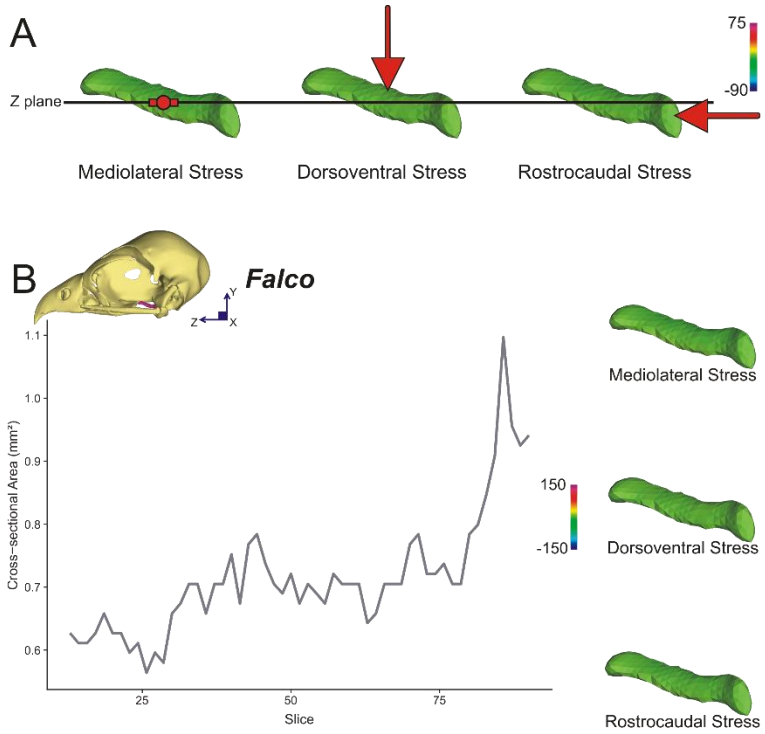

Figure 4-13. Analysis of the cross-sectional properties of pterygoids and principal stresses affecting the pterygoid along the z-plane of action. **(A)** Principal stresses acting on the pterygoids in mediolateral, dorsoventral, and rostrocaudal directions. **(B)** *Falco* In left lateral view showing the placement and orientation of the pterygoid in relation to the rest of the cranium. Pterygoids in the insets are shown in the same left lateral view. Cross-sectional areas (CSAs) of pterygoids are plotted for the length of the bone in all taxa presented in this study.

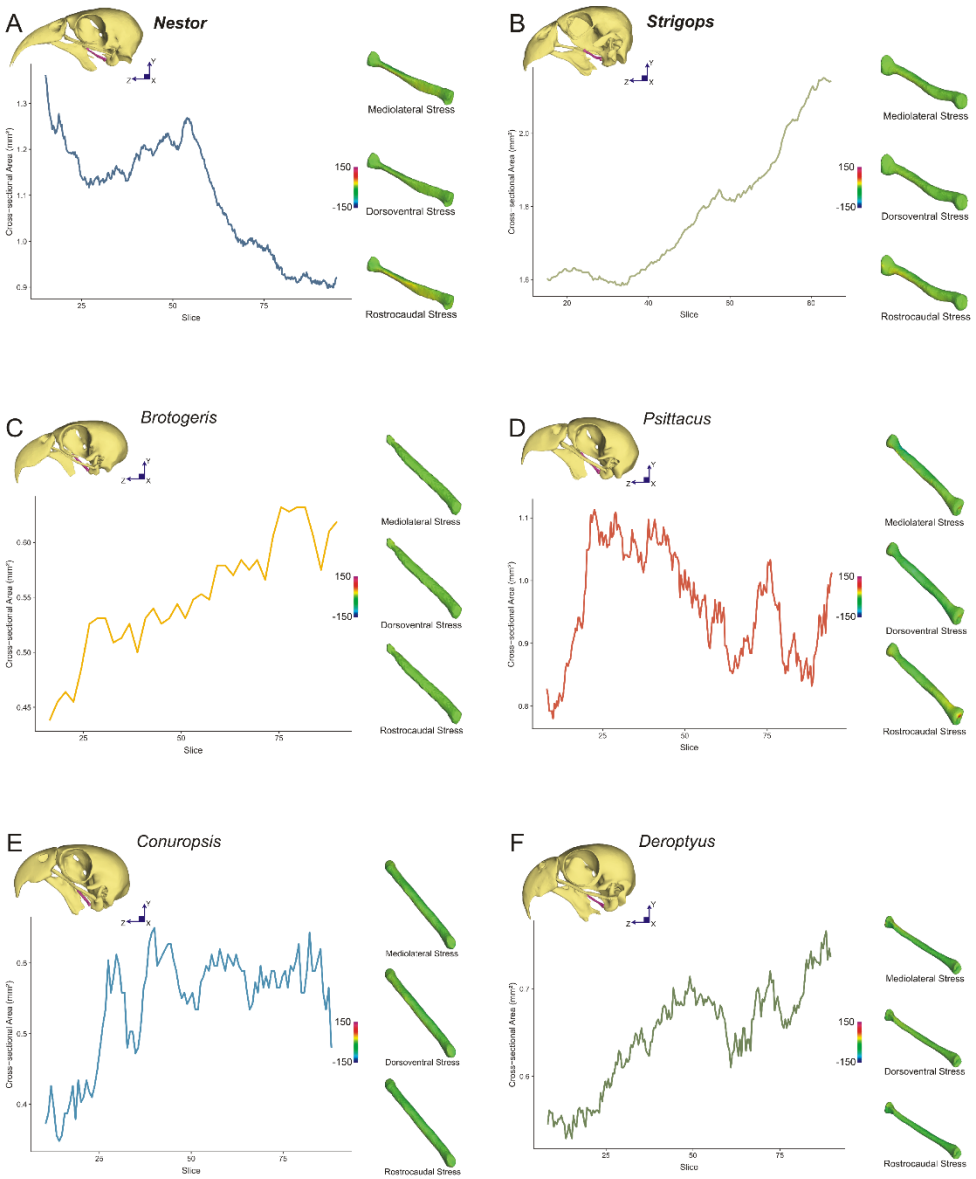

Figure 4-14. Analysis of the cross-sectional properties of pterygoids and principal stresses affecting the pterygoid along the z-plane of action. **(A)** *Nestor* and **(B)** *Strigops* represent the strigopoid lineage of parrots from New Zealand. **(C)** *Brotogeris* represents small-bodied parakeets and parrotlets in this study and exemplifies their pterygoid shape and CSA geometry. **(D)** *Psittacus*, **(E)** *Conuropsis*, and **(F)** *Deroptyus* represent medium sized Old and New World parrots and exemplify their pterygoid shape and geometry. *Conuropsis* **(E)** also represents an extinct, subfossil taxon. Cross-sectional areas (CSAs) of pterygoids are plotted for the length of the bone in all taxa presented in this study. Principal stresses acting on the pterygoids in mediolateral, dorsoventral, and rostrocaudal directions are show to the sides of the graphs.

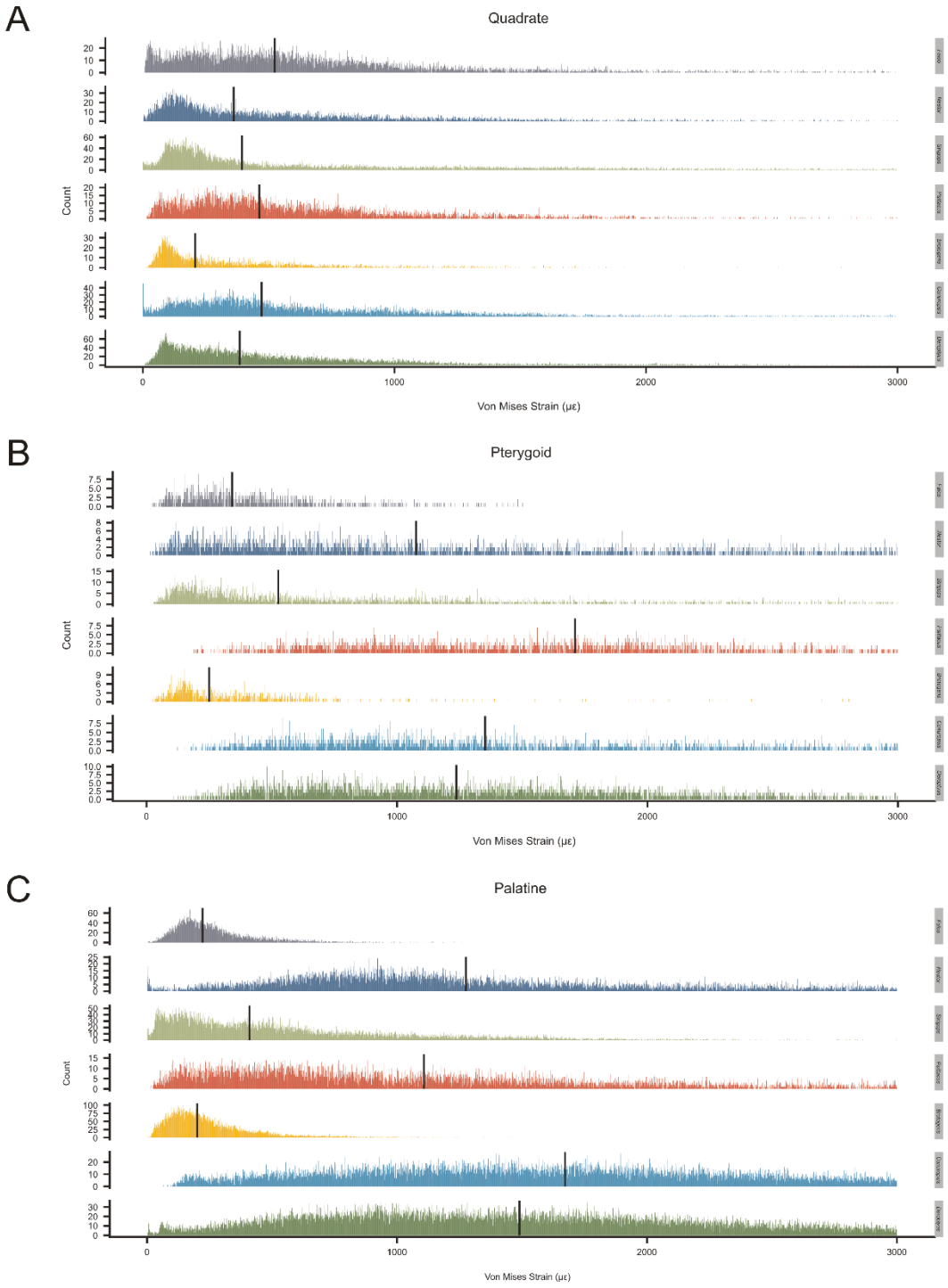

Figure 4-15. Strain profiles in the bones of the palate of Psittaciformes. **(A)** Quadrate, **(B)** palatine, and **(C)** pterygoid strains of parrots and a falcon are represented. Median values from the skeletal element are represented as vertical black bars. The medians facilitate interspecific comparison independent of the shape of the strain curve. All samples are truncated at 3000 με to eliminate structural or artefactual (modeling) failure from the represented data. Patterns of strain propagation between the strigopoid parrots appear weak and inconsistent. Patterns between the Old and New World parrots appear to be more uniform across granivorous taxa, suggesting that the manner in which strain propagates through the palate may be related to feeding behaviors.

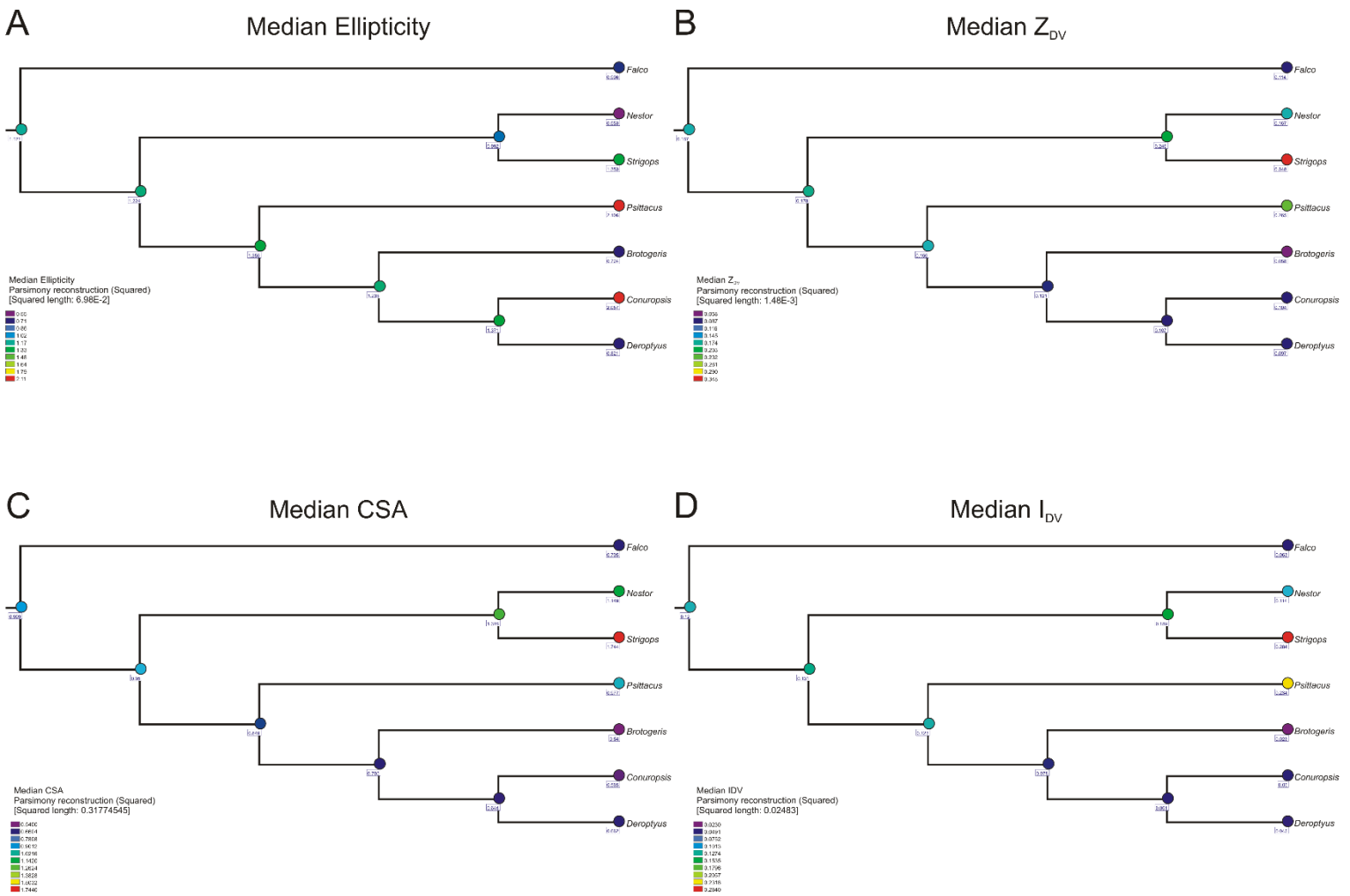

Figure 4-16. Phylogenetic trees showing ancestral state squared-change parsimony reconstructions. **(A)** Median Ellipticity, **(B)** Median Z_{DV}, **(C)** Median CSA, and **(D)** Median I_{DV} characters of shape. Median ellipticity describes overall bone roundness. Median Z_{DV}, $_{m}$edian CSA, and Median I_{DV} describe the bending resistance of the pterygoid. Character gains rates are indicated by labels at nodes. Individual node values are color coded to character evolution rates to facilitate reading the tree. Individual character states of continuous variables appear in Tables 1 and 4 - 6.

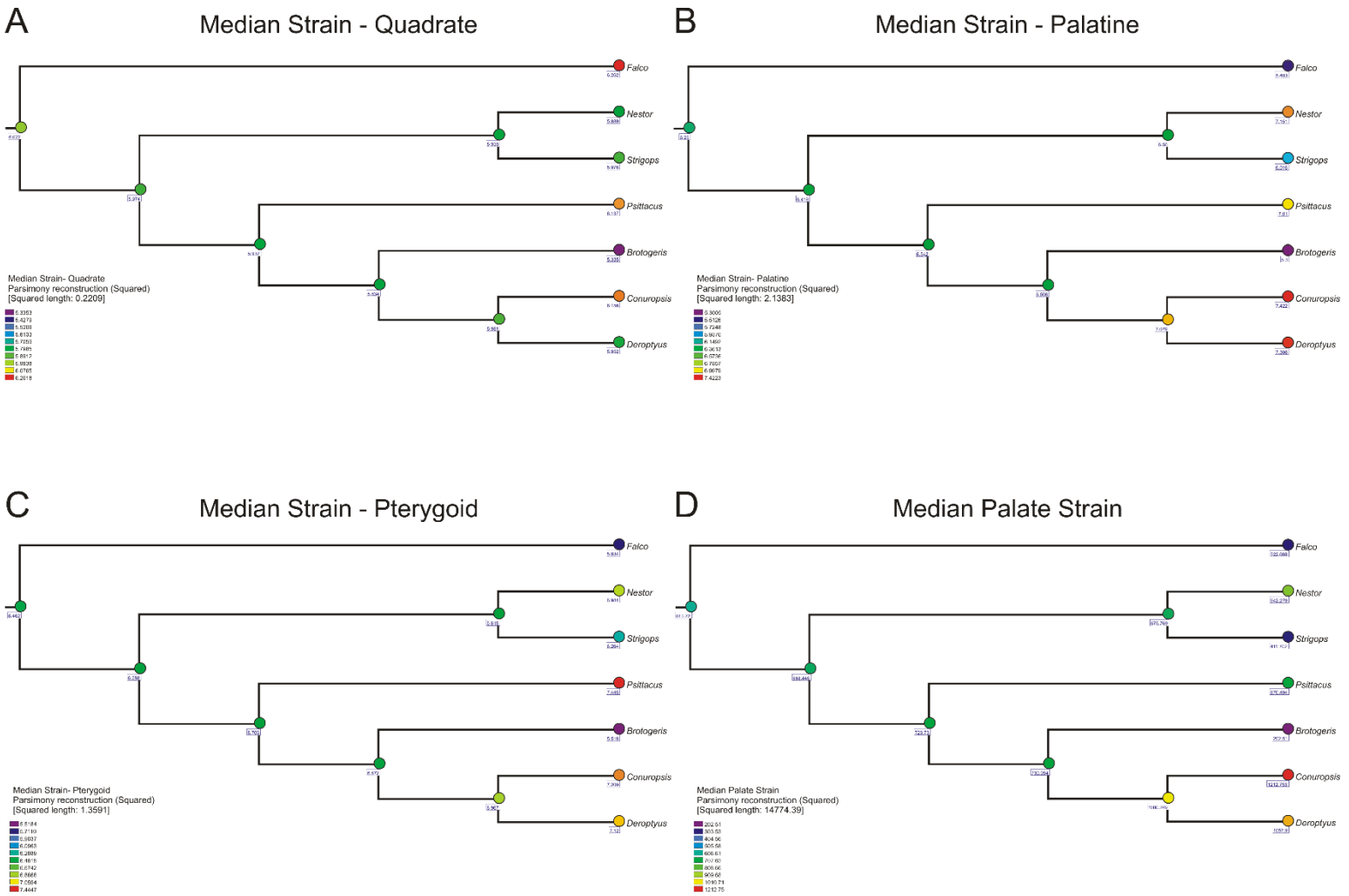

Figure 4-17. Phylogenetic trees showing ancestral state squared-change parsimony reconstructions. **(A)** Median Strain - Quadrate, **(B)** Median Strain -Palatine, **(C)** Median Strain - Pterygoid, and **(D)** Median Palate Strain are characters of strain propagation across the skeletal elements of the palate and the palate as a whole unit. Character gains rates are indicated by labels at nodes. Individual node values are color coded to character evolution rates to facilitate reading the tree. Individual character states of continuous variables appear in Tables 1 and 4 - 6.

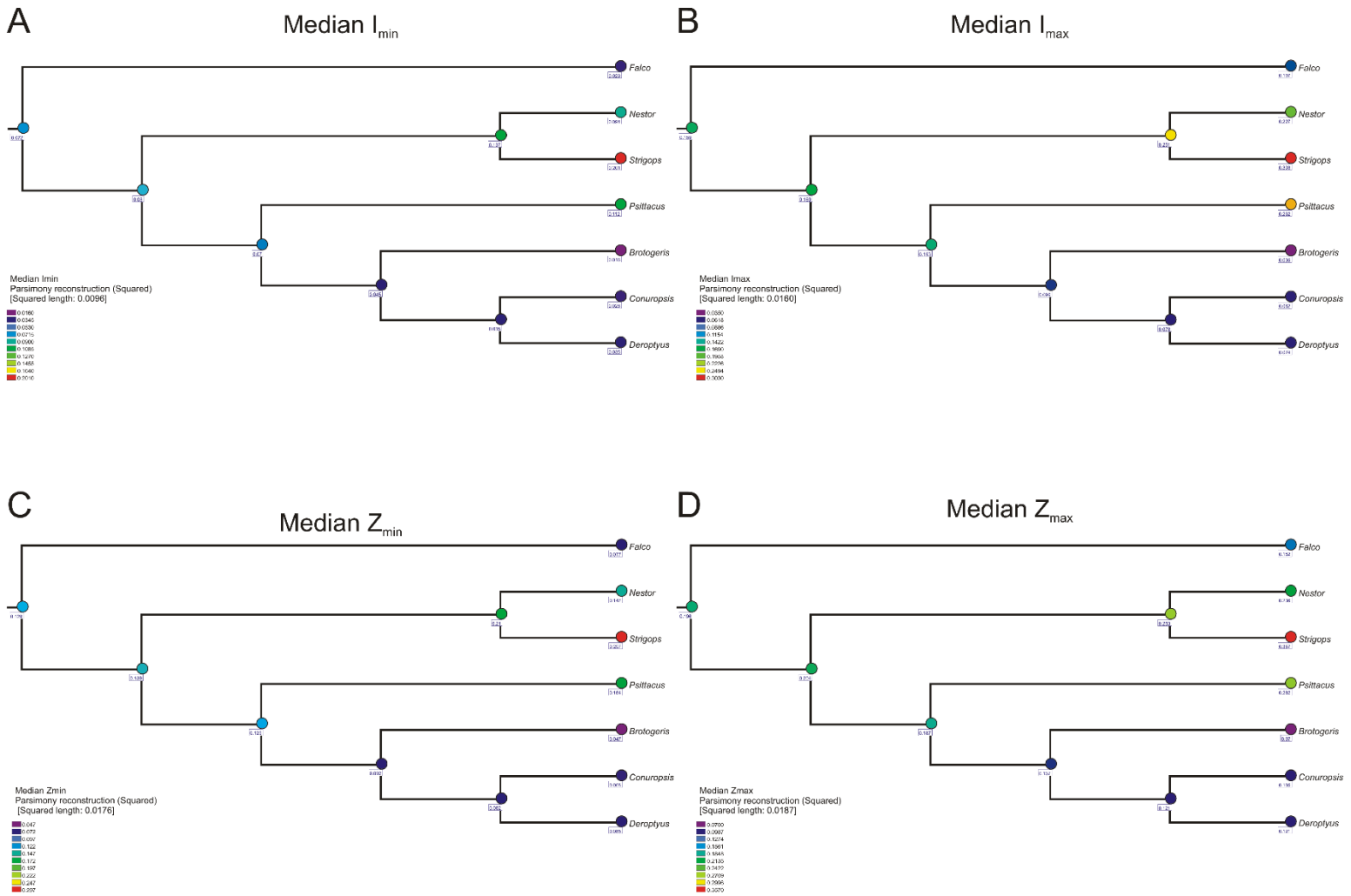

Figure 4-18. Phylogenetic trees showing ancestral state squared-change parsimony reconstructions. **(A)** Median l_{min}, **(B)** Median l_{max}, **(C)** Median Z_{min}, and **(D)** Median Z_{max} characters of shape. Character gains rates are indicated by labels at nodes. Individual node values are color coded to character evolution rates to facilitate reading the tree. Individual character states of continuous variables appear in Tables 1 and 4 - 6.

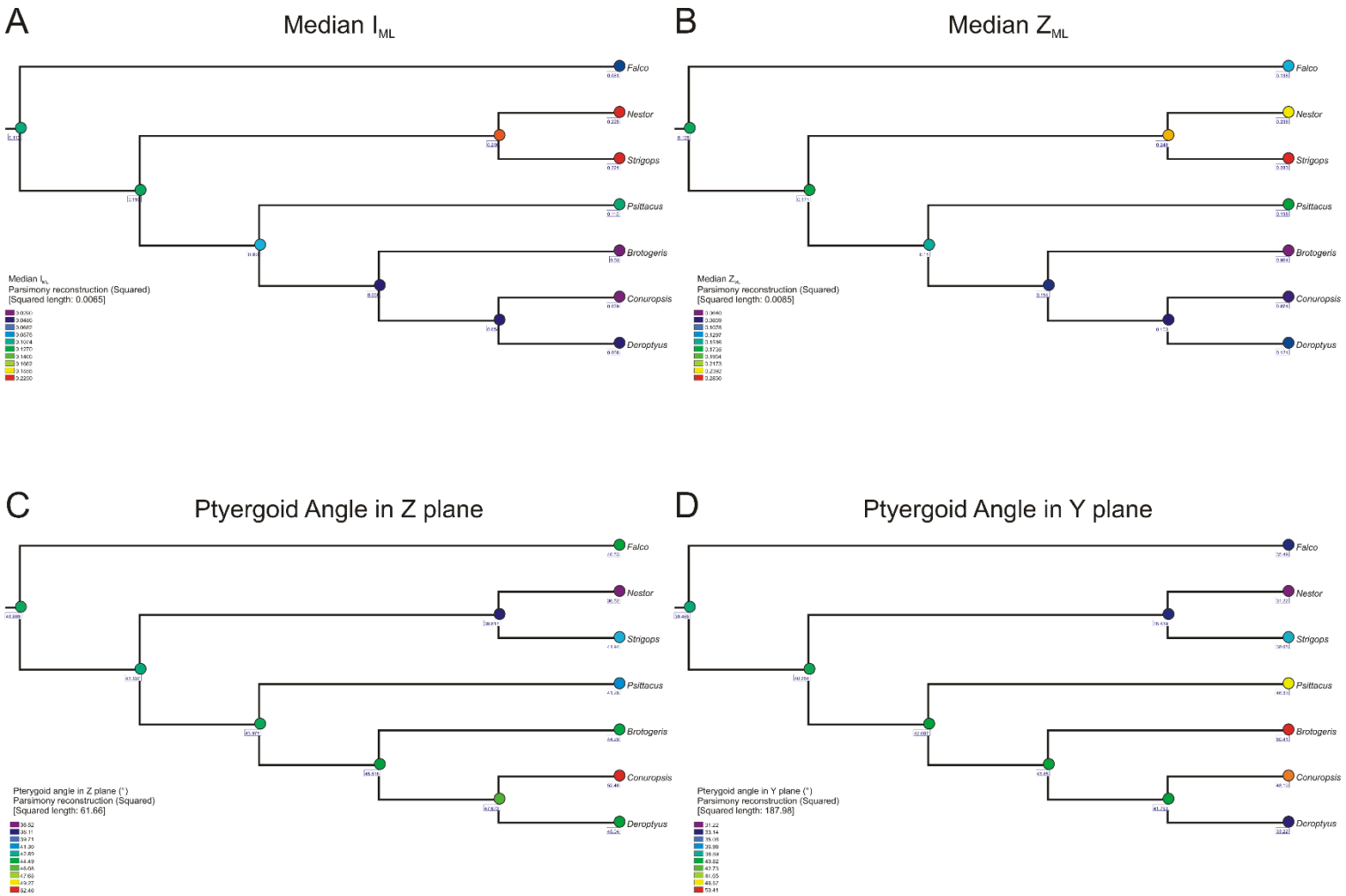

Figure 4-Figure 19. Phylogenetic trees showing ancestral state squared-change parsimony reconstructions. **(A)** Median I_{ML}, **(B)** Median Z_{ML}, **(C)** Pterygoid angle in the Z plane, and **(D)** Pterygoid angle in the Y plane. Median I_{ML}, Median Z_{ML} are characteristics of shape. Character gains rates are indicated by labels at nodes. Individual node values are color coded to character evolution rates to facilitate reading the tree. Individual character states of continuous variables appear in Tables 1 and 4 - 6.

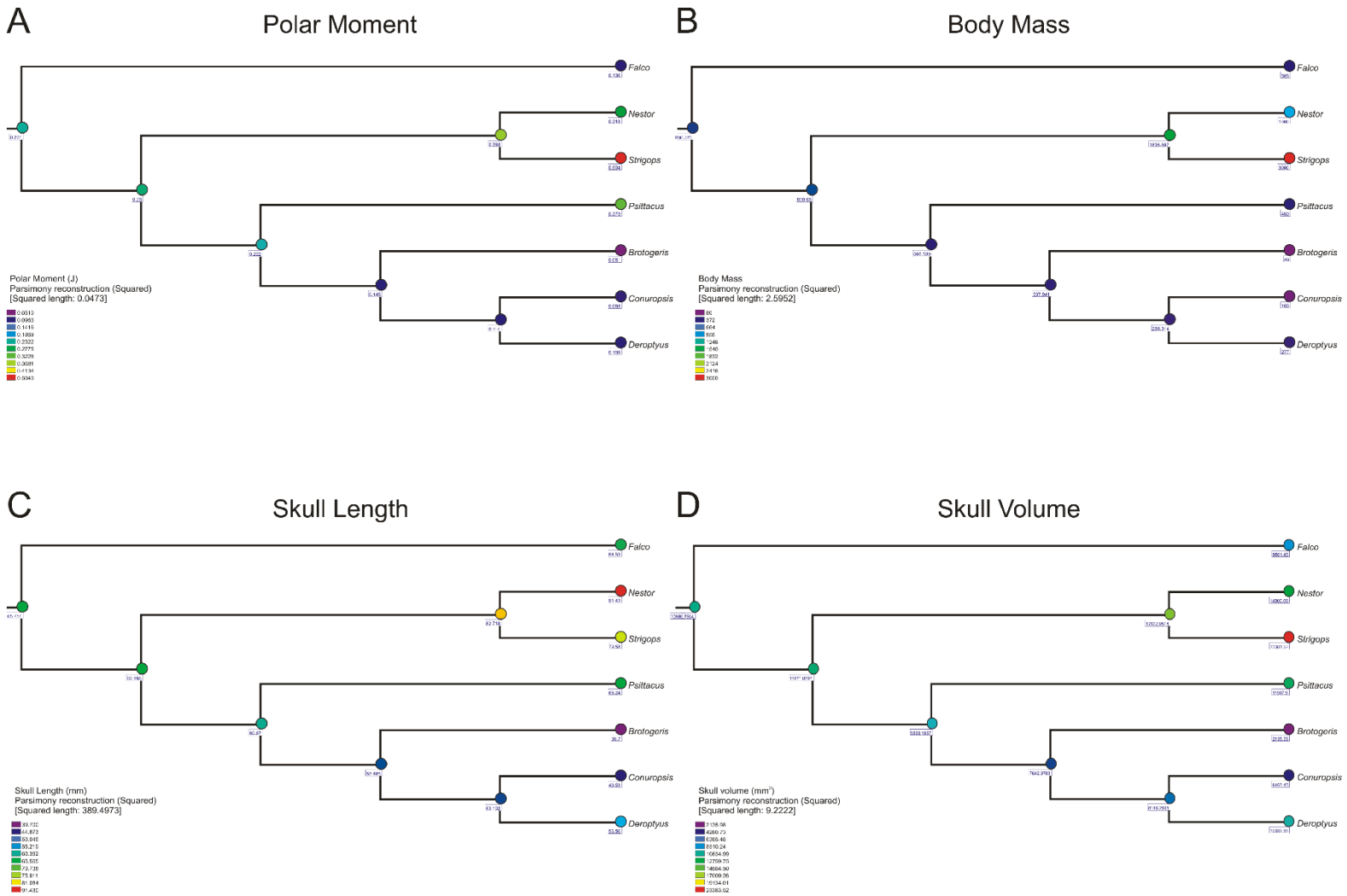

Figure 4-20. Phylogenetic trees showing ancestral state squared-change parsimony reconstructions. **(A)** Polar Moment, **(B)** Body Mass, **(C)** Skull Length, and **(D)** Skull Volume. Character gains rates are indicated by labels at nodes. Individual node values are color coded to character evolution rates to facilitate reading the tree. Individual character states of continuous variables appear in Tables 1 and 4 - 6.

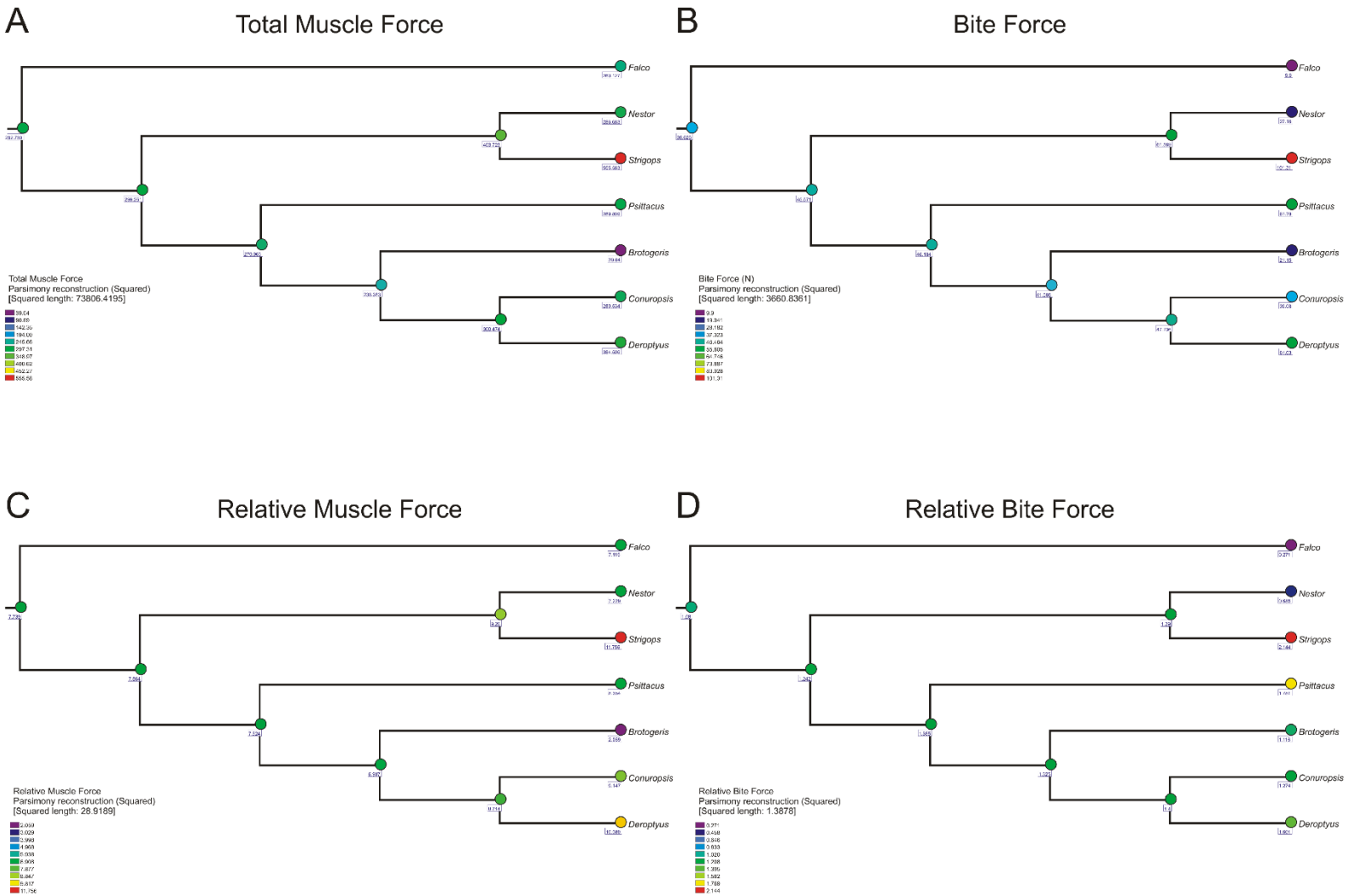

Figure 4-21. Phylogenetic trees showing ancestral state squared-change parsimony reconstructions. **(A)** Total Muscle Force, **(B)** Bite Force, **(C)** Relative Total Force, and **(D)** Relative Bite Force. Character gains rates are indicated by labels at nodes. Individual node values are color coded to character evolution rates to facilitate reading the tree. Individual character states of continuous variables appear in Tables 1 and 4 - 6.

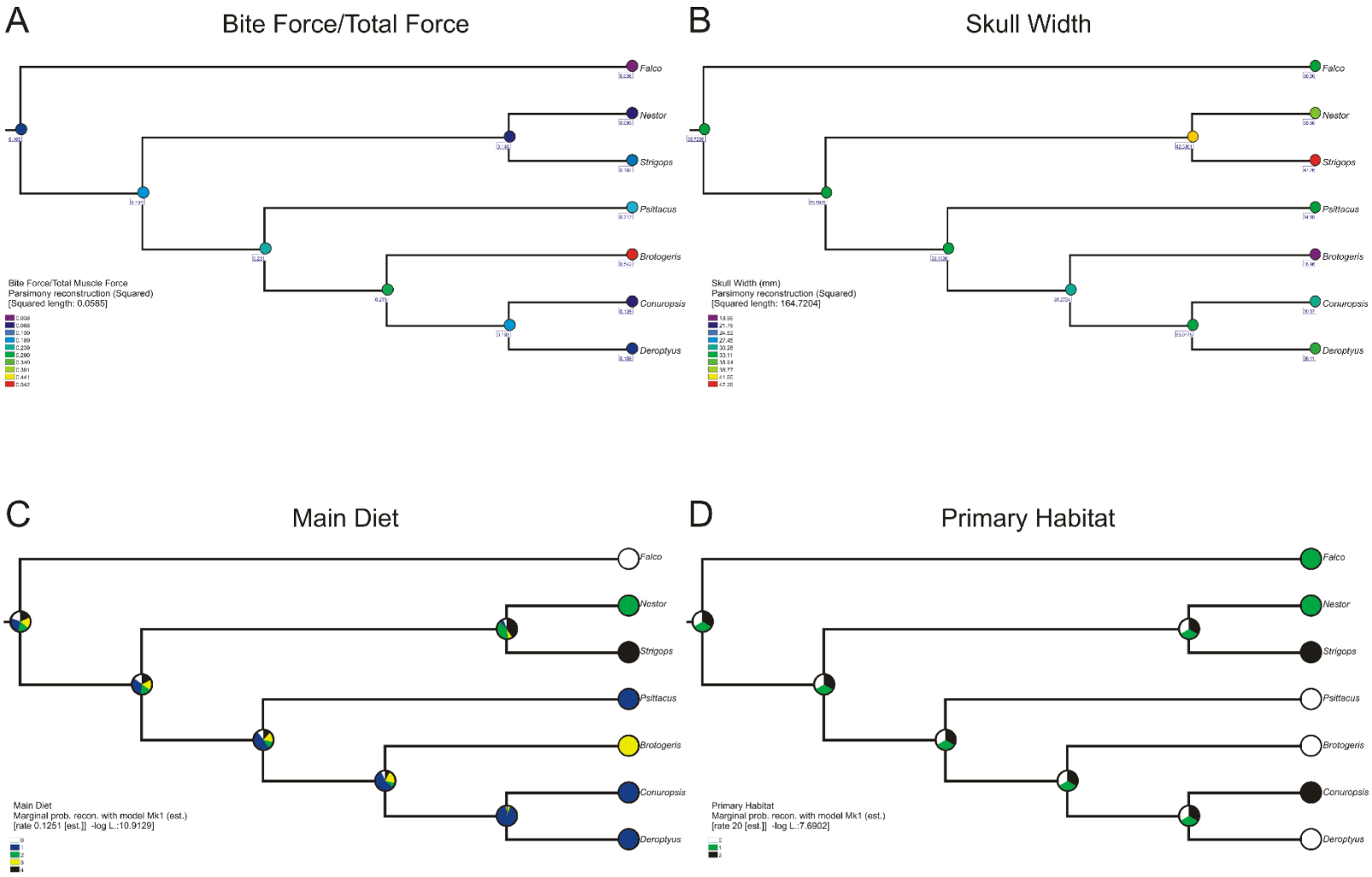

Figure 4-22. Phylogenetic trees showing squared-change parsimony and maximum likelihood ancestral state reconstructions. **(A)** Bite Force/Total Force, **(B)** Skull Width, **(C)** Main Diet, and **(D)** Primary Habitat. Character gains rates are indicated by labels at nodes. Individual node values are color coded to character evolution rates to facilitate reading the tree. Individual character states of continuous variables appear in Tables 1 and 4 - 6. Individual character states of discrete variables appear in Table 7.

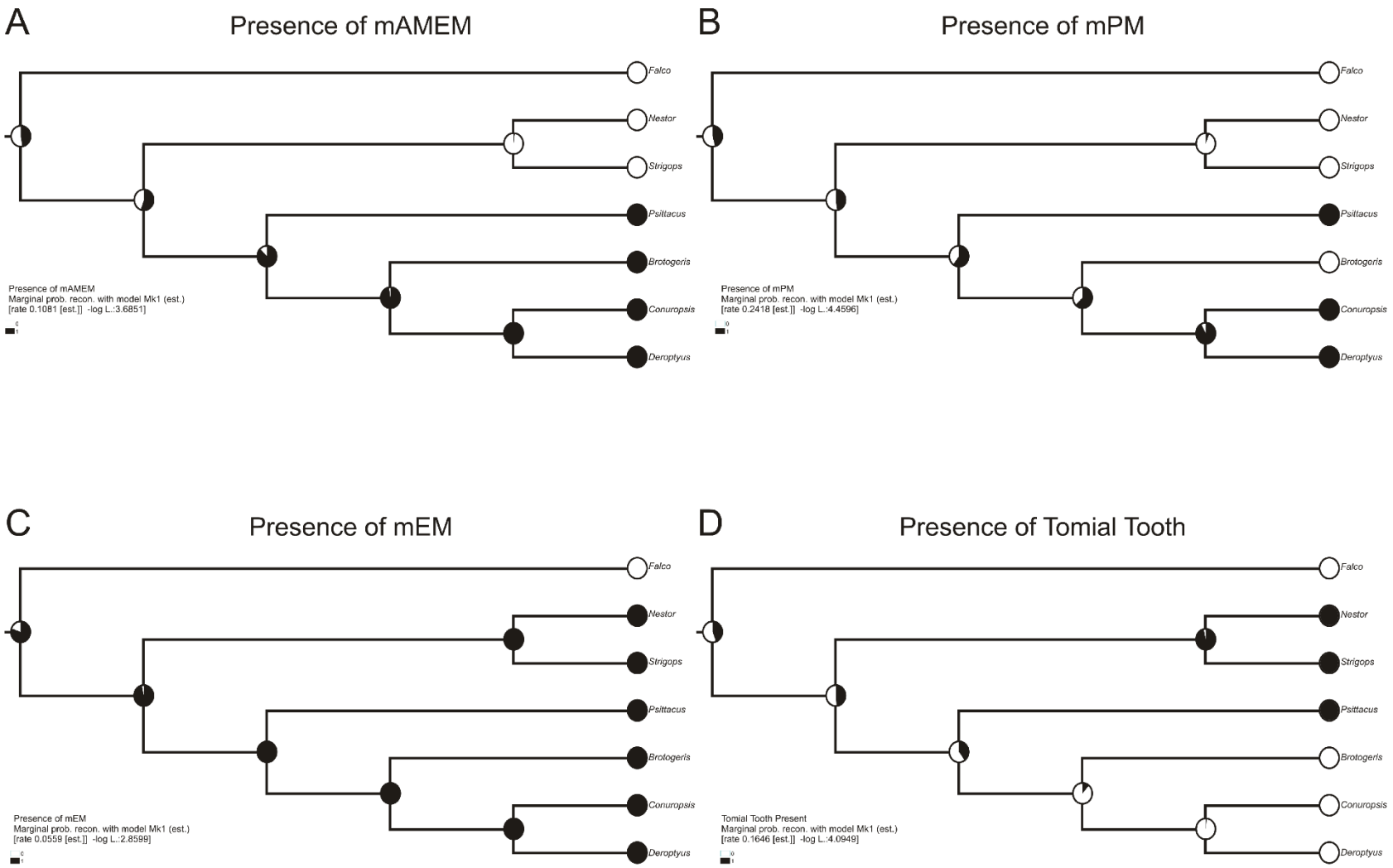

Figure 4-23. Phylogenetic trees showing maximum likelihood ancestral state reconstructions. **(A)** Presence of mAMEM, **(B)** Presence of mPM, **(C)** Presence of mEM, and **(D)** Presence of Tomial Tooth. Individual node values are color coded to character evolution rates to facilitate reading the tree. Individual character states of discrete variables appear in Table 7.

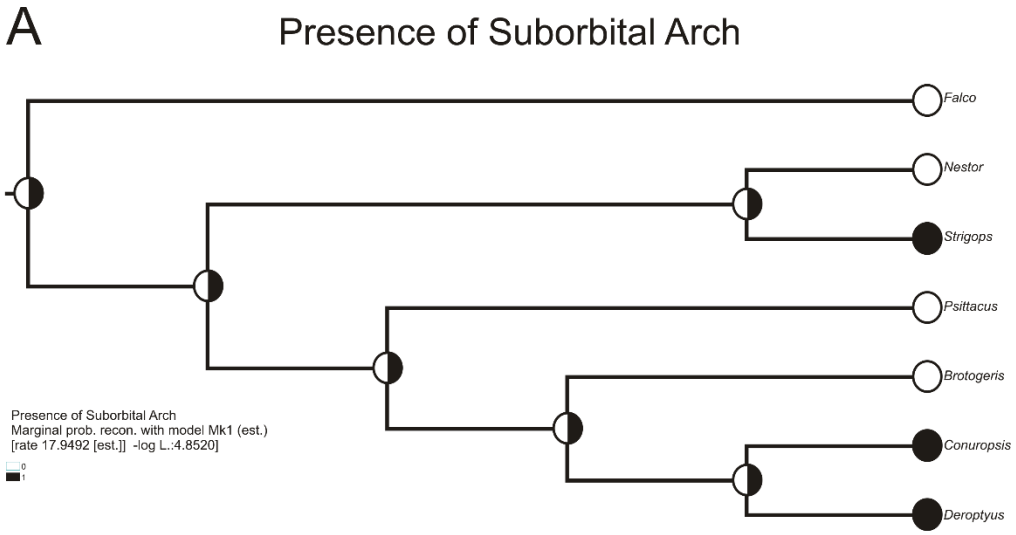

Figure 4-24. Phylogenetic tree showing maximum likelihood ancestral state reconstructions. **(A)** Presence of Suborbital Arch. Individual node values are color coded to character evolution rates to facilitate reading the tree. Individual character states of discrete variables appear in Table 7.

Chapter 5

Summary

Avian feeding ecology is powered by diverse mechanisms with unique musculoskeletal apparatus that biomechanically drive feeding behaviors. The varied behaviors are not discernible from the shape of the feeding apparatus alone, yet the shape of the feeding apparatus is part of the unique system. Muscles, their orientations and the forces they produce, as well as the geometric, mechanical, and material properties of bone also play important roles in feeding behaviors and, eventually, in feeding ecology. This dissertation explored the many parameters of the feeding apparatus, not to attribute any single parameter as an ultimate indicator of feeding ecology, but to explain and define a series of parameters which govern the basic functionality of the feeding apparatus. Here I explored a new method to visualize and model the muscular system of the cranium, the effects of modeling specific postures of the feeding apparatus, and new methods to statistically analyze, mechanically define, and phylogenetically map characters of the feeding apparatus.

The overarching goal of the dissertation research presented here was to test and evaluate hypotheses and predictions concerning feeding behavior, changes in muscle function over time, and the biomechanical environment of the feeding apparatus. Over the course of this work I showed that changes in muscle function over time can be used to inform the use of muscles in different ways by different taxa. I also showed that instances of behavior can be validated and that hypotheses of the feeding behaviors of fossil taxa can be tested using new

methods of modeling. Finally, I showed that the findings of my initial two studies are capable of being integrated and that predictions of the biomechanical environment of the feeding apparatus can be evaluated using the methods described in the first two studies. Additionally, I showed that a geometric shape analysis of the pterygoid can be informed by and tested using the biomechanical analyses I described previously. The integration of all of the studies I have presented here is important in showing that a multifaceted approach to investigating the biomechanical environment of the feeding apparatus is integral to describing not only a given taxon's mechanisms, but also the evolution of suites of mechanical characters.

The first chapter of this dissertation outlined the evolution of the avian lineage and discussed feeding in birds. I laid the groundwork for the anatomical basis of the later chapters of this thesis and discussed the functions of this foundational anatomy. Additionally, the first chapter discussed a feeding behavior integral to the other chapters of this thesis, cranial kinesis, and the basic anatomy and manner in which kinesis functions.

In chapter two I introduced a new method to visualize the 3D architecture of cranial musculature using a graphical tool that has been used effectively in many different disciplines. Ternary plots employ three axes that, when supplied with three points in space, recreates the three dimensional architecture of a system in a two dimensional graphic representation. Using ternary plots, I showed how we are able to trace muscle orientation changes throughout feeding cycles, ontogeny of animals, and across a phylogeny. I also showed the different

ways, using ternary plots, in which taxa use diverse muscles to accomplish similar goals using disparate hard-biting taxa as an example.

In chapter three I showed how finite element models can be constructed in multiple postures to simulate disparate feeding behaviors. I showed how statistical analysis of the palate across hypothetical postures of cranial kinesis can be used to validate recreations of known postures and how the same analyses can be used to show that a posture is unlikely or even detrimental to the animal displaying that posture. These methods were applied to a series of hypothesized postures in the extinct taxon *Tyrannosaurus rex* to analyze what, if any, cranial kinesis *T. rex* was capable of producing when it engaged in bouts of feeding. The findings of this chapter indicated that my statistical methods are capable of validating postural models and, in the case of *T. rex*, that hypotheses concerning extinct animals are testable. I found, specifically, that the skull of *T. rex* was constructed such that its skull was not capable of cranial kinesis and that postures other than the non-kinetic posture resulted in detrimental effects within the palate of *T. rex*.

In chapter four I conducted extensive biomechanical analyses to determine and describe the parameters governing the function of the feeding apparatus. The stress and strain environments of the palate and the mechanics and geometry of the propulsive skeletal element of the palate, the pterygoid, were described and analyzed. Stress and strain profiles of the palate were used to describe the capability of the palate to dissipate stress and strains throughout the skeletal structures. The muscle system of the feeding apparatus was mapped

and absolute and relative forces were described and analyzed across parrots. To describe the propulsive unit of the palate, the pterygoid, geometric and mechanical parameters were analyzed and their relationships with one another and impact on the pterygoid and downstream in the palate were described. All of the data from the analyses of the palate and pterygoid specifically were then mapped onto a series of phylogenetic trees and the relationships for each character were analyzed.

The studies described here introduce many new modeling and graphic methods of describing and analyzing the feeding apparatus of both related and highly disparate avian and non-avian taxa. New methods of producing models in diverse postures, with realistic bone and joint materials, contribute significantly to the finite element model and biomechanics disciplines. These methods can be used across multiple taxa to model and analyze not only feeding behaviors, but also locomotor, respiratory, and many other biomechanically important behaviors. New visualization methods, including the repurposing of ternary plots, that are detailed in these studies will contribute immensely to all 2D methods of publication. These new visualizations enable 3D information to be portrayed in new and meaningful ways that were previously unknown in 2D publications.

Finally, the new statistical analyses of postural models, new methods of analyzing the stress and strain environment of the feeding apparatus, and geometric analyses of the pterygoid are integral to better understanding and describing the biomechanical environment of the palate of animals that engage in cranial kinesis. These methods can be used to analyze the feeding apparatus of

vertebrates with mobile skulls that are capable of cranial kinesis, whether the animals engage in any specific feeding behavior or not. The analysis of why, or why not, elements of the skull move during feeding bouts will further inform our knowledge of the evolution of the feeding apparatus. Overall, this dissertation adds significant contributions to the methods of finite element modelling and biomechanical statistical analysis and enhances studies of feeding behavior and ecology.

Literature Cited

Abdala V, Moro S. 1996. Cranial musculature of South American Gekkonidae. J Morphol 229:59–70.

Aguirre LF, Herrel A, Van Damme R, Matthysen E. 2003. The implications of food hardness for diet in bats. Funct Ecol 17:201–12

Alexander RM. 1981. Factors of safety in the structure of animals. Sci Prog 67:109–30.

Anderson RA, McBrayer LD, Herrel A. 2008. Bite force in vertebrates: Opportunities and caveats for use of a nonpareil whole-animal performance measure. Biol J Linn Soc Lond 93:709–20.

Arnold K, Bordoli L, Kopp J, Schwede T. 2006. The SWISS-MODEL workspace: a web-based environment for protein structure homology modelling. Bioinformatics 22:195–201.

Attard MRG, Wilson LAB, Worthy TH, Scofield P, Johnston P, Parr WCH, Wroe S. 2016. Moa diet fits the bill: virtual reconstruction incorporating mummified remains and prediction of biomechanical performance in avian giants. Proceedings of the Royal Society B: Biological Sciences 283:20152043.

Auersperg AMI, von Bayern AMP, Gajdon GK, Huber L, Kacelnik A. 2011. Flexibility in problem solving and tool use of kea and New Caledonian crows in a multi access box paradigm. PLoS One 6:e20231.

Baier DB, Gatesy SM, Dial KP. 2013. Three-Dimensional, High-Resolution Skeletal Kinematics of the Avian Wing and Shoulder during Ascending Flapping Flight and Uphill Flap-Running. PLoS One 8:e63982.

Bailleul AM, Witmer LM, Holliday CM. 2017. Cranial joint histology in the mallard duck (*Anas platyrhynchos*): new insights on avian cranial kinesis. J Anat 230:444–60.

Baker AJ, Huynen LJ, Haddrath O, Millar CD, Lambert DM. 2005. Reconstructing the tempo and mode of evolution in an extinct clade of birds with ancient DNA: the giant moas of New Zealand. Proc Natl Acad Sci USA 102:8257–62.

Baker AJ, Haddrath O, McPherson JD, Cloutier A. 2014. Genomic Support for a Moa–Tinamou Clade and Adaptive Morphological Convergence in Flightless Ratites. Mol Biol Evol 31:1686–96.

Balanoff AM, Bever GS, Rowe TB, Norell MA. 2013. Evolutionary origins of the avian brain. Nature 501:93–96.

Balanoff AM, Smaers JB, Turner AH. 2016. Brain modularity across the theropod-bird transition: testing the influence of flight on neuroanatomical variation. J Anat 229:204–14.

Bates KT, Falkingham PL. 2012. Estimating maximum bite performance in *Tyrannosaurus rex* using multi-body dynamics. Biol Lett 8:660–64.

Bates KT, Falkingham PL. 2018. The importance of muscle architecture in biomechanical reconstructions of extinct animals: a case study using *Tyrannosaurus rex*. J Anat.

Beaufrère H, Laniesse D, Kabakchiev C, Axelson R, Zur Linden A. 2019. Multiple fractures and luxations of palatofacial bones in a hawk-headed parrot (*Deroptyus accipitrinus*). J Am Vet Med Assoc 254:251–56.

Bhullar B-AS, Hanson M, Fabbri M, Pritchard A, Bever GS, Hoffman E. 2016. How to Make a Bird Skull: Major Transitions in the Evolution of the Avian Cranium, Paedomorphosis, and the Beak as a Surrogate Hand. Integr Comp Biol 56:389–403.

Biewener AA, Taylor CR. 1986. Bone strain: a determinant of gait and speed? J Exp Biol 123:383–400.

Bimber O, Gatesy SM, Witmer LM, Raskar R, Miguel Encarnação L. 2002. Merging fossil specimens with computer-generated information. Computer 35:25–30.

Bock WJ. 1963. Evolution and Phylogeny in Morphologically Uniform Groups. Am Nat 97:265–85.

Bock WJ. 1964. Kinetics of the avian skull. J Morphol 114:1–41.

Bock WJ. 1966. An Approach to the Functional Analysis of Bill Shape. Auk 83:10–51.

Bock WJ. 1999. Cranial kinesis revisited. Zool Anz 238:27–40.

Bout RG, Zweers GA. 2001. The role of cranial kinesis in birds. Comparative Biochemistry and Physiology - A Molecular and Integrative Physiology 131:197–205.

Brainerd EL, Baier DB, Gatesy SM, Hedrick TL, Metzger KA, Gilbert SL, Crisco JJ. 2010. X-ray reconstruction of moving morphology (XROMM): precision, accuracy and applications in comparative biomechanics research. J Exp Zool A Ecol Genet Physiol 313:262–79.

Bramwell CD, Whitfield GR. 1974. Biomechanics of Pteranodon. Transactions of the Royal Society B 267:503–81.

Bright JA. 2014. A review of paleontological finite element models and their validity. J Paleontol.

Bright JA, Marugán-Lobón J, Cobb SN, Rayfield EJ. 2016. The shapes of bird beaks are highly controlled by nondietary factors. Proceedings of the National Academy of Sciences 113:5352–57.

Brochu CA. 2001. Progress and Future Directions in Archosaur Phylogenetics. J Paleontol 75:1185–1201.

Bühler P. 1981. Functional anatomy of the avian jaw apparatus. In: King AS, McLelland J, editors. Form and function in birds Academic Press. p. 439–68.

Burton PJK. 1974a. Feeding and the Feeding Apparatus in Waders London: Trustees of the British Museum.

Burton PJK. 1974b. Jaw and tongue features in Psittaciformes and other orders with special reference to the anatomy of the Tooth-billed pigeon (*Didunculus strigirostris*). J Zool 174:255–76.

Busbey AB. 1989. Form and function of the feeding apparatus of *Alligator mississippiensis*. J Morphol 202:99–127.

Busbey AB. 1997. Structural consequences of skull flattening in crocodilians. In: Thomason J, editor. Functional Morphology in Vertebrate Paleontology Cambridge University Press. p. 173–92.

Butler DJ. 2006. The habitat, food and feeding ecology of kakapo in Fiordland: a synopsis from the unpublished MSc thesis of Richard Gray. Notornis 53:55.

Camp AL, Roberts TJ, Brainerd EL. 2015. Swimming muscles power suction feeding in largemouth bass. Proceedings of the National Academy of Sciences 112:8690–95.

Campàs O, Mallarino R, Herrel A, Abzhanov A, Brenner MP. 2010. Scaling and shear transformations capture beak shape variation in Darwin’s finches. Proc Natl Acad Sci USA 107:3356–60.

Campbell AM, Cler ML, Skurla CP, Kuehl JJ. 2016. Damage accumulation of bovine bone under variable amplitude loads. Bone Reports 5:320–32.

Capano JG, Moritz S, Cieri RL, Reveret L, Brainerd EL. 2019. Rib Motions Don't Completely Hinge on Joint Design: Costal Joint Anatomy and Ventilatory Kinematics in a Teiid Lizard, Salvator merianae. Integr Org Biol 1.

Carlson KJ, Stout D, Jashashvili T, de Ruiter DJ, Tafforeau P, Carlson K, Berger LR. 2011. The endocast of MH1, *Australopithecus sediba*. Science 333:1402–7.

Carr TD. 1999. Craniofacial ontogeny in Tyrannosauridae (Dinosauria, Coelurosauria). J Vert Paleontol 19:497–520.

Carril J, Degrange FJ, Tambussi CP. 2015. Jaw myology and bite force of the monk parakeet (Aves, Psittaciformes). J Anat 227:34–44.

Cartmill M. 1974. Pads and Claws in Arboreal Locomotion. In: Jenkins FA, editor. Primate Locomotion Academic Press. p. 45–83.

Cartmill, M. 1985. Climbing. In: Milton Hildebrand Dennis M. Bramble Karel F. Liem David B. Wake, editor. Functional Vertebrate Morphology Harvard Univ. Press. p. 73–88.

Chandler RJ. 2002. Rhynchokinesis in waders. Br Birds 95:395–97.

Charles JP, Cappellari O, Spence AJ, Wells DJ, Hutchinson JR. 2016. Muscle moment arms and sensitivity analysis of a mouse hindlimb musculoskeletal model. J Anat 229:514–35.

Chatterjee S. 1991. Cranial anatomy and relationships of a new Triassic bird from Texas. Philos Trans R Soc Lond B Biol Sci 332:277–346.

Chen W-F, Han DJ. 2007. Plasticity for Structural Engineers J. Ross Publishing.

Chien CH, Wu YD, Chao YJ, Chen T, Chen WF, Yu JC, Li X. 2008. The effects of different cranial modules on mechanical properties of cranial suture in Lewis rats and same-aged C57BL/6 mice. In: Strain p. 272–77.

Christensen R, Kleindorfer S. 2009. Jack-of-all-trades or master of one? Variation in foraging specialisation across years in Darwin's Tree Finches (Camarhynchus spp.). J Ornithol 150:383–91.

Chubb AL. 2004. New nuclear evidence for the oldest divergence among neognath birds: the phylogenetic utility of ZENK (i). Mol Phylogenet Evol 30:140–51.

Claes R, Muyshondt PGG, Van Hoorebeke L, Dhaene J, Dirckx JJJ, Aerts P. 2017. The effect of craniokinesis on the middle ear of domestic chickens (*Gallus gallus domesticus*). J Anat 230:414–23.

Claramunt S, Cracraft J. 2015. A new time tree reveals Earth history's imprint on the evolution of modern birds. Sci Adv 1:e1501005.

Cohen M, Prialnik D, Podolak M. 2003. A quasi-3D model for the evolution of shape and temperature distribution of comet nuclei—application to Comet 46P/Wirtanen. New Astron 8:179–89.

Cole JH, van der Meulen MCH. 2011. Whole bone mechanics and bone quality. Clin Orthop Relat Res 469:2139–49.

Cost IN, Middleton KM, Echols MS, Witmer LM, Davis JL, Holliday CM. 2019. Palatal biomechanics and its significance for cranial kinesis in *Tyrannosaurus rex*. Anat Rec.

Cuff AR, Bright JA, Rayfield EJ. 2015. Validation experiments on finite element models of an ostrich (*Struthio camelus*) cranium. PeerJ 3:e1294.

Cundall D. 1983. Activity of Head Muscles During Feeding by Snakes: A Comparative Study. Am Zool 23:383–96.

Curtis N. 2011. Craniofacial biomechanics: an overview of recent multibody modelling studies. J Anat 218:16–25.

Currey JD. 2006. Bones: Structure and Mechanics Princeton University Press.

Curtis N, Jones MEH, Evans SE, O'Higgins P, Fagan MJ. 2010. Feedback control from the jaw joints during biting: An investigation of the reptile Sphenodon using multibody modelling. J Biomech 43:3132–37.

Curtis N, Jones MEH, Evans SE, O'Higgins P, Fagan MJ. 2013. Cranial sutures work collectively to distribute strain throughout the reptile skull. J R Soc Interface 10:20130442.

Curtis N, Jones MEH, Shi J, O'Higgins P, Evans SE, Fagan MJ. 2011. Functional relationship between skull form and feeding mechanics in sphenodon, and implications for diapsid skull development. PLoS One 6:31–33.

Davis JL, Santana SE, Dumont ER, Grosse IR. 2010. Predicting bite force in mammals: two-dimensional versus three-dimensional lever models. J Exp Biol 213:1844–51.

Dawson MM, Metzger KA, Baier DB, Brainerd EL. 2011. Kinematics of the quadrate bone during feeding in mallard ducks. J Exp Biol 214:2036–46.

Daza JD, Mapps AA, Lewis PJ, Thies ML, Bauer AM. 2015. Peramorphic traits in the tokay gecko skull. J Morphol 276:915–28.

Degrange FJ, Picasso MBJ. 2010. Geometric morphometrics of the skull of Tinamidae (Aves, Palaeognathae). Zoology 113:334–38.

Degrange FJ, Tambussi CP, Moreno K, Witmer LM, Wroe S. 2010. Mechanical analysis of feeding behavior in the extinct “terror bird” *Andalgalornis steulleti* (Gruiformes: Phorusrhacidae). PLoS One 5:e11856.

Demery ZP, Chappell J, Martin GR. 2011. Vision, touch and object manipulation in Senegal parrots *Poicephalus senegalus*. Proc Biol Sci 278:3687–93.

Demes B, Jungers WL. 1993. Long bone cross-sectional dimensions, locomotor adaptations and body size in prosimian primates. J Hum Evol 25:57–74.

Demes B, Jungers WL, Selpien K. 1991. Body Size, Locomotion, and Long Bone Cross-Sectional Geometry in lndriid Primates. Am J Phys Anthropol 86:537–47.

Dodson P. 1975. Taxonomic Implications of Relative growth in Lambeosaurine Hadrosaurs. Syst Biol 24:37–54.

Doube M, Kłosowski MM, Arganda-Carreras I, Cordelières FP, Dougherty RP, Jackson JS, Schmid B, Hutchinson JR, Shefelbine SJ. 2010. BoneJ: Free and extensible bone image analysis in ImageJ. Bone 47:1076–79.

Du Plessis A, Slabbert R, Swanepoel LC, Els J, Booysen GJ, Ikram S, Cornelius I. 2015. Three-dimensional model of an ancient Egyptian falcon mummy skeleton. Rapid Prototyping Journal 21:368–72.

Dullemeijer P. 1956. The functional morphology of the head of the common viper. Archives neerlandaises de zoologie 11:387–497.

Dumont ER, Grosse IR, Slater GJ. 2009. Requirements for comparing the performance of finite element models of biological structures. J Theor Biol 256:96–103.

Dumont ER, Herrel A. 2003. The effects of gape angle and bite point on bite force in bats. J Exp Biol 206:2117–23.

Dumont ER, Piccirillo J, Grosse IR. 2005. Finite-element analysis of biting behavior and bone stress in the facial skeletons of bats. Anatomical Record - Part A Discoveries in Molecular, Cellular, and Evolutionary Biology 283:319–30.

Dumont ER, Samadevam K, Grosse I, Warsi OM, Baird B, Davalos LM. 2014. Selection for mechanical advantage underlies multiple cranial optima in new world leaf-nosed bats. Evolution 68:1436–49.

Dyke GJ, Van Tuinen M. 2004. The evolutionary radiation of modern birds (Neornithes): Reconciling molecules, morphology and the fossil record. Zool J Linn Soc 141:153–77.

Eng CM, Ward SR, Vinyard CJ, Taylor AB. 2009. The morphology of the masticatory apparatus facilitates muscle force production at wide jaw gapes in tree-gouging common marmosets (*Callithrix jacchus*). J Exp Biol 212:4040–55.

Ericson PGP, Anderson CL, Britton T, Elzanowski A, Johansson US, Källersjö M, Ohlson JI, Parsons TJ, Zuccon D, Mayr G. 2006. Diversification of Neoaves: integration of molecular sequence data and fossils. Biol Lett 2:543–47.

Erickson GM, Lappin AK, Vliet KA. 2003. The ontogeny of bite-force performance in American alligator (*Alligator mississippiensis*). J Zool 260:317–27.

Estrella SM, Masero JA. 2007. The use of distal rhynchokinesis by birds feeding in water. J Exp Biol 210:3757–62.

Evans DC, Ridgely RC, Witmer LM. 2009. Endocranial anatomy of lambeosaurine hadrosaurids (Dinosauria: Ornithischia): A sensorineural perspective on cranial crest function. Anat Rec 292:1315–37.

Evans SE. 2003. At the feet of the dinosaurs: the early history and radiation of lizards. Biol Rev Camb Philos Soc 78:513–51.

Fabbri M, Mongiardino Koch N, Pritchard AC, Hanson M, Hoffman E, Bever GS, Balanoff AM, Morris ZS, Field DJ, Camacho J, Rowe TB, Norell MA, Smith RM, Abzhanov A, Bhullar B-AS. 2017. The skull roof tracks the brain during the evolution and development of reptiles including birds. Nat Ecol Evol 1:1543–50.

Fain MG, Houde P. 2004. Parallel radiations in the primary clades of birds. Evolution 58:2558–73.

Fain MG, Houde P. 2007. Multilocus perspectives on the monophyly and phylogeny of the order Charadriiformes (Aves). BMC Evol Biol 7:35.

Felice RN, Goswami A. 2018. Developmental origins of mosaic evolution in the avian cranium. Proc Natl Acad Sci USA 115:555–60.

Felice RN., Tobias JA, Pigot AL., Goswami A. 2019. Dietary niche and the evolution of cranial morphology in birds. Proceedings of the Royal Society B: Biological Sciences 286:20182677.

Ferrara TL, Clausen P, Huber DR, McHenry CR, Peddemors V, Wroe S. 2011. Mechanics of biting in great white and sandtiger sharks. J Biomech 44:430–35.

Fessl B, Loaiza AD, Tebbich S, Glyn Young H. 2011. Feeding and nesting requirements of the critically endangered Mangrove Finch *Camarhynchus heliobates*. J Ornithol 152:453–60.

Figueirido B, Tseng ZJ, Martín-Serra A. 2013. Skull Shape Evolution In Durophagous Carnivorans. Evolution 67:1975–93.

Fox R, Lehmkuhle SW, Bush RC. 1977. Stereopsis in the falcon. Science 197:79–81.

Francisco MR, Oliveira Lunardi V, Galetti M. 2002. Massive Seed Predation of *Pseudobombax grandiflorum* (Bombacaceae) by Parakeets *Brotogeris versicolurus* (Psittacidae) in a Forest Fragment in Brazil1. Biotropica 34:613–15.

Frazzetta TH. 1962. A Functional Consideration of Cranial Kinesis in Lizards. J Morphol 111:287–319.

Friedrich F, Beutel RG. 2008. Micro-computer tomography and a renaissance of insect morphology. In: Developments in X-Ray Tomography VI Presented at the Developments in X-Ray Tomography VI. International Society for Optics and Photonics. p. 70781U.

Froggatt JMA, Gill BJ. 2016. Bill morphology reflects adaptation to a fibrous diet in the kākāpō (Strigops: Psittaciformes). N Z J Zool 43:138–48.

Frost HM. 1987. Bone “mass” and the “mechanostat”: a proposal. Anat Rec 219:1–9.

Gans C. 1961. The feeding mechanism of snakes and its possible evolution. Integr Comp Biol 1:217–27.

Gans C, de Vree F. 1987. Functional bases of fiber length and angulation in muscle. J Morphol 192:63–85.

Gans C, De Vree F, Carrier DR. 1985. Usage pattern of the complex masticatory muscles in the shingleback lizard, *Trachydosaurus rugosus*: A model for muscle placement. Am J Anat 173:219–40.

Gatesy SM, Bäker M, Hutchinson JR. 2009. Constraint-based exclusion of limb poses for reconstructing theropod dinosaur locomotion. J Vert Paleontol 29:535–44.

Gatesy SM, Middleton KM. 1997. Bipedalism, flight, and the evolution of theropod locomotor diversity. J Vert Paleontol 17:308–29.

Gauthier J, De Queiroz K. 2001. Feathered Dinosaurs, Flying Dinosaurs, Crown Dinosaurs and the Name “Aves.” In: New perspectives on the origin and early evolution of birds: proceedings of the international symposium in honor of John H. Ostrom Peabody Museum of Natural History, Yale University.

Gidmark NJ, Tarrant JC, Brainerd EL. 2014. Convergence in morphology and masticatory function between the pharyngeal jaws of grass carp, *Ctenopharyngodon idella*, and oral jaws of amniote herbivores. J Exp Biol 217:1925–32.

Gignac PM, Erickson GM. 2017. The Biomechanics Behind Extreme Osteophagy in Tyrannosaurus rex. Sci Rep 7:2012.

Gignac PM, Kley NJ, Clarke JA, Colbert MW, Morhardt AC, Cerio D, Cost IN, Cox PG, Daza JD, Early CM, Echols MS, Henkelman RM, Herdina AN, Holliday CM, Li Z, Mahlow K, Merchant S, Müller J, Orsbon CP, Paluh DJ, Thies ML, Tsai HP, Witmer LM. 2016. Diffusible iodine-based contrast-enhanced computed tomography (diceCT): an emerging tool for rapid, high-resolution, 3-D imaging of metazoan soft tissues. J Anat 228:889–909.

Godefroit P, Cau A, Dong-Yu H, Escuillié F, Wenhao W, Dyke G. 2013. A Jurassic avialan dinosaur from China resolves the early phylogenetic history of birds. Nature 498:359–62.

Gray RS. 1977. The Kakapo (*Strigops habroptilus*, Gray, 1847) Its Food, Feeding and Habitat in Fiordland and Maud Island (MSci).

Greaves WS. 1982. A Mechanical Limitation on the Position of the Jaw Muscles of Mammals: The One-Third Rule. J Mammal 63:261–66.

Grigg G, Kirshner D. 2015. Biology and Evolution of Crocodylians Csiro Publishing.

Grosse IR, Dumont ER, Coletta C, Tolleson A. 2007. Techniques for modeling muscle-induced forces in finite element models of skeletal structures. Anat Rec 290:1069–88.

Groth JG, Barrowclough GF. 1999. Basal divergences in birds and the phylogenetic utility of the nuclear RAG-1 gene. Mol Phylogenet Evol 12:115–23.

Gussekloo SWS. 2000. The evolution of the Paleognathous birds: functional morphology and evolutionary patterns.

Gussekloo SWS, Bout RG. 2005. Cranial kinesis in palaeognathous birds. J Exp Biol 208:3409–19.

Gussekloo SWS, Zweers GA. 1999. The Paleognathous Pterygoid-Palatinum complex. A true character? Neth J Zool 49:29–43.

Haas G. 1973. Muscles of the jaws and associated structures in the Rhynchocephalia and Squamata. In: Gans C, Parsons T, editors. Biology of the Reptilia Academic Press. p. 285–490.

Habegger ML, Motta PJ, Huber DR, Deban SM. 2010. Feeding biomechanics in the Great Barracuda during ontogeny. 1–10.

Hackett SJ, Kimball RT, Reddy S, Bowie RCK, Braun EL, Braun MJ, Chojnowski JL, Cox WA, Han K-L, Harshman J, Huddleston CJ, Marks BD, Miglia KJ, Moore WS, Sheldon FH, Steadman DW, Witt CC, Yuri T. 2008. A phylogenomic study of birds reveals their evolutionary history. Science 320:1763–68.

Hart NH, Nimphius S, Rantalainen T, Ireland A, Siafarikas A, Newton RU. 2017. Mechanical basis of bone strength: influence of bone material, bone structure and muscle action. J Musculoskelet Neuronal Interact 17:114–39.

Haut RC, Lancaster RL, DeCamp CE. 1992. Mechanical properties of the canine patellar tendon: Some correlations with age and the content of collagen. J Biomech 25:163–73.

Hedrick BP, Schachner ER, Rivera G, Dodson P, Pierce SE. 2019. The effects of skeletal asymmetry on interpreting biologic variation and taphonomy in the fossil record. Paleobiology 45:154–66.

Herrel A, Aerts P, De Vree F. 2000. Cranial kinesis in geckoes: functional implications. J Exp Biol 203:1415–23.

Herrel A, Aerts P, Fret J, De Vree F. 1999. Morphology of the feeding system in agamid lizards: Ecological correlates. Anat Rec 254:496–507.

Herrel A, Cleuren J, De Vree F. 1996. Kinematics of feeding in the lizard *Agama stellio*. J Exp Biol 199:1727–42.

Herrel A, De Vree F, Delheusy V, Gans C. 1999. Cranial kinesis in gekkonid lizards. J Exp Biol 202 Pt 24:3687–98.

Herrel A, O'Reilly JC. 2006. Ontogenetic Scaling of Bite Force in Lizards and Turtles. Physiol Biochem Zool 79:31–42.

Herrel A, Podos J, Huber SK, Hendry AP. 2005a. Evolution of bite force in Darwin's finches: A key role for head width. J Evol Biol 18:669–75.

Herrel A, Podos J, Huber SK, Hendry AP. 2005b. Bite performance and morphology in a population of Darwin's finches: Implications for the evolution of beak shape. Funct Ecol 19:43–48.

Herrel A, Schaerlaeken V, Meyers JJ, Metzger KA, Ross CF. 2007. The evolution of cranial design and performance in squamates: Consequences of skull-bone reduction on feeding behavior. Integr Comp Biol 47:107–17.

Herrel A, Soons J, Aerts P, Dirckx J, Boone M, Jacobs P, Adriaens D, Podos J. 2010. Adaptation and function of the bills of Darwin's finches: Divergence by feeding type and sex. Emu 110:39–47.

Herring SW, Ochareon P. 2005. Bone - special problems of the craniofacial region. Orthod Craniofac Res 8:174–82.

Hieronymus TL. 2006. Quantitative microanatomy of jaw muscle attachment in extant diapsids. J Morphol 267:954–67.

Hoese WJ, Westneat MW. 1996. Biomechanics of cranial kinesis in birds: Testing linkage models in the white-throated sparrow (*Zonotrichia albicollis*). J Morphol 227:305–20.

Hofer H. 1949. Die Gaumenlucken der Vogel. Acta Zool 30:210–48.

Hofer H. 1950. Zur Morphologie der Kiefermuskulatur der Vögel. Zool Jahrb Abt Anat Ontogenie Tiere 70:427–556.

Holliday CM. 2009. New insights into dinosaur jaw muscle anatomy. Anat Rec 292:1246–65.

Holliday CM, Porter WR, Vliet KA, Witmer LM. 2018. The frontoparietal fossa and dorsotemporal fenestra of archosaurs and their significance for interpretations of vascular and muscular anatomy in dinosaurs. Anat Rec.

Holliday CM, Sellers KC, Davis JL, Middleton KM, Witmer LM. 2014. Modeling Cranial Biomechanics in Archosaurs using 3D computational methods. In: Society of Vertebrate Paleontology p. 149.

Holliday CM, Tsai HP, Skiljan RJ, George ID, Pathan S. 2013. A 3D Interactive Model and Atlas of the Jaw Musculature of *Alligator mississippiensis*. PLoS One 8:e62806.

Holliday CM, Witmer LM. 2007. Archosaur adductor chamber evolution: integration of musculoskeletal and topological criteria in jaw muscle homology. J Morphol 268:457–84.

Holliday CM, Witmer LM. 2008. Cranial kinesis in dinosaurs: intracranial joints, protractor muscles, and their significance for cranial evolution and function in diapsids. J Vert Paleontol 28:1073–88.

Holzman R, Collar DC, Day SW, Bishop KL, Wainwright PC. 2008. Scaling of suction-induced flows in bluegill: morphological and kinematic predictors for the ontogeny of feeding performance. J Exp Biol 211:2658–68.

Homberger DG. 1980. Funktionell-Morpologische Untersuchungen zur Radiation der Ernahrungs-und Trinkmethoden der Papageien. Bonn Zool Monogr 13:1–192.

Homberger DG. 2003. The comparative biomechanics of a prey-predator relationship: The adaptive morphologies of the feeding apparatus of Australian Black-Cockatoos and their foods as a basis for the reconstruction of the evolutionary history of the Psittaciformes. In: Vertebrate Biomechanics and Evolution BIOS Scientific Publishers Ltd. p. 203–28.

Huber DR, Dean MN, Summers AP. 2008. Hard prey, soft jaws and the ontogeny of feeding mechanics in the spotted ratfish *Hydrolagus colliei*. J R Soc Interface 5:941–52.

Hughes S, Wright R, Barry M. 2005. Virtual reconstruction and morphological analysis of the cranium of an ancient Egyptian mummy. Australas Phys Eng Sci Med 28:122–27.

Hull C. 1991. A Comparison of the Morphology of the Feeding Apparatus in the Peregrine Falcon, *Falco-Peregrinus*, and the Brown Falcon, *F-Berigora* (Falconiformes). Aust J Zool 39:67–76.

Hutchinson JR. 2004. Biomechanical modeling and sensitivity analysis of bipedal running ability. II. Extinct taxa. J Morphol 262:441–61.

Huxley TH. 1867. On the classification of birds, and on the taxonomic value of the modification of certain of the cranial bones. P Zool Soc Lond 415–72.

Iordansky NN. 1989. Evolution of Cranial Kinesis in Lower Tetrapods. Neth J Zool 40:32–54.

Iwaniuk AN, Heesy CP, Hall MI, Wylie DRW. 2008. Relative Wulst volume is correlated with orbit orientation and binocular visual field in birds. J Comp Physiol A Neuroethol Sens Neural Behav Physiol 194:267–82.

Jarvis ED, Mirarab S, Aberer AJ, Li B, Houde P, Li C, Ho SYW, Faircloth BC, Nabholz B, Howard JT, Suh A, Weber CC, da Fonseca RR, Li J, Zhang F, Li H, Zhou L, Narula N, Liu L, Ganapathy G, Boussau B, Bayzid MS, Zavidovych V, Subramanian S, Gabaldón T, Capella-Gutiérrez S, Huerta-Cepas J, Rekepalli B, Munch K, Schierup M, Lindow B, Warren WC, Ray D, Green RE, Bruford MW, Zhan X, Dixon A, Li S, Li N, Huang Y, Derryberry EP, Bertelsen MF, Sheldon FH, Brumfield RT, Mello CV, Lovell PV, Wirthlin M, Schneider MPC, Prosdocimi F, Samaniego JA, Vargas Velazquez AM, Alfaro-Núñez A, Campos PF, Petersen B, Sicheritz-Ponten T, Pas A, Bailey T, Scofield P, Bunce M, Lambert DM, Zhou Q, Perelman P, Driskell AC, Shapiro B, Xiong Z, Zeng Y, Liu S, Li Z, Liu B, Wu K, Xiao J, Yinqi X, Zheng Q, Zhang Y, Yang H, Wang J, Smeds L, Rheindt FE, Braun M, Fjeldsa J, Orlando L, Barker FK, Jønsson KA, Johnson W, Koepfli K-P, O'Brien S, Haussler D, Ryder OA, Rahbek C, Willerslev E, Graves GR, Glenn TC, McCormack J, Burt D, Ellegren H, Alström P, Edwards SV, Stamatakis A, Mindell DP, Cracraft J, Braun EL, Warnow T, Jun W, Gilbert MTP, Zhang G. 2014. Whole-genome analyses resolve early branches in the tree of life of modern birds. Science 346:1320–31.

Jetz W, Thomas GH, Joy JB, Hartmann K, Mooers AO, America N. 2012. The global diversity of birds in space and time. Nature 491:444–48.

Ji Q, Ji S 'an. 1996. On the Discovery of the earliest fossil bird in China (*Sinosauropteryx* gen. nov.) and the origin of birds. Chinese Geology 233:30–33.

Jones MEH, Curtis N, Fagan MJ, O'Higgins P, Evans SE. 2011. Hard tissue anatomy of the cranial joints in Sphenodon (Rhynchocephalia): sutures, kinesis, and skull mechanics. Palaeontol Electronica 14:1–56.

Jones MEH, Gröning F, Dutel H, Sharp A, Fagan MJ, Evans SE. 2017. The biomechanical role of the chondrocranium and sutures in a lizard cranium. J R Soc Interface 14:20170637.

Jones MP, Pierce KE, Ward D. 2007. Avian Vision: A Review of Form and Function with Special Consideration to Birds of Prey. Journal of Exotic Pet Medicine 16:69–87.

Kelly DA. 2016. Intromittent Organ Morphology and Biomechanics: Defining the Physical Challenges of Copulation. Integr Comp Biol 56:705–14.

Keyak JH, Fourkas MG, Meagher JM, Skinner HB. 1993. Validation of an automated method of three-dimensional finite element modelling of bone. J Biomed Eng 15:505–9.

Kirchman JJ, Schirtzinger EE, Wright TF. 2012. Phylogenetic relationships of the extinct Carolina Parakeet (*Conuropsis carolinensis*) inferred from DNA sequence data. Auk 129:197–204.

Kirk EJ, Powlesland RG, Cork SC. 1993. Anatomy of the mandibles, tongue and alimentary tract of kakapo, with some comparative information from kea and kaka. Notornis 40:55–63.

Klaus AV, Kulasekera VL, Schawaroch V. 2003. Three-dimensional visualization of insect morphology using confocal laser scanning microscopy. J Microsc 212:107–21.

Kolmann MA, Huber DR. 2009. Scaling of feeding biomechanics in the horn shark *Heterodontus francisci* ontogenetic constraints on durophagy. Zoology 112:351–61.

Korsun PP, Ivanova OV, Afanasiev VL, Kulyk IV. 2016. Distant Jupiter family Comet P/2011 P1 (McNaught). Icarus 266:88–95.

Ksepka DT, Bertelli S, Giannini NP. 2006. The phylogeny of the living and fossil Sphenisciformes (penguins). Cladistics 22:412–41.

Kumar S, Hedges SB. 1998. A molecular timescale for vertebrate evolution. Nature 392:917–20.

Larsson HCE. 2008. Palatal kinesis of *Tyrannosaurus rex*. In: *Tyrannosaurus rex*, the tyrant king Bloomington: University of Indiana Press. p. 245–52.

Lauder GV, Drucker EG, Nauen JC, Wilga CD. 2003. Experimental Hydrodynamics and Evolution: Caudal Fin Locomotion in Fishes. Vertebrate Biomechanics and Evolution 117–35.

Lanfear R, Bromham L. 2011. Estimating phylogenies for species assemblages: a complete phylogeny for the past and present native birds of New Zealand. Mol Phylogenet Evol 61:958–63.

Lautenschlager S. 2015. Estimating cranial musculoskeletal constraints in theropod dinosaurs. R Soc Open Sci 2:150495.

Lautenschlager S, Rayfield EJ, Altangerel P, Zanno LE, Witmer LM. 2012. The endocranial anatomy of therizinosauria and its implications for sensory and cognitive function. PLoS One 7:e52289.

Lautenschlager S, Witmer LM, Altangerel P, Rayfield EJ. 2013. Edentulism, beaks, and biomechanical innovations in the evolution of theropod dinosaurs. Proceedings of the National Academy of Sciences 110:20657–62.

Lee IS, Kim MJ, Yoo DS, Lee YS, Park SS, Bok GD, Han SH, Chung YH, Chang BS, Yi YS, Oh CS, Shin DH. 2007. Three-dimensional reconstruction of medieval child mummy in Yangju, Korea, using multi-detector computed tomography. Ann Anat 189:558–68.

Lee MSY, Bell GL Jr, Caldwell MW. 1999. The origin of snake feeding. Nature 400:655.

Lieberman DE, Polk JD, Demes B. 2004. Predicting Long Bone Loading from Cross-Sectional Geometry. Am J Phys Anthropol 123:156–71.

Livezey BC. 1992. Morphological corollaries and ecological implications of flightlessness in the kakapo (Psittaciformes: *Strigops habroptilus*). J Morphol 213:105–45.

Lockwood CA, Lynch JM, Kimbel WH. 2002. Quantifying temporal bone morphology of great apes and humans: an approach using geometric morphometrics. J Anat 201:447–64.

Lüthy R, Bowie JU, Eisenberg D. 1992. Assessment of protein models with three-dimensional profiles. Nature 356:83–85.

Maddison WP. 1991. Squared-Change Parsimony Reconstructions of Ancestral States for Continuous-Valued Characters on a Phylogenetic Tree. Syst Biol 40:304–14.

Maddison WP, Maddison DR. 2018. Mesquite: A modular system for evolutionary analysis.

Mallison H. 2010. CAD assessment of the posture and range of motion of *Kentrosaurus aethiopicus* Hennig 1915. Swiss J Geosci 103:211–33.

Manafzadeh AR, Padian K. 2018. ROM mapping of ligamentous constraints on avian hip mobility: implications for extinct ornithodirans. Proceedings of the Royal Society B: Biological Sciences 285:1–9.

Martin RB. 2000. Toward a unifying theory of bone remodeling. Bone 26:1–6.

Maynard Smith J, Savage RJG. 1959. The mechanics of mammalian jaws. Sch Sci Rev 40:289–301.

Mayr G. 2010. Parrot interrelationships—morphology and the new molecular phylogenies. Emu - Austral Ornithology 110:348–57.

Mayr G. 2011. Metaves, Mirandornithes, Strisores and other novelties - a critical review of the higher-level phylogeny of neornithine birds: Higher-level phylogeny of birds. J Zoolog Syst Evol Res 49:58–76.

Mayr G, Manegold A, Johansson US. 2003. Monophyletic groups within “higher land birds” - Comparison of morphological and molecular data. J Zoolog Syst Evol Res 41:233–48.

McKibben JS, Harrison GJ. 1987. Clinical Anatomy with emphasis on the Amazon Parrot. In: Harrison GJ, Harrison LR, editors. Clinical Avian Medicine and Surgery p. 31–66.

Meekangvan P, Barhorst AA, Burton TD, Chatterjee S, Schovanec L. 2006. Nonlinear dynamical model and response of avian cranial kinesis. J Theor Biol 240:32–47.

Metzger K. 2002. Cranial Kinesis in Lepidosaurs: Skulls in Motion. In: Aerts P, D’Aout K, Herrel A, Van Damme R, editors. Topics in Functional and Ecological Vertebrate Morphology p. 15–46.

Mezzasalma M, Maio N, Guarino FM. 2014. To move or not to move: Cranial joints in European gekkotans and lacertids, an Osteological and histological perspective. Anat Rec 297:463–72.

Miller RE, Fowler ME. 2014. Fowler’s Zoo and Wild Animal Medicine Elsevier/Saunders.

Mitchell KJ, Llamas B, Soubrier J, Rawlence NJ, Worthy TH, Wood J, Lee MSY, Cooper A. 2014. Ancient DNA reveals elephant birds and kiwi are sister taxa and clarifies ratite bird evolution. Science 344:898–900.

Moazen M, Curtis N, Evans SE, O’Higgins P, Fagan MJ. 2008. Combined finite element and multibody dynamics analysis of biting in a *Uromastyx hardwickii* lizard skull. J Anat 213:499–508.

Moazen M, Curtis N, O’Higgins P, Evans SE, Fagan MJ. 2009. Biomechanical assessment of evolutionary changes in the lepidosaurian skull. Proc Natl Acad Sci USA 106:8273–77.

Moazen M, Curtis N, O’Higgins P, Jones MEH, Evans SE, Fagan MJ. 2009. Assessment of the role of sutures in a lizard skull: a computer modelling study. Proceedings of the Royal Society B: Biological Sciences 276:39–46.

Molnar RE. 1991. The cranial morphology of *Tyrannosaurus rex*. Palaeontographica Abt A 217:137–76.

Molnar RE. 1998. Mechanical factors in the design of the skull of *Tyrannosaurus rex* (Osborne, 1905). Gaia Ecological Perspectives For Science And Society 15:193–218.

Molnar RE. 2008. Reconstruction of the jaw musculature of *Tyrannosaurus rex*. In: Larson PL, Carpenter K, editors. *Tyrannosaurus rex*, the tyrant king Bloomington: Indiana University Press. p. 254–81.

Monteiro LR, Cavalcanti MJ, Sommer HJS 3rd. 1997. Comparative ontogenetic shape changes in the skull of Caiman species (Crocodylia, Alligatoridae). J Morphol 231:53–62.

Montuelle SJ, Williams SH. 2015. In Vivo Measurement of Mesokinesis in *Gekko gecko*: The Role of Cranial Kinesis during Gape Display, Feeding and Biting. PLoS One 10:e0134710.

Muyshondt PGG, Claes R, Aerts P, Dirckx JJJ. 2017. Sound attenuation in the ear of domestic chickens (*Gallus gallus domesticus*) as a result of beak opening. R Soc open sci 4:171286.

Navalón G, Bright JA, Marugán-Lobón J, Rayfield EJ. 2018. The evolutionary relationship between beak shape, mechanical advantage, and feeding ecology in modern birds. Evolution evo.13655.

Norton JJ. 1966. Ternary diagrams of the quartz-feldspar content of pegmatites in Colorado US Government Printing Office.

Nuijens FW, Hoek AC, Bout RG. 2000. The Role of the Postorbital Ligament in the Zebra Finch (*Taeniopygia guttata*). Neth J Zool 50:75–88.

Nuijens FW, Snelderwaard PC, Bout RG. 1997. An electromyographic technique for small animals. J Neurosci Methods 76:71–73.

O'Brien HD, Lynch LM, Vliet KA, Brueggen J, Erickson GM, Gignac PM. 2019. Crocodylian Head Width Allometry and Phylogenetic Prediction of Body Size in Extinct Crocodyliforms. Integr Org Biol 1.

Olsen AM, Camp AL, Brainerd EL. 2017. The opercular mouth-opening mechanism of largemouth bass functions as a 3D four-bar linkage with three degrees of freedom. J Exp Biol 220:4612–23.

Osborn HF. 1912. Crania of *Tyrannosaurus* and *Allosaurus*. Memoirs of the American Museum of Natural History 1:1–32.

Ostrom JH. 1976. On a new specimen of the lower Cretaceous theropod dinosaur *Deinonychus antirrhopus*. Breviora 439:1–21.

Othmer D, Tobias P. 1942. Liquid-Liquid Extraction Data - The Line Correlation. Ind Eng Chem 34:693–96.

Padian K, Chiappe LM. 1998. The origin of birds and their flight. Sci Am 278:38–47.

Pagel M. 1999. The maximum likelihood approach to reconstructing ancestral character states of discrete characters on phylogenies. Syst Biol.

Parker WK. 1866. VIII. On the structure and development of the skull in the ostrich tribe. Phil Trans R Soc Lon 156:113–83.

Parkes KC, Clark GA. 1966. An additional character linking ratites and tinamous, and an interpretation of their monophyly. Condor 68:459–71.

Paton TA, Baker AJ, Groth JG, Barrowclough GF. 2003. RAG-1 sequences resolve phylogenetic relationships within Charadriiform birds. Mol Phylogenet Evol 29:268–78.

Paton TA, Baker AJ. 2006. Sequences from 14 mitochondrial genes provide a well-supported phylogeny of the Charadriiform birds congruent with the nuclear RAG-1 tree. Mol Phylogenet Evol 39:657–67.

Pennycuick CJ. 1967. The strength of the pigeon’s wing bones in relation to their function. J Exp Biol 46:219–33.

Pennycuick CJ. 1968. Power Requirements for Horizontal Flight in the Pigeon Columba Livia. J Exp Biol 49:527–55.

Perry JMG, Prufrock KA. 2018. Muscle Functional Morphology in Paleobiology: The Past, Present, and Future of “Paleomyology.” Anat Rec 301:538–55.

Peters KJ, Kleindorfer S. 2015. Divergent foraging behavior in a hybrid zone: Darwin’s tree finches (*Camarhynchus* spp.) on Floreana Island. Curr Zool 61:181–90.

Pfaller JB, Gignac PM, Erickson GM. 2011. Ontogenetic changes in jaw-muscle architecture facilitate durophagy in the turtle *Sternotherus minor*. J Exp Biol 214:1655–67.

Piras P, Buscalioni AD, Teresi L, Raia P, Sansalone G, Kotsakis T, Cubo J. 2014. Morphological integration and functional modularity in the crocodilian skull. Integr Zool 9:498–516.

Pizo MA, Simáo I, Galetti M. 1995. Diet and flock size of sympatric parrots in the Atlantic forest of Brazil. Ornitol Neotrop 6:87–95.

Pol D, Rauhut OWM, Lecuona A, Leardi JM, Xu X, Clark JM. 2013. A new fossil from the Jurassic of Patagonia reveals the early basicranial evolution and the origins of Crocodyliformes. Biol Rev Camb Philos Soc 88:862–72.

Porro LB, Holliday CM, Anapol F, Ontiveros LC, Ontiveros LT, Ross CF. 2011. Free body analysis, beam mechanics, and finite element modeling of the mandible of *Alligator mississippiensis*. J Morphol 272:910–37.

Preusker F, Scholten F, -D. Matz K, Roatsch T, Willner K, Hviid SF, Knollenberg J, Jorda L, Gutiérrez PJ, Kührt E, Mottola S, A'Hearn MF, Thomas N, Sierks H, Barbieri C, Lamy P, Rodrigo R, Koschny D, Rickman H, Keller HU, Agarwal J, Barucci MA, -L. Bertaux J, Bertini I, Cremonese G, Da Deppo V, Davidsson B, Debei S, De Cecco M, Fornasier S, Fulle M, Groussin O, Güttler C, -H. Ip W, Kramm JR, Küppers M, Lara LM, Lazzarin M, Lopez Moreno JJ, Marzari F, Michalik H, Naletto G, Oklay N, Tubiana C, -B. Vincent J. 2015. Shape model, reference system definition, and cartographic mapping standards for comet 67P/Churyumov-Gerasimenko – Stereo-photogrammetric analysis of Rosetta/OSIRIS image data. Astron Astrophys Suppl Ser 583:A33.

Prum RO. 2002. Why Ornithologists Should Care About The Theropod Origin of Birds. Auk 119:1–17.

Prum RO, Berv JS, Dornburg A, Field DJ, Townsend JP, Lemmon EM, Lemmon AR. 2015. A comprehensive phylogeny of birds (Aves) using targeted next-generation DNA sequencing. Nature 526:569–73.

Ragusa-Netto J. 2004. Flowers, fruits, and the abundance of the yellow-chevroned parakeet (*Brotogeris chiriri*) at a gallery forest in the South Pantanal (Brazil). Braz J Biol 64:867–77.

Rayfield EJ. 2004. Cranial mechanics and feeding in *Tyrannosaurus rex*. Proceedings of the Royal Society B: Biological Sciences 271:1451–59.

Rayfield EJ. 2005. Using finite-element analysis to investigate suture morphology: A case study using large carnivorous dinosaurs. Anat Rec A Discov Mol Cell Evol Biol 283A:349–65.

Rayfield EJ. 2007. Finite Element Analysis and Understanding the Biomechanics and Evolution of Living and Fossil Organisms. Annu Rev Earth Planet Sci.

Rayfield EJ. 2011. Strain in the ostrich mandible during simulated pecking and validation of specimen-specific finite element models. J Anat 218:47–58.

Reed DA, Porro LB, Iriarte-Diaz J, Lemberg JB, Holliday CM, Anapol F, Ross CF. 2011. The impact of bone and suture material properties on mandibular function in *Alligator mississippiensis*: testing theoretical phenotypes with finite element analysis. J Anat 218:59–74.

Reilly GC, Currey JD. 1999. The development of microcracking and failure in bone depends on the loading mode to which it is adapted. J Exp Biol 202:543–52.

Richardson KC, Wooller RD. 1990. Adaptations of the Alimentary Tracts of Some Australian Lorikeets to a Diet of Pollen and Nectar. Aust J Zool 38:581–86.

Richmond BG, Wright BW, Grosse IR, Dechow PC, Ross CF, Spencer MA, Strait DS. 2005. Finite element analysis in functional morphology. Anat Rec A Discov Mol Cell Evol Biol 283A:259–74.

Rieppel OC. 1978. The phylogeny of cranial kinesis in lower vertebrates, with special reference to the Lacertilia. N Jb Geol Palaont Abh 156:353–70.

Rieppel OC. 1984. The structure of the skull and jaw adductor musculature in the Gekkota, with comments on the phylogenetic relationships of the Xantusiidae (Reptilia: Lacertilia). Zool J Linn Soc 82:291–318.

Ross CF, Iriarte-Diaz J. 2014. What does feeding system morphology tell us about feeding? Evol Anthropol 23:105–20.

Rubin CT, Bain SD, McLeod KJ. 1992. Suppression of the osteogenic response in the aging skeleton. Calcif Tissue Int 50:306–13.

Ruff CB. 2000. Body size, body shape, and long bone strength in modern humans. J Hum Evol 38:269–90.

Sacks RD, Roy RR. 1982. Architecture of the hind limb muscles of cats: Functional significance. J Morphol 173:185–95.

Santana SE, Dumont ER, Davis JL. 2010. Mechanics of bite force production and its relationship to diet in bats. Funct Ecol 24:776–84.

Schachner ER, Hutchinson JR, Farmer C. 2013. Pulmonary anatomy in the Nile crocodile and the evolution of unidirectional airflow in Archosauria. PeerJ 1:e60.

Schneider CA, Rasband WS, Eliceiri KW. 2012. NIH Image to ImageJ: 25 years of image analysis. Nat Methods 9:671–75.

Schweizer M, Güntert M, Seehausen O, Leuenberger C, Hertwig ST. 2014. Parallel adaptations to nectarivory in parrots, key innovations and the diversification of the Loriinae. Ecol Evol 4:2867–83.

Schwenk K. 2000. An introduction to tetrapod feeding. In: Feeding: Form, Function and Evolution in Tetrapod Vertebrates. p. 21–61.

Selker F, Carter DR. 1989. Scaling of long bone fracture strength with animal mass. J Biomech 22:1175–83.

Sellers KC, Middleton KM, Davis JL, Holliday CM. 2017. Ontogeny of bite force in a validated biomechanical model of the American alligator. J Exp Biol 220:2036–46.

Sheldon FH, Whittingham LA, Winkler DW. 1999. A comparison of cytochrome b and DNA hybridization data bearing on the phylogeny of swallows (Aves: Hirundinidae). Mol Phylogenet Evol 11:320–31.

Sibley CG, Ahlquist JE. 1990. Phylogeny and Classification of Birds: A Study in Molecular Evolution Yale University Press.

Sibley CG, Monroe BL. 1990. Distribution and Taxonomy of Birds of the World Yale University Press.

Simonetta AM. 1960. On the Mechanical Implications of the Avian Skull and Their Bearing on the Evolution and Classification of Birds. Review Literature And Arts Of The Americas 35:206–20.

Sinclair AG, Alexander RM. 1987. Estimates of forces exerted by the jaw muscles of some reptiles. J Zool 213:107–15.

Siqueira PR, Vasconcelos MF, Gonçalves RMM. 2015. Assessment of stomach contents of some Amazonian birds. Ornitol Neotrop 26:79–88.

Smith KK, Hylander WL. 1985. Strain gauge measurement of mesokinetic movement in the lizard *Varanus exanthematicus*. J Exp Biol 114:53–70.

Snively E, Cotton JR, Ridgely R, Witmer LM. 2013. Multibody dynamics model of head and neck function in *Allosaurus* (Dinosauria, Theropoda). Palaeontol Electronica 16:1–29.

Snively E, Fahlke JM, Welsh RC. 2015. Bone-breaking bite force of *Basilosaurus isis* (Mammalia, Cetacea) from the late Eocene of Egypt estimated by finite element analysis. PLoS One 10:e0118380.

Snively E, Henderson DM, Phillips DS. 2006. Fused and vaulted nasals of tyrannosaurid dinosaurs: Implications for cranial strength and feeding mechanics. Acta Palaeontol Pol 51:435–54.

Snively E, Russell A. 2002. The tyrannosaurid metatarsus: Bone strain and inferred ligament function. Senckenb Lethaea 82:35–42.

Snively E, Russell AP. 2007. Functional morphology of neck musculature in the Tyrannosauridae (Dinosauria, Theropoda) as determined via a hierarchical inferential approach. Zool J Linn Soc 151:759–808.

Snively E, Russell AP, Powell GL, Theodor JM, Ryan MJ. 2014. The role of the neck in the feeding behaviour of the Tyrannosauridae: Inference based on kinematics and muscle function of extant avians. J Zool 292:290–303.

Soons J, Herrel A, Genbrugge A, Aerts P, Podos J, Adriaens D, de Witte Y, Jacobs P, Dirckx J. 2010. Mechanical stress, fracture risk and beak evolution in Darwin's ground finches (*Geospiza*). Philos Trans R Soc Lond B Biol Sci 365:1093–98.

Stephenson RS, Atkinson A, Kottas P, Perde F, Jafarzadeh F, Bateman M, Iaizzo PA, Zhao J, Zhang H, Anderson RH, Jarvis JC, Dobrzynski H. 2017. High resolution 3-Dimensional imaging of the human cardiac conduction system from microanatomy to mathematical modeling. Sci Rep 7:7188.

Strait DS, Wang Q, Dechow PC, Ross CF, Richmond BG, Spencer MA, Patel BA. 2005. Modeling elastic properties in finite-element analysis: How much precision is needed to produce an accurate model? Anat Rec A Discov Mol Cell Evol Biol 283A:275–87.

Suh A, Paus M, Kiefmann M, Churakov G, Franke FA, Brosius J, Kriegs JO, Schmitz J. 2011. Mesozoic retroposons reveal parrots as the closest living relatives of passerine birds. Nat Commun 2:443.

Sustaita D. 2008. Musculoskeletal underpinnings to differences in killing behavior between North American accipiters (Falconiformes: Accipitridae) and falcons (Falconidae). J Morphol 269:283–301.

Sustaita D, Hertel F. 2010. In vivo bite and grip forces, morphology and prey-killing behavior of North American accipiters (Accipitridae) and falcons (Falconidae). J Exp Biol 213:2617–28.

Throckmorton GYS. 1976. Oral food processing in two herbivorous lizards, *Iguana iguana* (Iguanidae) and *Uromastix aegyptius* (Agarnidae). J Morphol.

Toft CA, Wright TF. 2015. Parrots of the Wild: A Natural History of the World's Most Captivating Birds Oakland: Univ of California Press.

Tokita M. 2003. The skull development of parrots with special reference to the emergence of a morphologically unique cranio-facial hinge. Zoolog Sci 20:749–58.

Tokita M. 2004. Morphogenesis of parrot jaw muscles: understanding the development of an evolutionary novelty. J Morphol 259:69–81.

Tokita M, Kiyoshi T, Armstrong KN. 2007. Evolution of craniofacial novelty in parrots through developmental modularity and heterochrony. Evol Dev 9:590–601.

Tsai HP, Holliday CM. 2015. Articular soft tissue anatomy of the archosaur hip joint: Structural homology and functional implications. J Morphol 276:601–30.

Tseng ZJ, Binder WJ. 2010. Mandibular biomechanics of *Crocuta crocuta*, *Canis lupus*, and the late Miocene *Dinocrocuta gigantea* (Carnivora, Mammalia). Zool J Linn Soc 158:683–96.

Turner AH, Nesbitt SJ. 2013. Body size evolution during the Triassic archosauriform radiation. Geological Society, London, Special Publications 379:573–97.

van der Meij MAA. 2004. A tough nut to crack: Adaptations to seed cracking in finches. Universiteit Leiden 330:149.

van der Meij MAA, Bout RG. 2006. Seed husking time and maximal bite force in finches. J Exp Biol 209:3329–35.

van der Meij MAA, Bout RG. 2008. The relationship between shape of the skull and bite force in finches. J Exp Biol 211:1668–80.

Van Eijden TMGJ. 2000. Biomechanics of the mandible. Crit Rev Oral Biol Med 11:123–36.

Vanden Berge, Zweers. 1993. Myologia. In: Baumel JJ, King AS, Breazile JE, Evans HE, Vanden Berge JC, editors. Nomina Anatomica Avium II Cambridge: Nuttal Ornithol. Club. Publ. p. 189–250.

Versluys J. 1910. Streptostylie bei Dinosaurien, nebst Bemerkungen über die Verwandschaft der Vogel und Dinosaurier. Zoologisches Jarhbuch 30:75–260.

Verwaijen D, Van Damme R, Herrel A. 2002. Relationships between head size, bite force, prey handling efficiency and diet in two sympatric lacertid lizards. Funct Ecol 16:842–50.

Vincent SE, Moon BR, Herrel A, Kley NJ. 2007. Are ontogenetic shifts in diet linked to shifts in feeding mechanics? Scaling of the feeding apparatus in the banded watersnake Nerodia fasciata. J Exp Biol 210:2057–69.

Vinyard CJ, Wall CE, Williams SH, Hylander WL. 2008. Patterns of variation across primates in jaw-muscle electromyography during mastication. Integr Comp Biol 48:294–311.

Wang Q, Wood SA, Grosse IR, Ross CF, Zapata U, Byron CD, Wright BW, Strait DS. 2012. The Role of the Sutures in Biomechanical Dynamic Simulation of a Macaque Cranial Finite Element Model: Implications for the Evolution of Craniofacial Form. Anat Rec 295:278–88.

Wickham H. 2016. Ggplot2: Elegant Graphics for Data Analysis.

Witmer LM, Rose KD. 1991. Biomechanics of the jaw apparatus of the gigantic Eocene bird Diatryma: Implications for diet and mode of life. Paleobiology 17:95–120.

Witmer LM, Sampson SD, Solounias N. 1999. The proboscis of tapirs (Mammalia: Perissodactyla): A case study in novel narial anatomy. J Zool 249:249–67.

Wroe S, McHenry C, Thomason J. 2005. Bite club: comparative bite force in big biting mammals and the prediction of predatory behaviour in fossil taxa. Proceedings of the Royal Society B: Biological Sciences 272:619–25.

Xu X, Wang X-L, You H-L. 2000. A primitive ornithopod from the early Cretaceous Yixian formation of Liaoning. Vertebrata palasiatica.

Yamada H. 1970. Strength of biological materials Williams & Wilkins.

Yanega GM, Rubega MA. 2004. Hummingbird jaw bends to aid insect capture. Nature 428:615.

Zemla A. 2003. LGA: A method for finding 3D similarities in protein structures. Nucleic Acids Res 31:3370–74.

Zhou Z, Zhang F. 2002. Largest bird from the Early Cretaceous and its implications for the earliest avian ecological diversification. Naturwissenschaften 89:34–38.

Zusi RL. 1967. The Role of the Depressor Mandibulae Muscle in Kinesis of the Avian Skull. Proceedings of the United States National Museum 123:1–28.

Zusi RL. 1984. A functional and evolutionary analysis of rhynchokinesis in birds. Smithson Contrib Zool 1–40.

Zusi RL. 1987. A Feeding Adaption of the Jaw Articulation In New World Jays Corvidae. Auk 104:665–80.

Zusi RL. 1993. Patterns of diversity in the avian skull. In: Hanken J, Hall BK, editors. The Skull, Volume 2: Patterns of Structural and Systematic Diversity University of Chicago Press. p. 391–429.

VITA

I grew up with a limestone driveway and one of my earliest memories was finding small marine fossils there. I announced that I wanted to be a paleontologist in elementary school and I have had a strong interest in fossils ever since. Despite originally earning a B. A. in Asian History at Bridgewater State University and an M. Ed. in special education at Lesley University, I never stopped wanting to work with animals, fossil or living. This is what drove me to go back to school and to follow my original dream. I worked to describe a plesiosaur fossil to earn an M. S. in Biology at Fort Hays State University and I discovered a love of birds and photography. My passion for birds and photography complements my academic interests in fossils and anatomy. I have combined all of these topics as a Ph. D. student in Integrative Anatomy in the Veterinary Pathobiology program at the University of Missouri to better understand and describe the functional morphology of birds, dinosaurs, and other reptiles. My work ultimately leads to a better understanding of the history of feeding biomechanics in all animals. I am more passionate about discovering the evolutionary history of reptile feeding than when I initially arrived here, and I know that as I continue my research that enthusiasm and passion will only continue to grow. Additionally, my work and responsibilities at the University of Missouri have also helped me to improve my skillsets as an anatomist, educator, mentor, and coordinator of outreach events. These skills will enable me to educate future scientists, doctors and nurses, and the public as well.